National Library of Canada
Acquisitions and Bibliographic Services Branch
395 Wellington Street
Ottawa, Ontario
K1A 0N4

Bibliothèque nationale du Canada
Direction des acquisitions et des services bibliographiques
395, rue Wellington
Ottawa (Ontario)
K1A 0N4

Your file Votre référence

Our file Notre référence

NOTICE

The quality of this microform is heavily dependent upon the quality of the original thesis submitted for microfilming. Every effort has been made to ensure the highest quality of reproduction possible.

If pages are missing, contact the university which granted the degree.

Some pages may have indistinct print especially if the original pages were typed with a poor typewriter ribbon or if the university sent us an inferior photocopy.

AVIS

La qualité de cette microforme dépend grandement de la qualité de la thèse soumise au microfilmage. Nous avons tout fait pour assurer une qualité supérieure de reproduction.

S'il manque des pages, veuillez communiquer avec l'université qui a conféré le grade.

La qualité d'impression de certaines pages peut laisser à désirer, surtout si les pages originales ont été dactylographiées à l'aide d'un ruban usé ou si l'université nous a fait parvenir une photocopie de qualité inférieure.

Canada

Quantum Corrections to the Conductivity in Disordered Conductors

by

Abdelhadi Sahnoune
Department of Physics, McGill University
Montréal, Québec

October 1992

A Thesis submitted to the
Faculty of Graduate Studies and Research
in partial fulfillment of the requirements for the degree of
Doctor of Philosophy

ISBN 0-315-87676-X

Canada

Abstract

Quantum corrections to the conductivity have been studied at low temperatures down to 0.15K and fields up to 8.8T in two different disordered systems, namely amorphous Ca-Al alloys doped with Ag and Au and icosahedral Al-Cu-Fe alloys. In the former the influence of spin-orbit scattering on the enhanced electron-electron contribution to the resistivity has been, for the first time, clearly displayed. As the spin-orbit scattering rate increases, this contribution decreases rapidly to finally vanish at extremely high spin-orbit scattering rates. Furthermore the analysis shows that the current weak localization theory gives an accurate description of the experiments irrespective of the level of spin-orbit scattering.

In icosahedral Al-Cu-Fe alloys, detailed study of the low temperature resistivity shows that the magnetoresistance and the temperature dependence of the resistivity data are consistent with the predictions of quantum corrections to the conductivity theories. The success of these theories in this alloy system is attributed to intense electron scattering due to disorder. The spin-orbit scattering and the electron wave-function dephasing rates are extracted from fitting the magnetoresistance. The dephasing rate is found to vary as AT^p with $p \sim 1.5$; a characteristic of electron-electron scattering in the strong disorder limit. An antilocalization effect has also been directly observed in the temperature dependence of the resistivity in one of the samples.

Résumé

Les corrections quantiques à la conductivité on été étudiées à basses températures jusqu'à 0.15K et dans un champ magnétique atteignant 8.8T, dans deux systèmes désordonnés differents, en l'occurence les alliages amorphes de Ca-Al dopés avec Ag et Au et les alliages icosaédriques d'Al-Cu-Fe. Dans le premier, l'influence de la diffusion spin-orbite sur la contribution de l'interaction renforcée des électrons à la resistivité a été, pour la première fois, clairement démontrée. Quand le taux de diffusion spin-orbite augmente celle-ci diminue rapidement pour finalement disparaitre à très forte diffusion spin-orbite. D'autre part, l'analyse a demontré que la théorie actuelle de la localisation faible donne une description précise des données expérimentales indépendemment du niveau de la diffusion spin-orbite.

Dans les alliages icosaédriques d'Al-Cu-Fe, l'étude détaillée de la résistivité à basse température montre que les données de la magnétoresistance et de la dépendence en température de la résistivité sont en accord avec les prédictions des théories des corrections quantiques à la conductivité. Le succés de ces théories est attribué à la diffusion intense des électrons dûe au désordre. Les taux de diffusion spin-orbite et du déphasage de la fonction d'onde de l'électron ont été tirés du lissage de la magnétorésistance. Le taux de déphasage varie selon AT^p avec $p \sim 1.5$; caractéristique de la diffusion électron-électron dans les systèmes fortement désordonnés. L'effet de l'antilocalisation sur la dépendence en température de la résistivité a été directement observé dans l'un des échantillons.

Acknowledgments

First and foremost, I wish to thank Prof. John O. Ström-Olsen, my research supervisor, for all his support and continuous encouragement throughout my graduate work at McGill. Thanks are also due to Prof. Zaven Altounian for numerous enlightening discussions at various stages of this project.

My sincere thanks go to Dr. Reinhart Richter and Prof. David V. Baxter who first initiated me to the experimental techniques used in this work. I am also grateful to them for the very useful discussions we had on quantum corrections to the conductivity phenomena and for writing most of the fitting routines I used in the analysis of the data presented in this thesis.

Many people have contributed in one way or another to this thesis. I would like to express my thanks in particular to Dr. Henry E. Fischer for his help during dilution refrigerator experiments, Dr. Alicja Zaluska for the outstanding TEM and SEM work she performed on my quasicrystalline samples, Frank Van Gils for his technical assistance, Betty Pedersen, Diane Koziol and Paula Domingues for their help in the administrative paper work.

I would also like to thank my fellow graduate students. During my stay at McGill I enjoyed the friendship and discussions with Noureddine Mebarki, Ahmed Houari, Mohamed Laradji, Andrew Dawson, Lixiang Liao, Steve Brauer, Karim Aguennaou and many others. I will really miss the entertaining coffee-break discussions about science, politics, and social life with Andrew Dawson.

Special thanks are due to the Ministère de l'Enseignement Supérieur of Algeria, the Graduate Faculty of McGill University, the Natural Sciences and Engineering research Council of Canada, les Fonds pour la Formation des Chercheurs et l'aide à la Recherche du Québec for their financial assistance.

At last but not least, I thank my parents and all members of my family for their moral support throughout the years of my studies. I want them to know that without their help and encouragement my life as a student would have been a very tedious road.

Contents

List of Figures

List of Tables

Chapter 1

Introduction

In 1979 a new field in solid state physics was discovered. It deals with anomalous electron transport properties in disordered conductors. The phenomenon is generally called weak localization and is essentially caused by coherent interference of the conduction electron wavefunctions due to intense elastic scattering by the defects of the system. Theoretically, this phenomenon was first considered by Abrahams, Anderson, Licciardello and Ramakrishnan [1] when, following the ideas of Thouless [2], they developed a scaling theory of electron localization in two dimensional systems. Since then extensive theoretical work as well as experimental investigations have been carried out and it has been shown that weak localization effects occur in one and three dimensional systems as well as in two dimensional systems [3, 4, 5]

Weak localization shows up most dramatically as a change of the electrical resistivity of a disordered conductor, for example an amorphous metal, in the presence of a magnetic field. Since it is possible to measure these changes very accurately, many interesting physical properties have been observed. Moreover, it is well known today that measurement of the weak localization effect provides a very useful tool for determining the characteristic scattering times of the conduction electron system [6, 7]. The reason is that the phenomenon is a quantum interference effect controlled by the different scattering processes such as inelastic, spin-orbit and spin-spin scattering, and the rates can be deduced by a direct comparison of the theory to the experiment.

Almost coincidentally with the theory of weak localization, Altshuler and Aronov pointed out that, in the limit of intense elastic scattering (as in amorphous metals) the interaction between the electrons is affected causing important corrections to the electron density of states [8]. Intense scattering leads to a decrease in the dynamical screening, hence enhancing the electron-electron interaction. As a result significant temperature and magnetic field dependent corrections to the resistivity were also predicted.

Without exception, all theories developed so far to deal with the transport properties of disordered metals are based on the fact that, with disorder the electron motion becomes diffusive in contrast with ordered (i.e. crystalline) conductors where the electron motion is ballistic. In the presence of disorder, a plane-wave description of the conduction electrons breaks down and the Boltzmann approach [9] is no longer applicable for calculating the resistivity. Furthermore, as the amount of disorder is increased quantum mechanical effects dominate the physics. As a consequence, they must be incorporated in the calculations of the electronic transport properties of disordered systems.

It is now well established that weak localization and enhanced electron-electron interactions theories, also known today under the generic term quantum corrections to the conductivity, provide a very good description of the low temperature transport properties of a wide variety of disordered systems of various dimensionalities. Bergmann investigated the magnetoresistance in Mg, Cu, Ag, and Au [7, 10, 11] films and found remarkable agreement between the experiment and the theory for quasi-two dimensional systems. Good agreement has also been reported in very thin wires (quasi-one-dimensional conductors) by Masden and Giordano [12] and Santhanam *et al.* [13]. Three dimensional disordered systems are no exception; although earlier investigations reported some important discrepancies between the theory and experiment at large magnetic fields [14, 15, 16, 17], it has been since shown that quantum corrections to the conductivity theories provide an accurate description of the data

in simple bulk metals, as well.[1] In particular it was found by Sahnoune and Ström-Olsen [18] and Lindqvist *et al.* [19] that the theory quantitatively agrees with the measurements in Ca-Mg-Al amorphous alloys. Moreover it was clearly demonstrated that both weak localization and enhanced electron-electron interactions terms are essential for describing the data.

The success and the current understanding of the quantum corrections to the conductivity theories is so good, that specific and detailed studies can be carried out. Moreover, these theories can now be used as a tool not only to determine the characteristic times of the electron system but also to probe the electronic properties of non conventional metals (such as quasicrystals).

The present work has two main objectives. First, to investigate in a systematic way the influence of spin-orbit scattering on the enhanced electron-electron interactions corrections to the resistivity, the last major problem in quantum corrections to the conductivity theories that remains unanswered. Second, by using quantum corrections to the conductivity theories, to get an insight into the low temperature transport properties of the novel Al-Cu-Fe icosahedral alloys.

Unlike the theory of weak localization for which the role of spin-orbit scattering has been investigated in great detail by both theory [20, 21, 22] and experiment [10, 11, 23, 24], to date the influence of spin-orbit scattering on the electron-electron interaction has received little attention. The only theoretical predictions due to Altshuler *et al.* [25] and Millis and Lee [26], are that the magnetoresistance for example, vanishes in the extremely strong spin-orbit regime. On the experimental side, most studies have concentrated on qualitative comparisons with the theory without any detailed analysis of the results. This was in part due to the relative insensitivity of the electron-electron interaction to low magnetic fields. However, the studies were made even more difficult as most of the systems selected where made of heavy elements (with strong

[1] Weak localization and enhanced electron-electron interaction effects in bulk conductors are less pronounced than those observed in one- and two-dimensional systems where the restricted geometry of the conductor imposes more constraints on the interfering electrons.

spin-orbit scattering which is predicted to suppress the electron-electron interaction contribution) [14, 27] or contained transition metal elements [15, 28, 29] which make the analysis ambiguous and the results less conclusive.

To achieve the first goal it is therefore imperative to select a simple system where the electron-electron interaction contribution to the resistivity is relatively large and can be identified unambiguously. Such a system is amorphous Ca-Al alloys. Apart from being well characterized [30, 31, 32, 33], this system has a very low level of spin-orbit scattering when compared to other amorphous systems. Hence the spin-orbit interaction effect on electron-electron interaction is at its minimum. In fact this feature makes amorphous Ca-Al alloy system very attractive if not unique for a quantitative study of spin-orbit scattering effect on the correction to the resistivity originating from electron-electron interaction in bulk disordered conductors. The spin-orbit scattering will be systematically varied from very weak to very strong by progressively replacing Al with heavy elements (Ag and Au) which have high spin-orbit coupling. The level of the dopant is kept low so that other electronic properties of the alloy are not appreciably affected. By this means, in an otherwise constant system, the effect of spin-orbit interaction on electron-electron interactions can be directly examined. Moreover, at the same time the study will also provide a test of the accuracy of the quantum corrections to the conductivity theories over a wide range of spin-orbit scattering.

Since the discovery by Shechtman and coworkers of the first quasicrystalline metal alloy about eight years ago [34], quasicrystals have been under intensive investigation in order to understand their basic structural and physical properties. Although their structure is incompatible with conventional crystallography, these materials are not structurally disordered either. They belong to a new class of an ordered structure with a five-fold symmetry (not allowed in the Bravais lattice classification scheme) and in which the translational order is preserved only in a quasiperiodic way while maintaining the long-range orientational order [35]. Yet, these systems give very sharp peaks (very often narrower than the instruments resolution) in x-ray and electron-

diffraction experiments, reminiscent only of single crystals. Most of the quasicrystals known today have been prepared by rapid quenching from the melt as metastable phases but some do exist as thermodynamically stable phases over a wide temperature range, from room temperature to several hundred degrees just below the melting temperature. Among them are Al-Cu-Ru [36] and Al-Cu-Fe [37, 38] icosahedral alloys.

Regarding the electron transport properties, they were also immediately investigated. But in several cases, this was hindered by the presence of impurity crystalline and/or amorphous phases along the quasicrystalline phase, as they also participate in the transport. Furthermore a number of them, like AlMn and U-Pd-Si alloys, exhibit magnetic behavior which complicates the analysis [39, 40]. It is only with the preparation of single-phased and non-magnetic quasicrystals that comprehensive studies became possible. Based on the x-ray and electron diffraction patterns which indicate a very well ordered structure, it was intuitively expected that the physical properties of quasicrystals will be similar to those of crystalline metals. But this turned out to be totally wrong. In fact it was found that the transport properties of these materials resemble in many aspects those of highly disordered metals. For instance, early measurements of the resistivity in several quasicrystalline alloys reported values varying from $\sim$ 50 to 400 $\mu\Omega$.cm, typical of amorphous conductors. Furthermore and to the surprise of the workers in the field, a newly discovered class of stable quasicrystals, which includes Al-Cu-Fe, Al-Cu-Ru and Al-Mn-Pd alloys, present very high resistivities ($\sim 4000 - 30000\mu\Omega$.cm), one to two orders of magnitude larger than that of the most resistive amorphous metals. Another unexpected property of quasicrystals is that their already high resistivity tends to increase with increasing quasicrystallinity, i.e. with increasing atomic order, in contrast to conventional metals where removing defects always lowers the resistivity. It has been suggested that this results from low carrier density at the Fermi level due to the presence of a pseudogap in the density of states. The existence of the pseudogap is believed to arise from a strong interaction of the Fermi surface with the Brillouin zone boundaries [41, 42]. Moreover according to many authors, this pseudogap plays a key role in the stability of the quasicrystalline

phase, in the same way as the Hume-Rothery type metals. In fact, Poon [41] argues that the positioning of the Fermi level near the minimum of the pseudogap would tend to lower the electronic energy making the formation of a quasicrystalline phase competitive with other structures. This view is supported by both specific heat measurements [43, 44] which report reduced density of states at the Fermi level, and soft-x-ray emission and photoabsorption spectroscopy experiments [45, 46, 47] which indicate the emergence of a minimum in the density of states in the vicinity of the Fermi level. Numerical calculations of the electron density of states, though limited to small samples due to the complexity of the quasicrystalline structure, are also in support of this scenario [48, 49]. To set against this however are the low temperature resistivity and magnetoresistance studies in several quasicystalline alloys [50, 51, 52, 53] where it is found that both the temperature dependence of the resistivity and the magnetoresistance are well described by quantum corrections to the conductivity theories which, as pointed out above, were derived to describe the anomalous resistivity of disordered conductors. Thus, the second aim of the present work is to make use of our knowledge and understanding of weak localization and enhanced electron-electron theories in a quantitative and complete study of the low temperature resistivity of one of the simplest quasicrystalline alloys, namely icosahderal Al-Cu-Fe alloys. This alloy system is particularly interesting for several reasons. First, samples of high structural quality can be prepared with relative ease [37, 38]. Second, they exhibit very high resistivities, ranging from 4500 to 10000$\mu\Omega$.cm, reminiscent of highly doped semiconductors. Third, magnetic susceptibility measurements [44, 53] have shown that the system is non-magnetic. Hence difficulties, arising from possible superposition of complicated magnetic effects are avoided. Recent work on this system by Biggs and coworkers [43] and Klein *et al.* [44, 52, 53] was mainly limited to measurements of the specific heat, Hall coefficient and temperature dependence of the resistivity. Here, the low temperature resistivity and magnetoresistance are completely analyzed within the framework of weak localization and enhanced electron-electron interaction theories[2].

[2]In references [44, 52, 53] only the temperature dependence of the resistivity was so analyzed.

Furthermore we show that it is of great importance to consider the full fitting to obtain a clear and consistent picture of the dephasing of the electron wavefunction.

The thesis is organized as follows. In the next Chapter, weak localization and enhanced electron-electron interactions phenomena are discussed followed by the analytical expressions of the corrections to the resistivity that will be used for analyzing the experimental data. In Chapter 3, the different experimental techniques used in this work for the sample preparation and the resistance measurements are described. In Chapter 4 we present, discuss and analyze the results of the low temperature resistivity measurements of amorphous Ca-Al-(Ag,Au) and icosahedral Al-Cu-Fe alloys. Chapter 5 contains the summary of the main results obtained in this thesis and suggestions for future work.

Chapter 2

Review of Quantum Corrections to the Conductivity Theories

Over the past few years it has been well established that the transport properties of disordered conductors cannot be understood using models that were derived for ordered systems. This chapter gives a review of the alternative theories that will help the reader in understanding the significance of the results presented in this thesis. Emphasis is placed on the physical origin of the quantum corrections to conductivity and their predictions regarding the magnetic field and temperature dependence of the resistivity. For a detailed derivation of the mathematical expressions the reader is referred to the many excellent reviews on the subject [3, 4, 54].

Prior to presenting these theories it is useful to mention what is predicted by the classical theories. It is well known that, within the free electron model where the elastic scattering time of the electron, τ_e, is a constant, there is no magnetic field dependence of the resistivity- i.e. no magnetoresistance [55]. However in real metals it was observed a long time ago that a magnetoresistance does exist and is proportional to B^2, B being the magnetic field. This magnetoresistance results usually from non-free electron behavior of metals- e.g. non-spherical Fermi surface [56], and can be

expressed as (see Kohler's rule [55]):

$$\frac{\Delta\rho}{\rho} \approx (\omega_c\tau_e)^2 = \frac{1}{(ne\rho)^2}B^2, \tag{2.1}$$

where $\omega_c = \frac{eB}{m}$ is the cyclotron frequency, n the electron density and ρ the resistivity.

In the case of high resistivity samples, such as the ones studied in this thesis, the above equation gives values at least five to six orders of magnitude smaller than what we observe experimentally. Therefore it is clear again that in order to explain our results one cannot resort to classical theories but needs to consider more elaborate theories.

2.1 Weak localization

Based on scaling arguments, Abrahams *et al.* [1] have shown in 1979 that the electrical conductivity in the presence of disorder is no longer given by the Boltzmann theory. Instead, due to coherent backscattering of the electron's wavefunction, they predicted important corrections to the conductivity.

The correction to the Boltzmann conductivity is usually calculated within the Kubo formalism and is obtained by evaluating the so-called fan-diagrams, first considered by Langer and Neal [57]. We do not intend to reproduce the derivation of the various expressions published to date. However we will describe below the physical picture of the phenomenon and then give the relevant analytical results that will be used in the analysis of the experimental data presented in chapter 4.

As mentioned in the previous chapter, when electron scattering is intense as in a disordered conductor, the motion of the electron becomes diffusive rather than ballistic. In most metals when this happens the mean free path, l_e, is of the order of the electron's wavelength λ_F, and the electrons become localized and do not contribute to the conduction. The amount of disorder is generally quantified by the so-called disorder parameter defined as: $(k_F l_e)^{-1}$, where k_F is the Fermi wavevector. Weak and strong disorder correspond to $(k_F l_e)^{-1} \ll 1$ and $(k_F l_e)^{-1} \sim 1$, respectively. To illustrate the localization phenomenon consider an electron that is diffusing through a

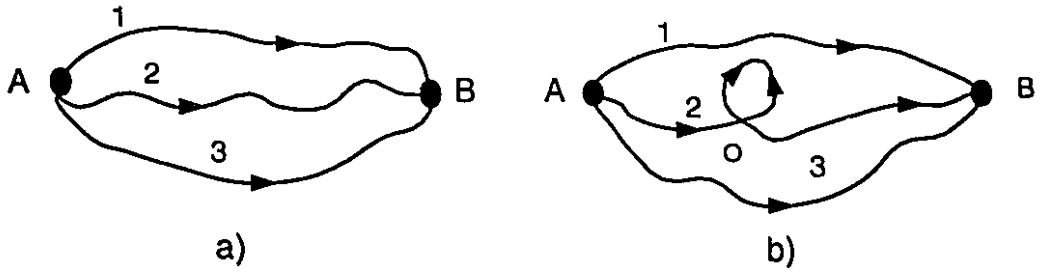

Figure 2.1: Electron diffusion paths, a) Non-intersecting paths, b) Self-intersecting paths (path 2).

disordered conductor as shown in Figure 2.1. To get from point A to point B (Figure 2.1.a), the electron can diffuse along different paths. Then the total probability $P(\mathrm{A},\mathrm{B})$ to diffuse from A to B is given by the square modulus of the sum of all amplitudes A_i of the probability for the particle to follow each path, i.e.

$$P(A,B) = \left|\sum_i A_i\right|^2 = \sum_i \mid A_i \mid^2 + \sum_{i \neq j} A_i A_j^*. \tag{2.2}$$

The first term in Eq. (2.2) represents the sum of probabilities for the particle to diffuse along any possible path and the second term represents the interference of various probability amplitudes. Since the path lengths differ strongly, the phases of the wavefunctions are also substantially different. Therefore, when summing over all possible paths, the mean value of the interference term at point B vanishes due to the oscillatory behavior of the terms contributing to it, and the probability of transfer reduces to $P(A,B) = \sum_i \mid A_i \mid^2$.

However, this is no longer true when one looks at paths similar to the one labeled 2 in Figure 2.1.b. Along this class of paths, called self-intersecting paths, the interference term is essential and cannot be neglected. For instance consider point O on path 2. Due to the wave-like character of the electron, there are two different

ways in which the electron can propagate around the loop with equal probability; clockwise and counterclockwise. In the presence of elastic scattering only, the two partial wavefunctions will have at point O the same phase and hence will interfere constructively. This coherent superposition of the wavefunctions therefore results in an enhanced probability to find the electron at point O. To emphasize this further we can let B tend to A. Each loop then can be traversed in both directions with equal probability and the total probability of return of the electron to its initial position is now given by:

$$P(O,O) = 2\sum_i \mid A_i \mid^2; \tag{2.3}$$

i.e. twice as large as when the interference term is neglected. Under these circumstances, the electron is said to be *weakly localized*. The enhanced probability of return implies that there is a reduced probability to find the electron elsewhere and hence leads to an increase in the resistivity. However it is important to note that the constructive interference just described occurs provided the diffusing electrons retain phase coherence along the self-intersecting paths. In fact, phase coherence can be lost in several ways; by inelastic electron-phonon, electron-electron, spin-spin and spin-orbit scattering processes (which will be discussed later on in see subsections 2.1.2-4). This leads to the definition of a characteristic length scale, L_ϕ, called phase coherence length (or equivalently to the definition of τ_ϕ, the phase coherence time). This length scale, given by $L_\phi = \sqrt{D\tau_\phi}$, where D is the electron diffusion constant, is the average distance beyond which phase coherence is lost. Thus loops longer than L_ϕ do not contribute to the constructive interference. At low temperatures, L_ϕ is typically a few tenths of a micron in three dimensional amorphous metals.

In real space the classical diffusion equation in d dimensions yields for the probability density of finding the electron at time t and position $\vec{r}$:

$$p(\mathrm{r},t) = \frac{1}{(4\pi Dt)^{d/2}} e^{-\vec{r}^2/4Dt}. \tag{2.4}$$

Hence the probability to find the electron at the origin is $p(o,t) = \frac{1}{(4\pi Dt)^{d/2}}$. But as explained above, one must consider two partial waves which propagate around

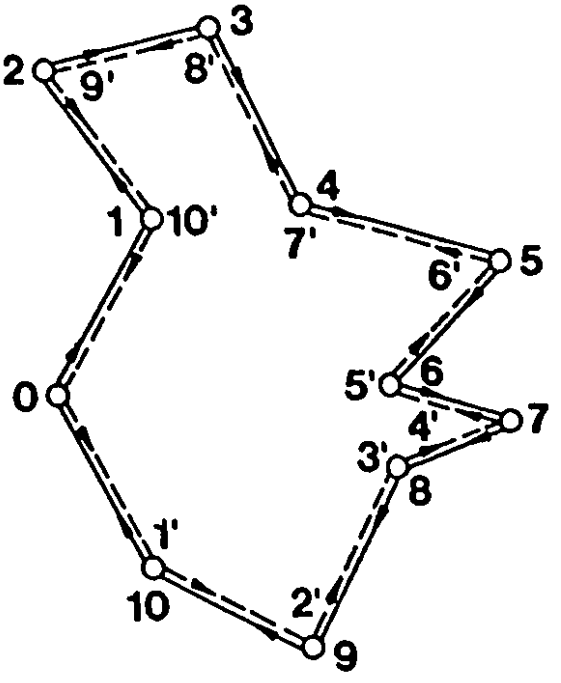

Figure 2.2: An electron diffusing around a closed loop. From reference [6]

a closed path in opposite directions as shown in Figure 2.2. At the origin, their amplitudes add (instead of their intensities) and therefore the probability of return is now doubled, i.e. $2 \times \frac{1}{(4\pi Dt)^{d/2}}$, as shown qualitatively in Figure 2.3.

To estimate the correction to the conductivity arising from the electron localization one needs to consider the probability of an electron ray-tube of cross section λ_F^2 to intersect itself. The magnitude of the correction to the conductivity is then given by [5]:

$$\frac{\Delta\sigma}{\sigma} \sim -\int_{\tau_e}^{\tau_\phi} \frac{\lambda^2 v_F dt}{(Dt)^{d/2}}, \tag{2.5}$$

where v_F is the Fermi velocity, and

$$D = \frac{v_F l_e}{d}.$$

The lower integration limit τ_e (the elastic scattering time) corresponds to the minimum time for a self-intersecting path and the upper limit the phase coherence time

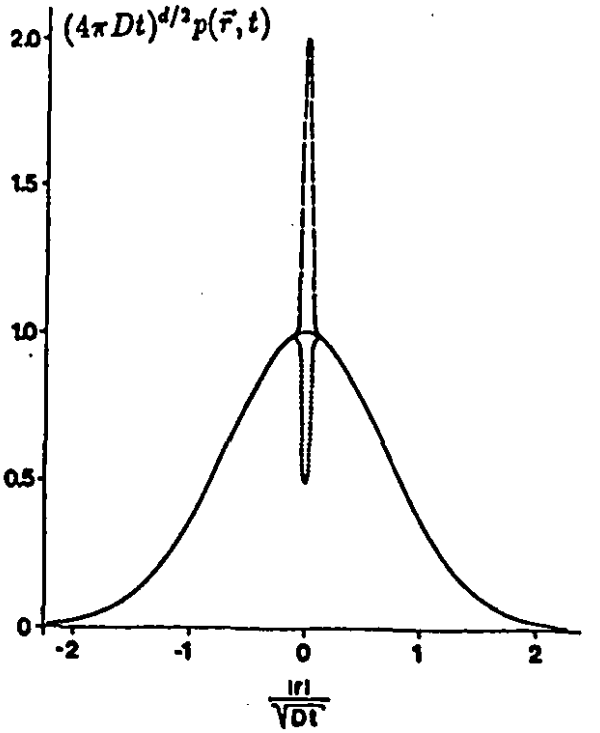

Figure 2.3: The probability distribution of a diffusing electron which starts at $\vec{r} = 0$ at $t = 0$ from Bergmann [6]. The solid line is the classical diffusion probability. Quantum constructive interference enhances the probability of return to the origin by a factor of two (dashed line). Large spin-orbit scattering reduces the probability by a factor of two and leads to weak anti-localization (dotted peak).

of the electron wavefunction, as defined above. Evaluating the above integral gives:

$$\begin{aligned} \Delta\sigma &\sim -\tfrac{e^2}{\hbar} L_\phi & d = 1 \\ \Delta\sigma &\sim -\tfrac{e^2}{\hbar} \ln\left(\tfrac{L_\phi}{l_e}\right) & d = 2 \\ \Delta\sigma &\sim \tfrac{e^2}{\hbar L_\phi} & d = 3 \end{aligned} \tag{2.6}$$

It has to be stressed once again that the above interference is constructive only in the absence of inelastic scattering and spin-spin scattering (the role of spin-orbit scattering will be discussed separately later on). In other words, the time-reversal symmetry must be conserved during the propagation of the electron wavefunction around the loop. The temperature dependence of the correction to the conductivity comes from the temperature dependence of L_ϕ (or $\tau_\phi \propto T^{-p}$). Thus in two dimensions one expects a logarithmic dependence on temperature while in one and three dimensions a power law dependence is predicted. The time τ_ϕ is a fundamental parameter of

weak localization phenomenon and deserves special attention (see subsection 2.1.2).

In the presence of a magnetic field, which also destroys the time-reversal symmetry of the system, the coherent interference is altered. When placed in a magnetic field B, the electron wavefunction propagating around a loop acquires a phase shift $\delta\Phi \propto \int \vec{A}.d\vec{l}$, where $\vec{A}$ is the magnetic vector potential. The sign of the phase shift depends on the direction of propagation with respect to the field. Therefore, the two partial waves going in opposite directions return to the origin with a relative phase shift $\Delta\Phi = 2\oint \vec{A}.d\vec{l} = \frac{\Phi}{\Phi_0}$, where $\Phi_0 = \frac{\hbar}{2e}$ is the quantum flux and Φ the magnetic flux through the loop. The two waves are out of phase when $\frac{\Phi}{\Phi_0} \approx 1$. This condition is reached when the electrons take a longer time than τ_B to traverse the loop. This magnetic field dephasing time is defined by:

$$\Delta\Phi = \frac{4eDB}{\hbar}\tau_B \approx 1, \tag{2.7}$$

or

$$\tau_B \approx \frac{\hbar}{4eDB}. \tag{2.8}$$

Here, $2DB\tau_B$ is the average magnetic flux through the loop.

Therefore the magnetic field destroys the constructive interference, reduces the probability of backscattering and, hence, reduces the resistivity. This is the origin of the *negative magnetoresistance* observed in various disordered conductors.

More insight into the weak localization phenomenon can be gained by considering the dual $\vec{k}$-space representation introduced by Bergmann [6]. Consider an electron at initial state $\vec{k}$. After many scattering events there is a finite probability for the electron to be scattered into the final state $-\vec{k}$ (Figure 2.4). This scattering sequence is:

$$\vec{k} \rightarrow \vec{k} + \vec{g}_1 \rightarrow \vec{k} + \vec{g}_1 + \vec{g}_2 \rightarrow \cdots \rightarrow \vec{k} + \sum_{i=1} \vec{g}_i = -\vec{k}.$$

Similarly, there is also a finite probability for the electron to be scattered into state $-\vec{k}$ but in opposite sequence, i.e.

$$\vec{k} \rightarrow \vec{k} + \vec{g}_n \rightarrow \vec{k} + \vec{g}_n + \vec{g}_{n-1} \rightarrow \cdots \rightarrow \vec{k} + \sum_{i=1} \vec{g}_i = -\vec{k}.$$

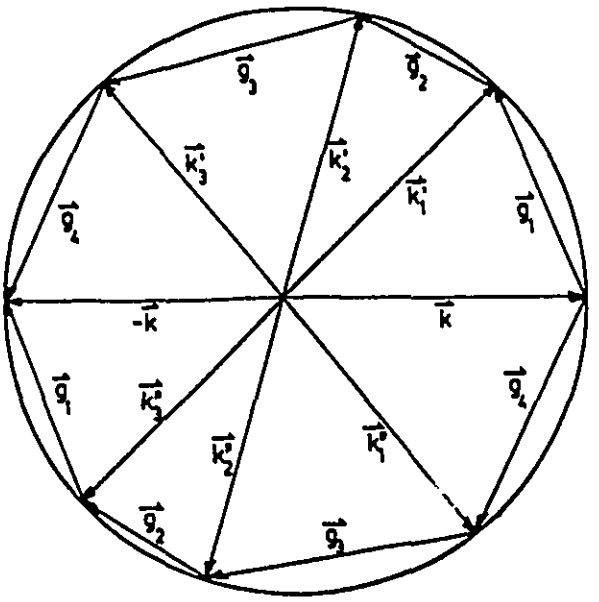

Figure 2.4: Complementary scattering sequences in $\vec{k}$-space. From reference [6].

If the individual scatterings are time-reversible and symmetric (no inelastic, spin-spin or spin-orbit scattering) the amplitudes in the final state is the same for both scattering sequences.

$$\prod_{i=1}^{n} V(\vec{q}_i) = \prod_{i=n}^{1} V(\vec{q}_i). \tag{2.9}$$

This leads, in the same way as above, to a constructive interference and therefore to an enhanced probability for the electron to be backscattered.

Up till now we have not considered in detail the effect of the spin scattering on weak localization. In fact this has important consequences on the coherent superposition of the electron wavefunctions. This is only natural since the interference involves not only the spatial part of the electron wavefunction but also its spin.

In the presence of magnetic impurities, the electron spin direction may be flipped

each time a scattering event involves a local magnetic moment and thus may return to the origin with a change in its orientation. The spin of the other partial wave, moving around the loop in the opposite direction, is also scattered by the same impurities but in the opposite sequence. Since in three dimensions, the rotation operators do not commute, the two final states are different and the interference will be progressively destroyed. The characteristic time associated with magnetic impurity scattering is denoted by τ_s. The effect of magnetic scattering on weak localization is very similar to that of inelastic scattering and it is usually very difficult if not impossible to separate the two contributions (see below and chapter 4).

On the other hand, although invariant under time-reversal, spin-orbit interaction also destroys the constructive interference but in a more subtle way. Spin-orbit interaction is a relativistic effect. A simple way to picture its origin can be expressed as follows [58]: In a coordinate system moving together with the electron in an electric field (due to the electrostatic potential of the nucleus), a magnetic field is produced by the orbiting nucleus. This magnetic field is proportional to the gradient of the electrostatic potential. It interacts with the electron spin moment and thus alters the electronic energy spectrum. According to Altshuler and Aronov the interference term around a given loop can be written, in the presence of spin-orbit interaction, as [4]:

$$C = \phi_\alpha^{(1)} \phi_\beta^{(2)} \phi_\beta^{*(1)} \phi_\alpha^{*(2)} \tag{2.10}$$

where ϕ_α and ϕ_β are the wavefunctions of the initial and final states respectively, and the superscripts 1 and 2 refer to clockwise and counterclockwise directions. The quantity C can be rewritten in a more transparent form in the total momentum representation for two particles. For spin $\frac{1}{2}$ particles this gives [4]:

$$\psi_{1,\pm 1} = \phi_\pm^{(1)} \phi_\pm^{(2)},$$

$$\psi_{1,0} = \frac{1}{\sqrt{2}} \left(\phi_+^{(1)} \phi_-^{(2)} + \phi_-^{(1)} \phi_+^{(2)} \right),$$

$$\psi_{0,0} = \frac{1}{\sqrt{2}} \left(\phi_+^{(1)} \phi_-^{(2)} - \phi_-^{(1)} \phi_+^{(2)} \right).$$

Hence

$$C = \sum_{m=-1}^{m=1} \mid \psi_{1,m} \mid^2 - \frac{1}{2} \mid \psi_{0,0} \mid^2 . \tag{2.11}$$

The first term in Eq. (2.11) contains all the information on the spin part (called triplet state, $j = 1, m = -1, 0, 1$). Because of spin-orbit scattering, it decays in time τ_{so} while the last term (called singlet state, $j = 0, m = 0$) decays in time τ_ϕ. Therefore for very short spin-orbit scattering time, $\tau_{so} \ll \tau_\phi$, the interference term becomes negative, i.e. $C = -\frac{1}{2} \mid \psi_{0,0} \mid^2$, and the total probability for the electron to be backscattered is now depressed by half from the classical one as shown by the dashed line in Figure 2.3. This phenomenon is called *weak anti-localization*. More quantitatively, the correction to the conductivity (Eq. 2.5), can be rewritten in the presence of spin-orbit scattering as [5]:

$$\frac{\Delta\sigma}{\sigma} \sim -\int_{\tau_e}^{\tau_\phi} \frac{\lambda^2 v dt}{(Dt)^{d/2}} \left(\frac{3}{2} e^{-t/\tau_{so}} - \frac{1}{2}\right) \tag{2.12}$$

which in three dimensions, yields for $\tau_{so} \ll \tau_\phi$ (strong spin-orbit scattering):

$$\Delta\sigma \simeq -\frac{1}{2} \frac{e^2}{\hbar L_\phi}. \tag{2.13}$$

As seen from the preceding equation, the spin-orbit scattering not only reverses the sign of the temperature correction to the conductivity but also reduces its magnitude by half (compare with Eq. (2.6)). Between the extreme cases of Eqs. (2.6) and (2.13) one obtains as a function of temperature, a maximum in the resistivity around $\tau_{so} \approx \tau_\phi$.

The effect of spin-orbit scattering is also reduced by the application of a magnetic field. If $\tau_B \ll \tau_{so}$, i.e. large magnetic fields, the interference is constructive and a reduction in the magnetic field (larger τ_B) increases the coherent backscattering and the resistivity [7]. If however τ_{so} is of the order of τ_B the interference is destructive and the resistivity decreases with decreasing field. In other words, in the presence of spin-orbit scattering one expects a positive magnetoresistance at low fields and a negative magnetoresistance at large fields. The maximum in the magnetoresistance occurs when $\tau_{so} \approx \tau_B$ [6, 59].

In the previous paragraphs we have presented qualitatively and semi-quantitatively the features of the weak localization phenomenon. In the following we will give the complete quantitative expressions of the weak localization correction to the conductivity.

The correction to the magnetoresistance due to weak localization has been computed by a number of authors. The most complete form was given by Fukuyama and Hoshino [22] where, in addition to spin-orbit scattering and inelastic scattering they included the splitting of the spin subbands. According to Fukuyama and Hoshino the magnetoresistance, in the limit $\tau_e \ll \tau_{so}$, τ_i and τ_s, is given by [22]:

$$\left(\frac{\Delta\rho}{\rho}\right)_{WL}(B,T) = \rho\frac{e^2}{2\pi^2\hbar}\sqrt{\frac{eB}{\hbar}}\left\{\frac{1}{2\sqrt{1-\gamma}}\left(f_3\left(\frac{B}{B_-}\right) - f_3\left(\frac{B}{B_+}\right)\right) - f_3\left(\frac{B}{B_2}\right)\right.$$
$$\left. -\sqrt{\frac{4B_{so}}{3B}}\left(\frac{1}{\sqrt{1-\gamma}}\left(\sqrt{t_+} - \sqrt{t_-}\right) + \sqrt{t} - \sqrt{t+1}\right)\right\}, \qquad (2.14)$$

where

$$t = \frac{3(B_i + 2B_s)}{4B_{so}},$$

$$t_\pm = t + \frac{1}{2}\left(1 \pm \sqrt{1-\gamma}\right),$$

$$B_\pm = B_i + 2B_s + \frac{2(B_{so} - B_s)}{3}\left(1 \pm \sqrt{1-\gamma}\right),$$

$$B_2 = B_i + \frac{2}{3}B_s + \frac{4}{3}B_{so},$$

with

$$\gamma = \left(\frac{3g^*\mu_B B}{8eD(B_{so} - B_s)}\right)^2.$$

g^* is the effective g factor and D the diffusion constant.

All the characteristic fields defined above are related to the electron-scattering times by the relation:

$$B_x = \hbar/4eD\tau_x, \qquad (2.15)$$

where τ_x is the inelastic scattering time τ_i, spin-orbit scattering time τ_{so}, and the magnetic-impurity scattering time τ_s. The dephasing field B_ϕ is defined as:

$$B_\phi = B_i + 2B_s. \tag{2.16}$$

Thus as mentioned before the field $B_\phi = \frac{\hbar}{4eD\tau_\phi}$ combines the dephasing effects due to the inelastic electron-phonon and electron-electron scattering and the spin-spin scattering (but not spin-orbit scattering).

The function $f_3(x)$ in Eq. (2.14) has been derived by Kawabata and is given by [60]:

$$f_3(x) = \sum_{n=0}^{\infty} \left(2(\sqrt{n+1+x} - \sqrt{n+x}) - \frac{1}{\sqrt{n+1/2+x}} \right). \tag{2.17}$$

It is an infinite series that converges very slowly; its asymptotic form at small and large x is:

$$f_3(x) \approx \frac{1}{48} x^{3/2}(1 - \frac{7}{64}x^2 + \cdots), \quad x \ll 1$$
$$f_3(x) \approx 0.605 - \frac{2}{\sqrt{x}}, \quad x \gg 1.$$

On the other hand, Altshuler and Aronov [4] have derived the following simpler expression:

$$\frac{\Delta\rho}{\rho} = \rho \frac{e^2}{2\pi^2\hbar}\sqrt{\frac{eB}{\hbar}} \left\{ \frac{1}{2} f_3\left(\frac{B}{B_\phi}\right) - \frac{3}{2} f_3\left(\frac{B}{B_+}\right) \right\} \tag{2.18}$$

With $B_+ \equiv B_2$ defined in Eq. (2.14).

In the preceding equation (2.18), the authors did not include the Zeeman splitting effect $g\mu_B B$ on the spin-down and spin-up bands which is expected to be important in systems with low diffusion constant, as will be demonstrated below.

It is interesting to note that in spite of its apparent complex form, the weak localization magnetoresistance expression given in Eqs. (2.14) and (2.18) is defined by only three parameters: the diffusion constant D, the spin-orbit field B_{so} and the dephasing field B_ϕ (which is however temperature dependent).

The weak localization magnetoresistance is very sensitive to the strength of spin-orbit scattering and dephasing fields. For very weak spin-orbit field i.e. $1/\tau_{so} \ll 1/\tau_\phi$,

the expressions in Eqs. (2.14) and (2.18) reduce to $-f_3(B/B_\phi)$ and the magnetoresistance is always negative. When spin-orbit scattering is of the order or stronger than inelastic scattering ($1/\tau_{so} \geq 1/\tau_\phi$) however, the expressions in Eqs. (2.14) and (2.18) are positive at low fields and negative at large enough fields. Specifically, using the asymptotic expressions of the function $f_3(x)$ given above, the magnetoresistance can be expressed as:

$$\left(\frac{\Delta\rho}{\rho}\right)_{WL} \approx -\rho\frac{e^2}{2\pi^2\hbar}\sqrt{\frac{e}{\hbar}}\frac{1}{B_\phi^{3/2}}\frac{B^2}{96} \qquad B \ll B_\phi; B_{so} \ll B_\phi$$

$$\left(\frac{\Delta\rho}{\rho}\right)_{WL} \approx \rho\frac{e^2}{2\pi^2\hbar}\sqrt{\frac{e}{\hbar}}\frac{1}{B_\phi^{3/2}}\frac{B^2}{192} \qquad B \ll B_\phi; B_{so} \gg B_\phi$$

$$\left(\frac{\Delta\rho}{\rho}\right)_{WL} \approx \rho\frac{e^2}{4\pi^2\hbar}\sqrt{\frac{eB}{\hbar}}.0.605 \qquad B_\phi \ll B \ll B_{so}$$

$$\left(\frac{\Delta\rho}{\rho}\right)_{WL} \approx -\rho\frac{e^2}{2\pi^2\hbar}\sqrt{\frac{eB}{\hbar}}.0.605 \qquad B \gg B_{so}; B_\phi$$

So as long as there is a finite spin-orbit scattering, the low field magnetoresistance will always be proportional to $+B^2$ with a slope depending on the dephasing field B_ϕ. The high field magnetoresistance has a universal $-\sqrt{B}$ field dependence. However to observe the asymptotic regime depends on the size of B_{so}. If B_{so} is very large, the magnetoresistance will remain positive for all magnetic fields that are attainable in the laboratory.

Figures 2.5-6 illustrate the expected behavior of the weak localization magnetoresistance for different values of τ_ϕ, τ_{so}, and τ_s using the Fukuyama and Hoshino expression (Eq. 2.14). The values of the resistivity ρ and the diffusion constant D are those of the $Ca_{70}Al_{30}$ alloy, a typical high resistivity amorphous alloy [18, 19].

Figure 2.7 is a comparison between Fukuyama and Hoshino expression (Eq. 2.14) and that of Altshuler and Aronov (Eq. 2.18) for different sets of the diffusion constant D and spin-orbit scattering field B_{so}. The value $D = 8\text{cm}^2/\text{s}$ is typical of low resistivity sp—band amorphous metals, such as $Ca_{70}Mg_{30}$ [18], whereas $D = 0.3\text{cm}^2/\text{s}$ is characteristic of d—band amorphous alloys or icosahedral alloys. As may be seen, for large values of D, both expressions give the same result. But for low diffusion

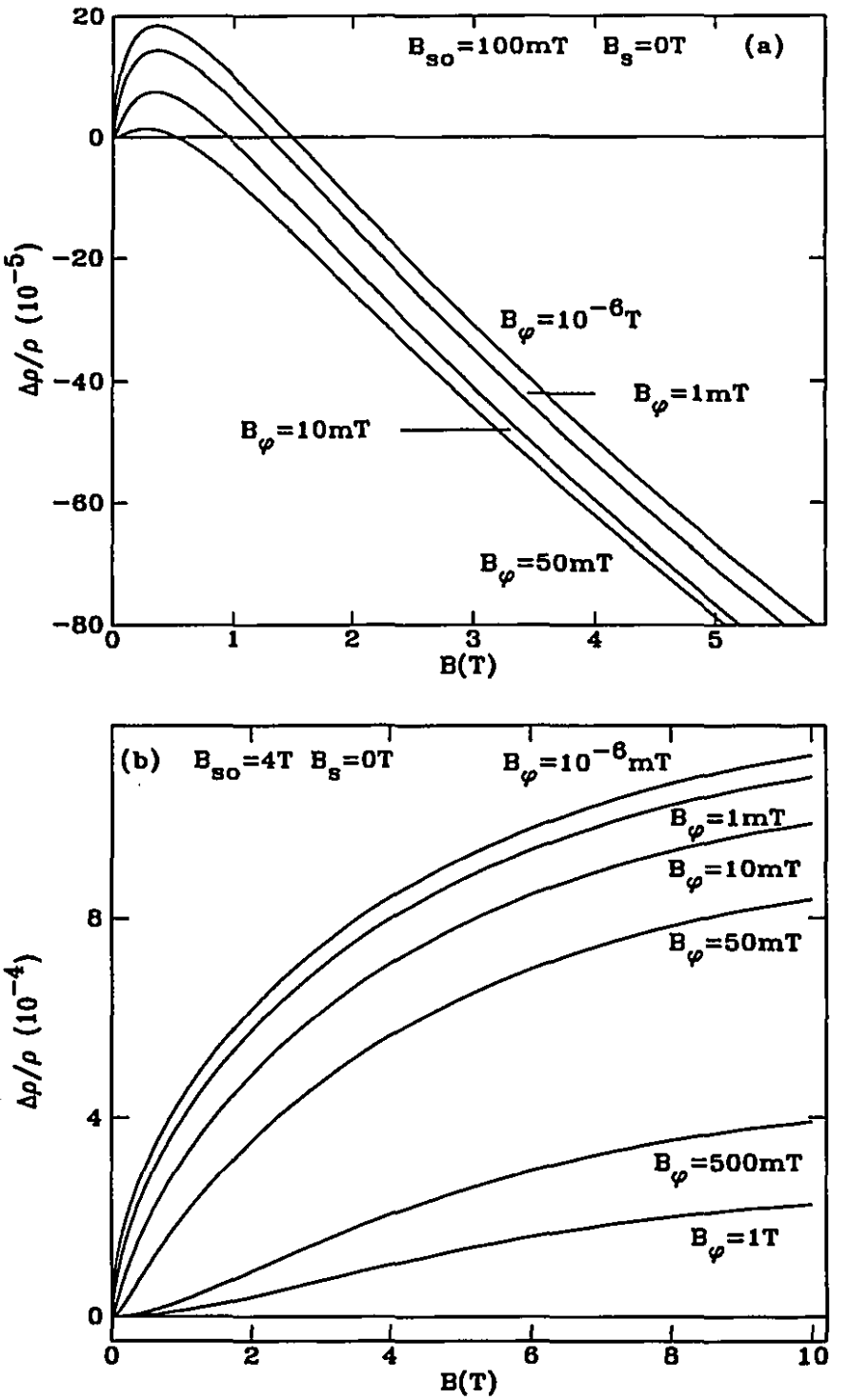

Figure 2.5: Normalized weak localization magnetoresistance (Eq. 2.14) for different dephasing fields B_ϕ, at constant; (a) weak and (b) strong spin-orbit scattering. $\rho = 300\mu\Omega$.cm, $D = 1.5\text{cm}^2/\text{s}$.

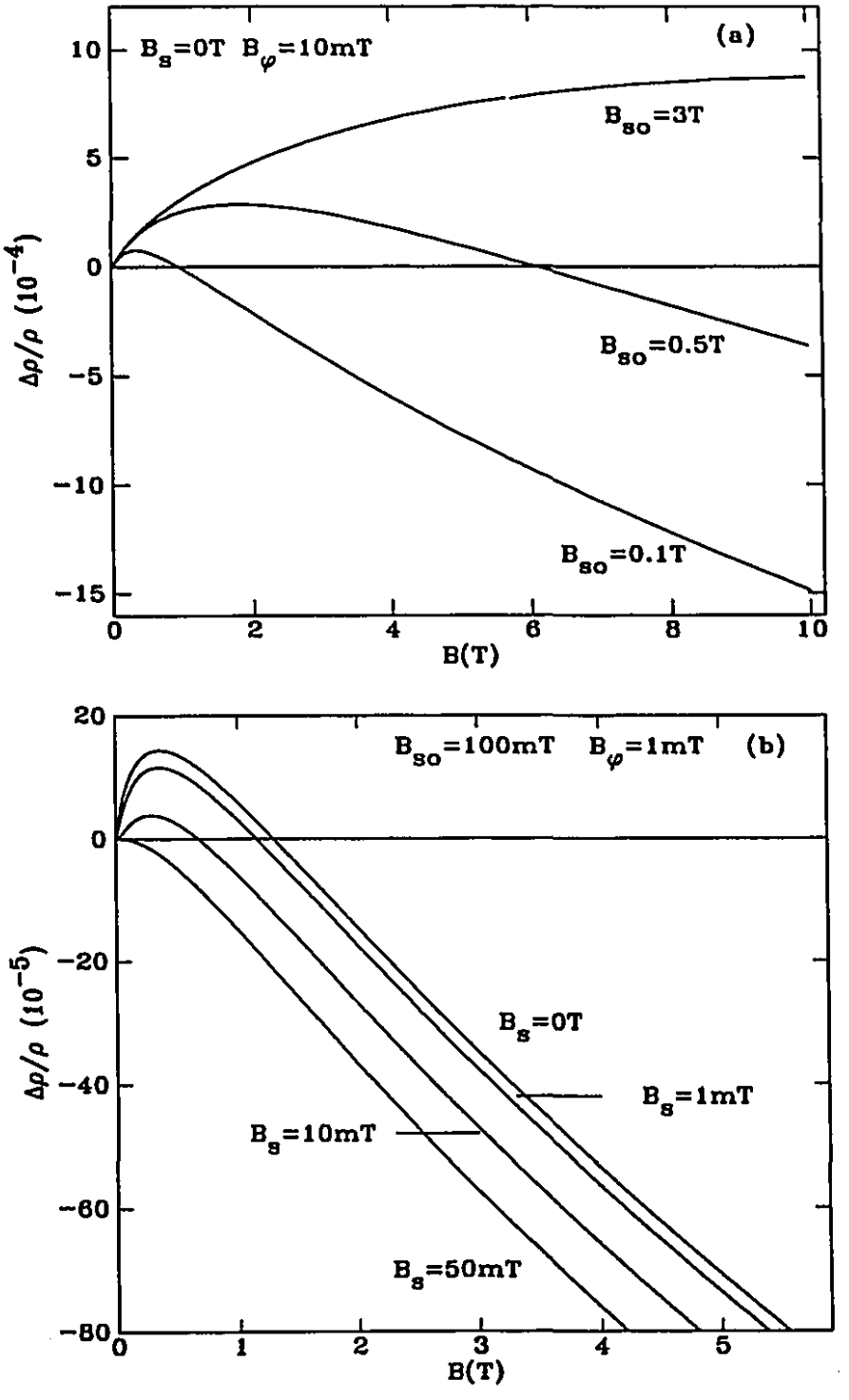

Figure 2.6: Normalized weak localization magnetoresistance (Eq. 2.14) for variable, (a) spin-orbit field B_{so} and (b) magnetic spin scattering B_s, at constant dephasing field B_ϕ. $\rho = 300\mu\Omega$.cm, $D = 1.5\text{cm}^2/\text{s}$.

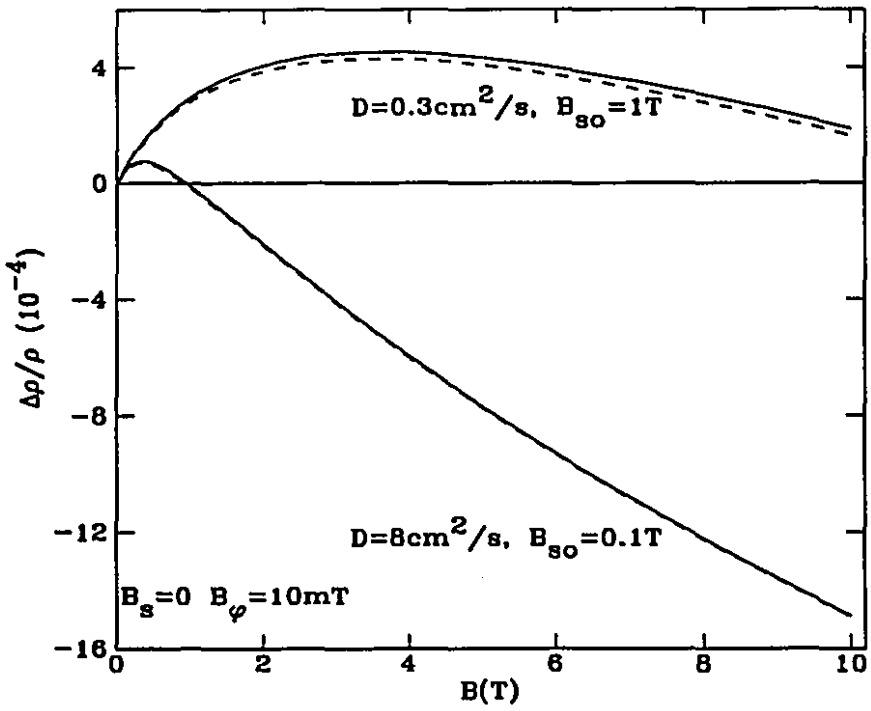

Figure 2.7: Normalized weak localization magnetoresistance (Eq. 2.14) for different values of the diffusion constant and spin-orbit scattering field; $\rho = 300\mu\Omega$.cm, $B_\phi = 10$mT. Solid line (Eq. 2.14) and dashed line (Eq. 2.18). For a large diffusion constant the two expressions give the same results.

constant, the Zeeman splitting effect plays an important role and the two expressions may differ substantially. The physical origin of the Zeeman splitting effect can be explained as follows: The dephasing through the phase-shift due to the magnetic field is proportional to the area of the closed loops and hence proportional to $L_\phi^2 = D\tau_\phi$. On the other hand, the dephasing due to Zeeman splitting in the presence of spin-orbit scattering depends on the number of spin-orbit scatterers along the loop and is therefore proportional to the length of the loop $v_F\tau_\phi$. It follows that for small D ($\leq 2\text{cm}^2/\text{s}$) the dephasing effect of the field is comparable or less than the Zeeman splitting dephasing, whereas for large diffusivities, ($D \geq 5\text{cm}^2/\text{s}$), the later effect is negligible.

In the absence of a magnetic field, the complete correction to the conductivity from weak localization in three dimensions reduces to [22]:

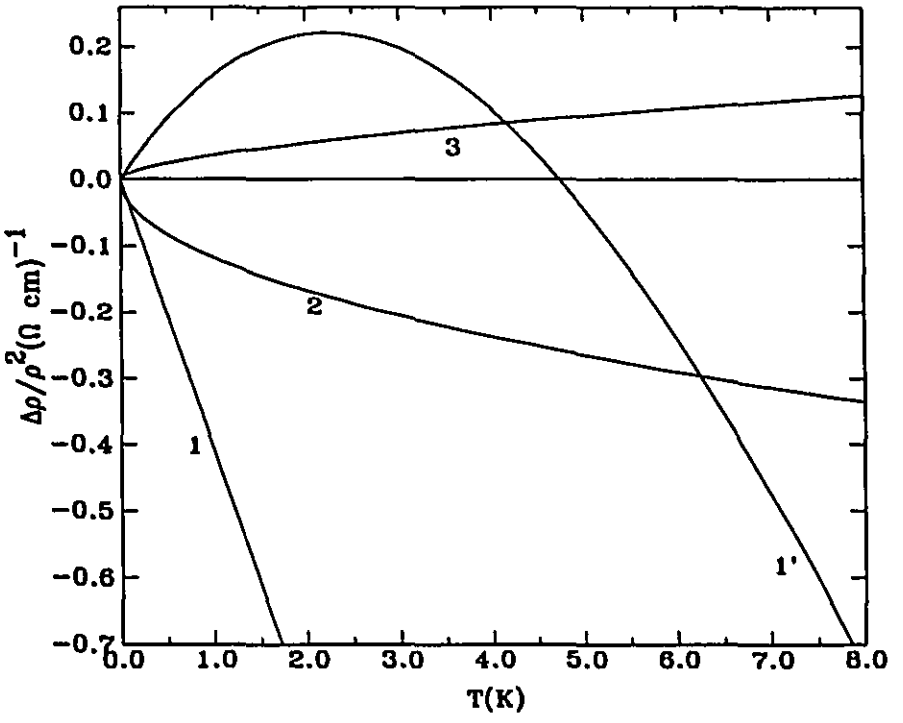

Figure 2.8: Normalized quantum corrections to the resistivity as a function of temperature for different values of B_ϕ and B_{so}.
1) Weak localization contribution, Eq. (2.19), $B_{so} = 0$.
1') Weak localization contribution, Eq. (2.19), B_{so} large.
2) Diffusion channel contribution, Eq. (2.33), see subsection 2.2.1.
3) Cooper channel contribution, Eq. (2.35),see subsection 2.2.2.

$$\left(\frac{\Delta\rho}{\rho}\right)_{WL}(T) = \rho\frac{e^2}{2\pi^2\hbar}\left(\sqrt{B_\phi} - 3\sqrt{\frac{4}{3}B_{so} + B_\phi}\right). \tag{2.19}$$

Representative plots for different sets of τ_{so} and τ_ϕ are shown in Figure 2.8 together with other temperature dependent corrections to the conductivity from the electron-electron interaction presented in the next section.

To complete this section, we give in the following the different theoretical expressions of the characteristic times introduced in the discussion of weak localization phenomenon.

2.1.1 Elastic relaxation time τ_0

The time τ_e represents the electron relaxation time as found classically from the conductivity, $\sigma = \frac{ne^2\tau_e}{m}$. In our amorphous Ca-Al alloys, $n \approx 10^{22}$electrons/cm^3 and $\rho = 300\mu\Omega$.cm, τ_e is approximately 10^{-15}s. For Al-Cu-Fe quasicrystalline alloys, $n \sim 6 \times 10^{20}$electrons/cm^3 [43, 44] and $\rho = 4500 - 10000\mu\Omega$.cm, τ_e is also of the order of 10^{-15}s. This value of τ_e is the time between scatterings of the electron by the impurities and defects present in the system and is not expected to change much with temperature (less than 20% for Ca-Al alloys and at most a factor of two for Al-Cu-Fe alloys).

2.1.2 Inelastic scattering time τ_i

According to Takayama [61] the inelastic scattering rate due to electron-phonon scattering at low temperatures is given by:

$$\frac{\hbar}{\tau_i^{ep}} = \frac{2\pi^2\lambda}{3mD}\frac{(k_BT)^2}{k_B\theta_D} + \frac{3\pi\hbar\ln 2}{(3mD)^2}k_BT, \tag{2.20}$$

where $\lambda \approx \mathcal{O}(1)$ and θ_D the Debye temperature. At 4.2 K, $1/\tau_i^{ep}$ is of the order of 10^{11}s^{-1}. On the other hand Chakravarty and Schmid [5] have recently presented a more careful calculation of the inelastic electron-phonon scattering rate in which the temperature exponent can take values anywhere between 2 and 4. They separated the contributions due to longitudinal and transverse phonons and found in the first case $p = 3$ or 4. For transverse phonons p is equal to either 2 or 4. Thus depending on the phonon modes involved in the scattering and their relative velocities of sound, p can vary between 2 and 4, as stated above.

For electron-electron scattering, Schmid [62] has given a general expression for the scattering rate in three dimensional disordered metals and it can be expressed as [62] :

$$\frac{1}{\tau_i^{ee}} = \frac{\pi}{8}\frac{(k_BT)^2}{\hbar E_F} + \frac{\sqrt{3}}{2}(k_Fl_e)^{-3/2}\frac{(k_BT)^{3/2}}{\hbar\sqrt{E_F}}, \tag{2.21}$$

where E_F is the Fermi energy and $(k_Fl_e)^{-1}$ the disorder parameter. A similar expression has also been derived by Altshuler and coworkers [4, 63]. The first term involves

scatterings with large energy transfers and is expected to dominate in weak disorder while the last term involving small energy transfers should dominate in the strong disorder limit.

It is important to note that though in most cases the inelastic scattering time (due to electron-phonon or electron-electron scattering) is identical to the dephasing time they are in principle different, even when the contribution from magnetic spin scattering is not included (see Eq. 2.16). According to Altshuler *et al.* [4] and also to Chakravarty and Schmid [5], the effectiveness of energy transfer in the scattering process has to be taken into account. Processes with small energy transfers, which give rise for example to the $T^{3/2}$ in $1/\tau_{ee}$, are less efficient in destroying the phase coherence of the electron wavefunction whereas in the calculation of the inelastic scattering time all energy transfers are weighted equally [64]. For inelastic electron-phonon scattering the correction to τ_ϕ is negligible and the distinction between $1/\tau_\phi$ and $1/\tau_i^{ep}$ is unnecessary [65].

2.1.3 Spin-orbit scattering time τ_{so}

This relaxation time refers to the time between two spin rotations due to spin-orbit interaction and was derived by Werthamer *et al.* as [66, 67]:

$$\frac{1}{\tau_{so}} = \frac{8\pi}{3\hbar} n_i N_b(E_F) \mid \langle M_{so} \rangle \mid^2, \tag{2.22}$$

where n_i is the density of spin-orbit scattering centers, $N(E_F)$ the density of states at the Fermi level and $\langle M_{so} \rangle$ is the average of the spin-orbit scattering matrix element. In a hydrogen-like picture the matrix element varies as Z^4/n^3, Z being the atomic number and n the principal quantum number of the orbit [68]. Therefore one expects a strong dependence of $1/\tau_{so}$ on the concentration of any heavy elements present in the alloy. Typically, the spin-orbit scattering rate varies from 10^{10}s^{-1}, in pure Mg to about $5 \times 10^{13}\text{s}^{-1}$ in pure Au [11].

2.1.4 Magnetic spin scattering time τ_s

The characteristic time τ_s is associated with spin-flip scattering by magnetic impurities and is generally given by Fermi's golden rule as:

$$\frac{1}{\tau_s} = c\frac{2\pi}{\hbar}N(E_F)\Omega J^2 S(S+1). \tag{2.23}$$

c is the magnetic impurity concentration, Ω the atomic volume, J the spin exchange integral and $S(S+1)$ the degeneracy of the magnetic spin state S. In Ca-Al alloys only manganese is expected to hold a moment. Taking appropriate values of $S = 2.5$ and $J = -0.24$eV [69, 70][1], $1/\tau_s$ is found to be of the order of $2.4 \times 10^9 s^{-1}$ per ppm of manganese.

2.2 Enhanced electron-electron interaction

In this section we present briefly the physical origin of the enhanced electron-electron interaction in disordered conductors. In contrast to the weak localization effect which is a direct result of quantum interference, the enhanced electron-electron interaction is an indirect effect of quantum interference. As a result, the details of the processes that lead to the corrections to the conductivity are considerably more complex. A full discussion of the theory is beyond the scope of this work, and only the final results will be given. And as in the case of weak localization the reader is referred to the review articles on the subject [4, 54] for further details.

As pointed out before, due to intense elastic scattering the electron motion in a disordered conductor is diffusive instead of being ballistic as it is the case in a well ordered conductor. Under such circumstances the screening of the electron's Coulomb potential is reduced when compared to that in a crystalline metal and thus the electrons experience a stronger interaction which is said to be *enhanced*. Therefore one expects the fundamental properties of disordered systems, such as amorphous metals for example, to be greatly affected.

[1] These values correspond to a free Mn^+ ion.

The disorder produces two important contributions to the interaction between the electrons. The first effect is due to an interference between electrons with wavevectors $\vec{k}$ and $\vec{k'}$ such that $\vec{k'} = \vec{k} + \vec{q}$ [71]. In analogy with Cooper pairs in the theory of superconductivity, this term is called "Cooper channel" or "particle-particle channel". The second contribution arises from modification in the matrix elements of the interaction between the electrons due to the absence of translation symmetry in disordered systems. This situation describes the interaction between an electron and a hole with wave vectors $\vec{k}$ and $\vec{k'}$ with $\vec{k'} = \vec{k} + \vec{q}$. This contribution is often referred to as "diffusion channel" or "particle-hole channel" contribution.

Before presenting the corrections to the conductivity resulting from the above effects it is worth mentioning the transparent physical interpretation of electron-electron interaction in disordered conductors introduced by Bergmann [71]. In this model, the phase coherence of an electron with wavevector $\vec{k}$ (returning to the origin) is re-established through the interaction of this electron with a wave charge that was created by another electron of wavevector $\vec{k} + \vec{q}$ which has previously traversed the closed loop and therefore contains all the phase information of the scattering events along this particular loop (see Figure 2.9). Thus the charge acts like a "hologram" but with the light flow replaced by a charge flow.

The constructive interference at the origin enhances the probability of return to the origin of the electron and therefore increases the resistivity in a similar way as weak localization phenomenon discussed in section 2.1. These remarks allow one to make the following comments on what one expects from enhanced electron electron interaction in disordered systems:

1- The maximum contribution is obtained when the energy difference between the interacting electrons is small, so that the phase coherence is maintained around the loops.

2- Any alteration of the phase coherence by inelastic scattering, magnetic spin scattering etc, leads to the destruction of the enhanced interaction. In particular, inelastic scattering progressively destroys these effects as it increases with increasing

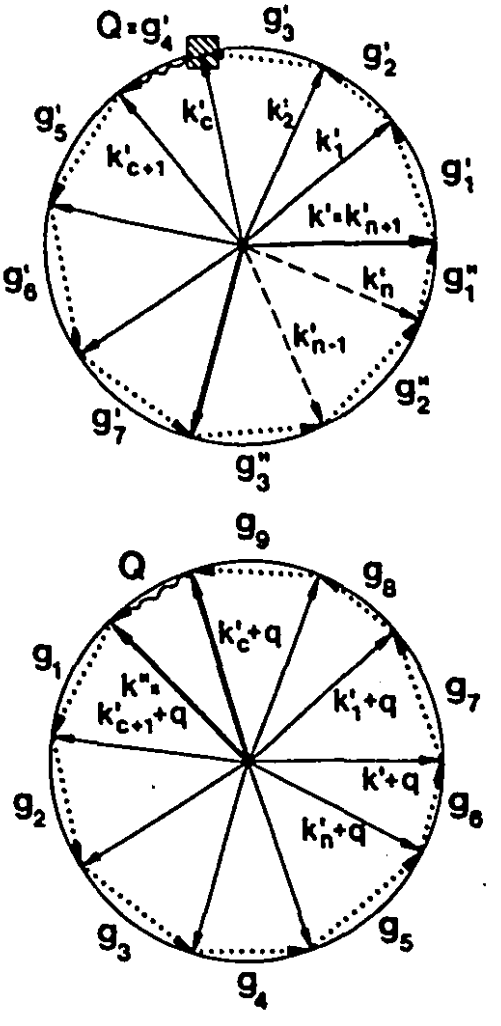

Figure 2.9: The charge hologram due to Bergmann [71]. The lower part shows the scattering series which generates a charge pattern. The upper part shows the electron which is scattered by the charge pattern. The two scattering sequences contain almost the same momenta and differ only by small Q, thus ensuring conservation of phase coherence.

temperature.

3- In the presence of a magnetic field, the phase shift is the same for the electron and the "charge hologram". Therefore to a first order, no change will occur in the interference pattern at low magnetic fields.

2.2.1 Diffusion channel correction to the resistivity

According to Lee and Ramakrishnan [3] and Altshuler and Aronov [4], the various contributions to the conductivity in the diffusion channel may be characterized by the total spin (j) of the interacting electrons together with its projection (m).

As noted above, the correction to the conductivity is due to interaction between electrons that are nearby in energy. In the presence of magnetic field, the triplet term ($j = 1,\ m = -1, 0, 1$) is divided into $m = 0$ and two $m =\mid 1 \mid$ terms. The singlet ($j = 0,\ m = 0$) and the triplet ($j = 1,\ m = 0$) terms involve interaction of electrons with the same spin and are unaffected by the spin splitting. In a magnetic field, the total correction to the resistivity can be written as a sum of two terms [3],

$$\left(\frac{\Delta\rho}{\rho}\right)_{DC}(B,T) = \left(\frac{\Delta\rho}{\rho}\right)_{DC1}(T) + \left(\frac{\Delta\rho}{\rho}\right)_{DC2}(B,T). \tag{2.24}$$

The first term represents the field-independent singlet and $m = 0$ triplet contribution and is given, in three dimensions, by [3]:

$$\left(\frac{\Delta\rho}{\rho}\right)_{DC1}(T) = -\rho\frac{0.915e^2}{4\pi^2\hbar}\left(\frac{4}{3} - \frac{1}{2}\tilde{F}_\sigma\right)\sqrt{\frac{k_BT}{\hbar D}}, \tag{2.25}$$

where $\tilde{F}_\sigma$ is the interaction constant which depends on the details of the electron screening and the Fermi surface of the conductor under consideration. It is given by [4, 3]:

$$\tilde{F}_\sigma = -\frac{32}{3F}\left(1 + \frac{3F}{4} - \left(1 + \frac{F}{2}\right)^{\frac{3}{2}}\right), \tag{2.26}$$

with

$$F = \frac{\int d\Omega V(q = 2k_F\sin\theta/2)}{\int d\Omega V(q = 0)}. \tag{2.27}$$

$V(q)$ is the Fourier transform of the statistically screened Coulomb potential, Ω a solid angle on the Fermi surface. Within the Thomas-Fermi screening theory [72] one finds:

$$F = \frac{\ln(1+x)}{x}, \tag{2.28}$$

where $x = \left(\frac{2k_F}{k_s}\right)^2$. k_s is the inverse screening length and k_F the Fermi wavevector. For complete screening (k_s large) $F \approx 1$ and for no screening (k_s small) $F \approx 0$ and in this case expression (2.26) becomes $\tilde{F}_\sigma \approx F$.

The second term in Eq. (2.24) is the $m = \pm 1$ triplet contribution which is field-dependent. Its field dependence has been calculated by Lee and Ramakrishnan and can be written as [3, 73]:

$$\left(\frac{\Delta\rho}{\rho}\right)_{DC2}(B,T) = \rho\frac{e^2}{2\pi^2\hbar}\sqrt{\frac{eB}{\hbar}}\frac{\tilde{F}_\sigma}{2\sqrt{\pi}}\sqrt{\frac{\pi k_B T}{2eDB}}g_3\left(\frac{g\mu_B B}{k_B T}\right), \tag{2.29}$$

with

$$g_3(x) = \int_0^\infty d\omega \left(\frac{d^2}{d\omega^2}(\omega N(\omega))\right)\left(\sqrt{\omega+x}+\sqrt{\omega-x}-2\sqrt{\omega}\right) \tag{2.30}$$

and $N(\omega) = 1/(e^\omega - 1)$. Details for the evaluation of the function $g_3(x)$ are given in appendix A.

The physical interpretation of the field dependence can be explained as follows: In the presence of the field, spin splitting produces a gap $g\mu_B B$ between the spin-up and spin-down subbands and therefore reduces the interaction between the electrons of these bands as noted above. Since, at $B = 0$, the interaction reduce the resistivity, the resulting magnetoresistance is positive as illustrated in Figure 2.10.

However this magnetoresistance is very sensitive to spin scattering and temperature. According to Altshuler *et al.* [4, 25] and Lee and Ramakrishnan [3], the diffusion channel contribution to magnetoresistance vanishes not only at high temperatures, but also when:

$$g\mu_B B \ll \hbar/t_s, \tag{2.31}$$

where

$$\frac{1}{t_s} = \frac{4}{3}\left(\frac{1}{\tau_s}+\frac{1}{\tau_{so}}\right) \tag{2.32}$$

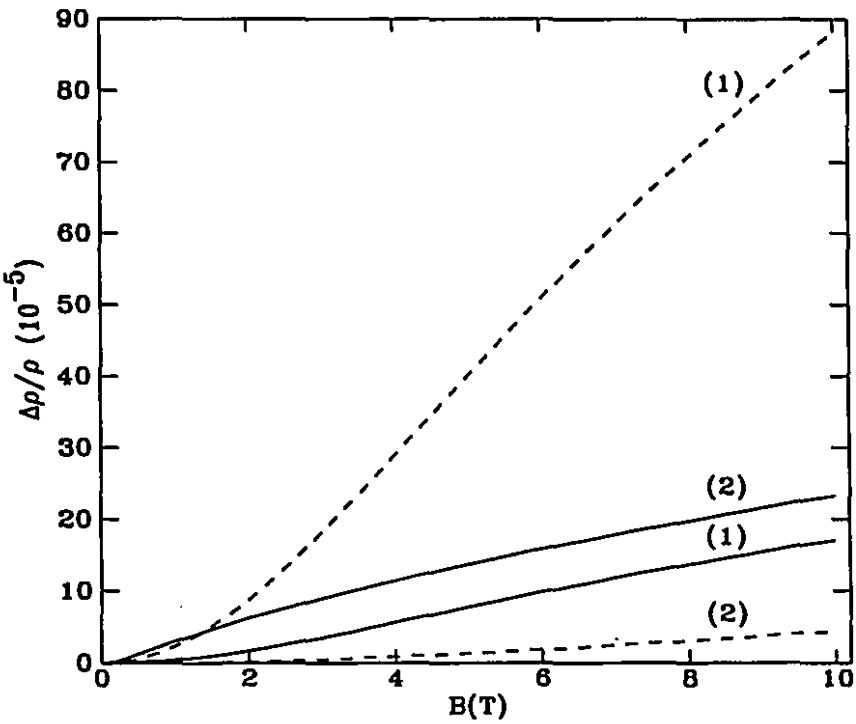

Figure 2.10: Normalized enhanced electron-electron interaction magnetoresistance for different values of D at $T = 1.5$K. Dashed line ($D = 0.3\text{cm}^2/\text{s}$) and solid line ($D = 8\text{cm}^2/\text{s}$).
1) Diffusion channel contribution, Eq. (2.29).
2) Cooper channel contribution, Eq. (2.34).

is the total spin relaxation time. This is so because spin scattering tends to mix the spin subbands and therefore destroys the effect. But to date, there has been no detailed calculation on how this suppression by spin scattering occurs and what one should expect in the intermediate spin scattering regime. From this observation comes the motivation of the present work where the diffusion channel contribution to the magnetoresistance will be investigated over wide range of spin-orbit scattering.

In the absence of a magnetic field the correction to the resistivity reduces to the following expression [3]:

$$\left(\frac{\Delta\rho}{\rho}\right)_{DC1}(T) = -\rho\frac{0.915e^2}{4\pi^2\hbar}\left(\frac{4}{3}-\frac{3}{2}\tilde{F}_\sigma\right)\sqrt{\frac{k_BT}{\hbar D}}, \tag{2.33}$$

which is the same as Eq. (2.25) except for the factor $\frac{3}{2}$ which is due to the multiplicity of the $j = 1$ state, replacing $\frac{1}{2}$ for $\tilde{F}_\sigma$.

2.2.2 Cooper channel correction to the resistivity

The magnetoresistance coming from the Cooper channel arises from the interactions in the particle-particle channel such that $\mid \vec{k}+\vec{k'} \mid = \mid \vec{q} \mid \ll \mid \vec{p} \mid$-i.e. small total momentum. Several authors have calculated this contribution, but their results are not consistent [4, 21] [2]. However there seems to be a consensus among workers that Isawa and Fukuyama's expression [74] is the most complete. These authors considered in detail the spin-orbit scattering effect on this contribution and concluded that it has no impact. Furthermore they explicitly included the dephasing effect of the temperature through the inelastic field B_i. In the case of non-superconductors, such as all the alloys considered in this thesis, they found [74]:

$$\left(\frac{\Delta\rho}{\rho}\right)_{CC}(B,T) = \rho\frac{e^2}{2\pi^2\hbar}\sqrt{\frac{eB}{\hbar}}\frac{3\pi^2}{2}\left(\frac{k_BT}{4eDB}\right)^2 g(T,B)\Phi_F(B,T), \tag{2.34}$$

where

$$\Phi_F(B,T) = -\sum_{k=0}^{\infty}\left(\zeta\left(\frac{5}{2},\frac{1}{2}+\frac{k+\gamma}{k\gamma}\right)-\frac{2}{3}\left(\frac{\gamma h}{k+\gamma}\right)^{\frac{3}{2}}\right),$$

[2] Different expressions were given by Altshuler *et al.* [21] and Altshuler and Aronov [4]

$$\gamma = \frac{2eDB_i}{\pi k_B T} \qquad h = \frac{B}{B_i}.$$

ζ is the generalized Riemann zeta function.

$g(T,B)$ is the coupling constant and is given by:

$$g(T,B) = \frac{1}{\frac{2}{F} + \ln\left(\frac{1.13T_F}{T^*}\right)},$$

with

$$T^* = max\left(T, \frac{4eDB}{k_B}\right),$$

T_F is the Fermi temperature.

It should be noted that the above expression for the coupling constant $g(T,B)$ is not exact. It is correct only to lowest order in B/T and a complete form remains to be derived.

The Cooper channel magnetoresistance as predicted by Eq. (2.34) is shown in Figure 2.10. For low diffusion constant it represents less than 10% of the diffusion channel contribution. Moreover, it would be reduced even further if Zeeman splitting and magnetic spin scattering (which decrease the Cooper channel magnetoresistance), were to be included in the derivation. It is for this reason that the Cooper channel contribution will not be included in the analysis of the experimental data presented in Chapter 4. However, for the sake of completeness we give here the correction to the temperature dependence of the resistivity coming from the Cooper channel. It is given by the following expressions [74]:

$$\left(\frac{\Delta\rho}{\rho}\right)_{CC}(T) = \rho\frac{0.915e^2}{2\pi^2\hbar}\left(\frac{2}{\ln\frac{T_F}{T}}\right)\sqrt{\frac{k_BT}{\hbar D}}. \tag{2.35}$$

2.3 Magnetic impurity scattering contribution to the magnetoresistance

Magnetic impurities contribute to the magnetoresistance in disordered conductors in two ways. As mentioned in section 2.1, spin-flip scattering of conduction electrons

by such impurities destroys the phase coherent backscattering responsible for weak localization, and so reduces the quantum correction to the magnetoresistance. The magnetic spin scattering rate is given in subsection 2.1.3.

The second contribution comes from the field and temperature dependence of single-site magnetic scattering. The states available to the impurity are progressively frozen out with increasing field giving rise to a magnetoresistance. This magnetoresistance has been calculated to second order in the exchange integral by Béal-Monod and Weiner and is given by [70]:

$$\left(\frac{\Delta\rho}{\rho}\right)_{mag} = kJ^2A(\alpha), \tag{2.36}$$

where

$$k = \frac{c}{\rho}\frac{3\pi m\Omega}{2\hbar e^2 E_F},$$

$$A(\alpha) = 4\langle S_z\rangle^2 + \langle S_z\rangle\left(\coth(\alpha/2) - \frac{\alpha/2}{\sinh^2(\alpha/2)}\right),$$

$$\alpha = \frac{g\mu_B B}{k_B T},$$

$$\langle S_z\rangle = \frac{M}{g\mu_B n} = SB_s(S\alpha).$$

$B_s(S\alpha)$ is the Brillouin function, Ω the atomic volume of the host alloy, c the concentration of impurities, and n the number density of the impurities.

The above equation describes a magnetoresistance which is proportional to $-B^2$ at low fields and saturates at high fields. It is important to note that both $1/\tau_s$ and $\left(\frac{\Delta\rho}{\rho}\right)_{mag}$ are proportional to cJ^2 so that small concentrations of magnetic impurities may give a non-negligible contribution to both dephasing and magnetoresistance. A representative plot of $\left(\frac{\Delta\rho}{\rho}\right)_{mag}$ is included in Figure 2.11 at $T = 1.5$K and $T = 10$K together with the other contributions.

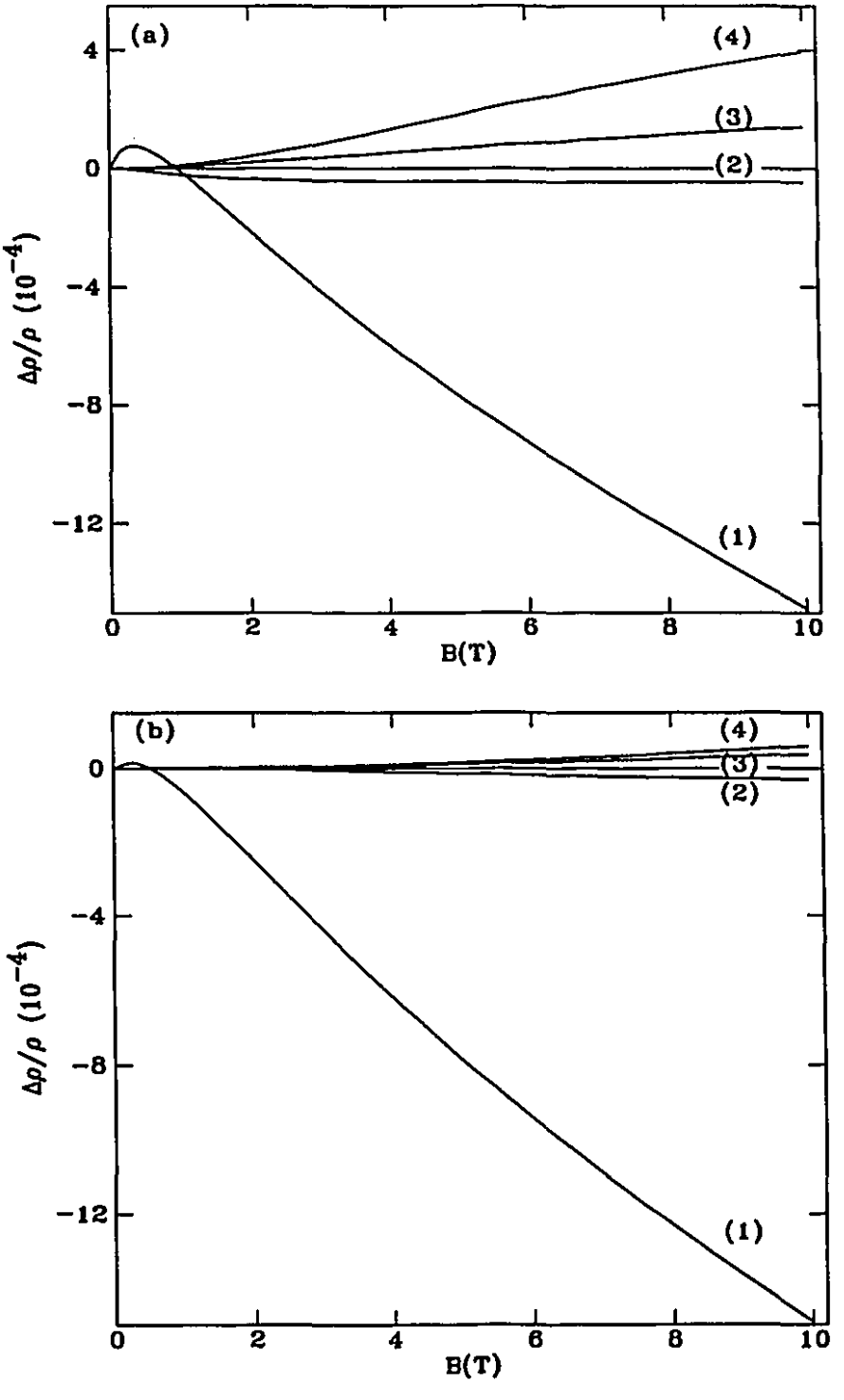

Figure 2.11: Normalized magnetoresistance for $\rho = 300\mu\Omega$.cm, $D = 1.5\text{cm}^2/\text{s}$, $B_{so} = 0.1\text{T}, B_\phi = 10\text{mT}$. (a) $T = 1.5\text{K}$ and (b) $T = 10\text{K}$.
1) Weak localization contribution, Eq. (2.14).
2) Magnetic impurity scattering contribution, Eq. (2.36), $c = 50\text{ppm}$, $J = -0.24\text{eV}$.
3) Electron-electron interaction contribution from the Cooper channel, Eq. (2.34).
4) Electron-electron interaction contribution from the diffusion channel, Eq. (2.29).

2.4 Applications to amorphous Ca-Al-(Ag,Au) and icosahedral Al-Cu-Fe systems

First we start with the amorphous Ca-Al-(Ag,Au) system. As mentioned in Chapter 1, the Ca-Al alloys have been extensively examined both experimentally and theoretically and are in consequence very well characterized. Mizutani *et al.* [31, 32] carried out measurements of the electrical resistivity, electronic specific heat and Hall coefficient of the different alloy compositions over a wide range of temperature. The electrical resistivity is found to be strongly dependent on the Al concentration; it goes from $\sim 150\mu\Omega$.cm to $\sim 400\mu\Omega$.cm as the Al content varies from 20 to 40 at. %. The density of states at the Fermi level, on the other hand, as deduced from the electronic specific heat coefficient data by the following formula:

$$N(E_F) = \frac{0.4241\gamma}{1+\lambda} \text{states/eV.atom}, \tag{2.37}$$

where γ is the electronic heat coefficient in mJ/mole.K^2 and λ the electron-phonon coupling constant, decreases with increasing Al concentration.

For the present alloys of $Ca_{70}Al_{30-x}(Ag,Au)_x$, the resistivity varies only slightly with the alloy composition except at large concentrations of Ag and Au (i.e. 2 and 3 at.%) where it decreases by up to 30%. Except for $Ca_{70}Al_{30}$, there is no available data on the density of states at the Fermi level for the remaining alloys and we assume it to stay constant (i.e. the same as for $Ca_{70}Al_{30}$, ≈ 0.49 states/eV.atom [31, 32]) since we do not expect it to change significantly upon substitution of Al by small amounts of Ag or Au. This assumption is supported by the results of Ca-Mg-Al [32], where the density of states, as deduced from specific heat measurements, only changes by $\sim 7\%$ when going from $Ca_{70}Al_{30}$ to $Ca_{70}Mg_{10}Al_{20}$. At the same time the resistivity spans the same range of values as that observed in the present alloys.

The disorder parameter, $(k_F l_e)^{-1}$ can be calculated from the measured resistivity and the density of states. If we assume an $sp-$band structure for our alloys, which is consistent with the theoretical calculations of Hafner and Jaswal [75] on Ca-Al

compounds, then $(k_F l_e)^{-1}$ is given by the following formula:

$$(k_F l_e)^{-1} = \frac{\hbar e^2}{3m} N(E_F)\rho, \tag{2.38}$$

Using our results for the resistivity and the density of states calculated from Mizutani *et al.* data [31, 32], for $Ca_{70}Al_{30}$ we find, $(k_F l_e)^{-1} \sim 0.25 - 0.35$. This value of the disorder parameter reflects a relatively high degree of disorder and in this case, as noticed in Chapter 1, the plane wave description breaks down as the wavevector of the conduction electrons is not well defined. In fact when $(k_F l_e)^{-1} \approx 1$, we have $\Delta k \approx k$ (uncertainty principle). Therefore, a priori one does not expect the weak localization and enhanced electron-electron interaction expressions (Eqs. 2.14 and 2.29), which were derived for the case $(k_F l_e)^{-1} \ll 1$, to give an accurate account of the experimental data in Ca-Al-(Ag,Au) system. However, the author in an earlier study of Ca-Mg-Al system where the disorder parameter was varied from very low (~ 0.05) to the present value (i.e. ~ 0.35) showed that, in this range, the quantum corrections to the conductivity provide an excellent description of the data irrespective of the exact value of $(k_F l_e)^{-1}$ [18, 19]. The only difference between the Ca-Mg-Al alloys and the present Ca-Al-(Ag,Au) alloys is the level of the spin-orbit scattering. The former system is characterized by a very weak spin-orbit scattering [18, 19] whereas in the later spin-orbit scattering is varied from very weak to very strong. Therefore a quantitative investigation of the quantum corrections to the conductivity in Ca-Al-(Ag,Au) will also provide a test of the validity of the current weak localization and enhanced electron-electron interaction expressions in the strong spin-orbit regime.

The quantum corrections to the conductivity expressions are defined by B_ϕ, B_{so}, $\tilde{F}_\sigma$ and D. The last two parameters are known; $\tilde{F}_\sigma$ is simply given by the free-electron Thomas-Fermi screening theory and is ≈ 0.52 for Ca-Al-(Ag,Au) alloys. The diffusion constant on the other hand is calculated by the Einstein relation (see Table 2.1):

$$D = \frac{1}{e^2 N(E_F)\rho}. \tag{2.39}$$

Since $N(E_F)$ is assumed to be the same for all the samples, the changes in the diffusion constant are a consequence of the changing resistivity only.

In the light of the earlier work on Ca-Mg-Al [30, 18, 19], the following predictions can be made about the low temperature magnetoresistance and resistivity temperature dependence of Ca-Al-(Ag,Au) alloys. Due to finite spin-orbit scattering the magnetoresistance will be positive at low fields for all samples. At high fields it is expected to either change sign or stay positive depending on the Ag or Au concentration. Because of the low diffusion constant the Zeeman band-splitting effect on the weak localization magnetoresistance should be important. The enhanced electron-electron interaction contribution will be positive and should be significant only at large field values and low temperature ($T \leq 6$ K) (see Figure 2.11). For the temperature dependence of the resistivity however, electron-electron interaction contribution is expected to dominate.

Application of the quantum corrections to the conductivity theories to Al-Cu-Fe quasicrystals is less obvious. Due to their recent discovery, many physical properties of quasicrystals in general and of this system in particular, are not completely understood and are still under intensive investigation both theoretical and experimental. The second part of the thesis is motivated by the desire to gain further information on the electronic properties of the icosahedral Al-Cu-Fe system. Applying quantum corrections to the conductivity theories to analyze the low temperature resistivity provides a way to answer (at least partly) the question: Are icosahedral Al-Cu-Fe alloys ordered or disordered?.

To use weak localization and enhanced electron-electron interaction theories in a quantitative analysis of the icosahedral Al-Cu-Fe data we need, at least, to know the diffusion constant D. This can be determined with the help of equation (2.39). However only the density of states for $Al_{63.5}Cu_{24.5}Fe_{12}$ is known from experiment [43, 44] and we therefore assume, in contrast to Ca-Al-(Ag,Au) alloys, that $N(E_F)$ remains the same for all Al-Cu-Fe samples. Thus the change in the resistivity is a result of the varying $N(E_F)$. This assumption is very reasonable if we consider that a

Alloy	d (g/cm^3)	ρ ($\mu\Omega$.cm)	D (cm^2/s)	$N(E_F)$ (st/eV.at)
$Ca_{70}Al_{30}$	1.85 ± 0.04	310 ± 16	1.5	0.49
$Ca_{70}Al_{29.7}Ag_{0.3}$	1.84 ± 0.04	264 ± 13	1.8	-
$Ca_{70}Al_{29.3}Ag_{0.7}$	1.84 ± 0.04	270 ± 13	1.7	-
$Ca_{70}Al_{28}Ag_2$	1.92 ± 0.04	245 ± 12	1.94	-
$Ca_{70}Al_{29.9}Au_{0.1}$	1.86 ± 0.04	297 ± 15	1.56	-
$Ca_{70}Al_{29.8}Au_{0.2}$	1.86 ± 0.04	280 ± 14	1.66	-
$Ca_{70}Al_{29.6}Au_{0.4}$	1.87 ± 0.04	280 ± 14	1.66	-
$Ca_{70}Al_{29.2}Au_{0.8}$	1.92 ± 0.04	290 ± 15	1.6	-
$Ca_{70}Al_{28}Au_2$	2.00 ± 0.04	220 ± 14	2.1	-
$Ca_{70}Al_{27}Au_3$	2.12 ± 0.04	210 ± 14	2.27	-
$Al_{63.5}Cu_{24.5}Fe_{12}$	4.5†	4620 ± 460	0.25	0.3
$Al_{63}Cu_{25}Fe_{12}$	4.5†	5330 ± 530	0.25	-
$Al_{62.5}Cu_{25.5}Fe_{12}$	4.5†	6700 ± 670	0.25	-
$Al_{62}Cu_{25.5}Fe_{12.5}$	4.5†	9730 ± 970	0.25	-

Table 2.1: The physical parameters of amorphous Ca-Al-(Ag,Au) and icosahedral Al-Cu-Fe samples studied in this thesis. †: from reference [42].

pseudogap in the density of states exists at the Fermi level as mentioned in Chapter 1. Note that although the resistivity is known from room-temperature measurements it will be used as a free parameter in the analysis and the results will serve as consistency check to our fitting procedure. Because of the low density of conduction electrons ($n \sim 6 \times 10^{20}$electrons/cm^3, as found from Hall coefficient measurements [43, 44]), it is questionable to calculate $\tilde{F}_\sigma$ from the Thomas-Fermi theory and will therefore be treated as a free parameter like ρ, B_{so} and B_ϕ.

Chapter 3

Experimental Techniques

The aim of this chapter is to describe the different stages of the sample preparation and characterization, and the different techniques used to measure the resistivity and its temperature and magnetic field dependence. During the preparation of the samples special attention was paid to their quality as contamination by foreign phases and/or the presence of magnetic impurities alter dramatically the electrical transport properties.

3.1 Sample preparation

The characteristics of the raw materials used in preparing the different samples are as follows:

Ca, Granule: From Rare Metallic Co. Japan.

Purity: 99.99% with 5ppm Mn, less than 18ppm Fe, 3-5ppm Ni, Co, and Cr.

Al, Rod: From McKay, New York, USA.

Purity: 99.9999%. Contaminants unknown but less than 1 ppm.

Mg, Rod: From Alfa Products, Massachusettts, USA.

Purity: m99.95% with 40ppm Mn, 20ppm Fe and 10ppm Ni.

Cu, Shot: From ASARCO Ltd. New York, USA.

Purity: 99.999% with less than 1ppm transition metal impurities.

Fe, Lump: From Atlantic Equipment Engineers, New Jersy, USA.
Purity: 99.99%.

Au, Shot: From Alfa Products (Morton Thiokol, Inc.), Massachusetts, USA.
Purity: 99.9999%.

Ag, Rod: From Johnson Matthey Chemicals Ltd. London, UK.
Purity: 99.999% with 3ppm Fe, 1ppm Cu, less than 1ppm Bi, Cd, and Mg.

3.1.1 Amorphous alloys

Prior to the preparation of the Ca-Al-X (X=Ag,Au), Al was etched with NaOH + H_2O to remove any surface contaminants. The Ca could not be treated because of its high reactivity and was used as it is. The alloys were made by induction melting appropriate amounts in a water-cooled Cu boat. Alloying was done under a high purity (99.998% pure) argon atmosphere of about 30kPa. The induction coil was powered by a high frequency LEPEL generator. In order to ensure homogeneity the ingots and the target were turned over and melted several times under the same conditions. The final mass loss was less than 2%. The nominal chemical compositions of the twelve amorphous samples used in this thesis are listed in Table 3.1.

3.1.2 Quasicrystals

The Al-Cu-Fe alloys are less reactive and were prepared in an arc furnace under a titanium-gettered argon atmosphere. Prior to alloying Cu was also etched with HNO_3 + H_2O solution to remove any surface contamination. The Fe lump was not etched because of the risk of oxidation and was only cleaned with a steel brush. To prevent evaporation of Al, which has a much lower melting temperature than Fe and Cu, the ambient pressure in the chamber was set to approximately 60kPa. The resultant buttons ($\sim$ 7g) were also melted several times for homogeneity purposes and the mass loss was very small (less than 1%).

Amorphous Alloys	Quasicrystals
$Ca_{70}Al_{30}$	$Al_{63.5}Cu_{24.5}Fe_{12}$
$Ca_{70}Al_{29.7}Ag_{0.3}$	$Al_{63}Cu_{25}Fe_{12}$
$Ca_{70}Al_{29.3}Ag_{0.7}$	$Al_{62.5}Cu_{25.5}Fe_{12}$
$Ca_{70}Al_{28}Ag_2$	$Al_{62}Cu_{25.5}Fe_{12.5}$
$Ca_{70}Al_{29.9}Au_{0.1}$	
$Ca_{70}Al_{29.8}Au_{0.2}$	
$Ca_{70}Al_{29.6}Au_{0.4}$	
$Ca_{70}Al_{29.2}Au_{0.8}$	
$Ca_{70}Al_{28}Au_2$	
$Ca_{70}Al_{27}Au_3$	

Table 3.1: The nominal chemical compositions of the amorphous and the quasicrystalline samples.

The four selected compositions (see Table 3.1) lie in the region were it has been experimentally established that a single phase icosahedral structure can be obtained as shown in the phase diagram (Figure 3.1.b) [37, 38, 76]. Although the chosen compositions are very close to each other, their electrical transport properties are very sensitive to the composition as will be discussed in the next chapter.

3.1.3 Meltspinning

Meltspinning is by far the most widely used technique for producing amorphous and quasicrystalline metals. It allows production of large quantities of material with relative ease and in suitable geometry for electrical transport measurements. In this technique the alloy is melted by induction and directed on the surface of a rapidly spinning wheel, usually made of copper. The material is spread into very thin and long ribbons and undergoes a cooling rate of $\sim 10^6$ degree/s. This process allows alloys with sufficiently deep eutectics to be quenched into the amorphous state. In Figure 3.1.a we have reproduced the phase diagram of Ca-Al [77]. One can see that

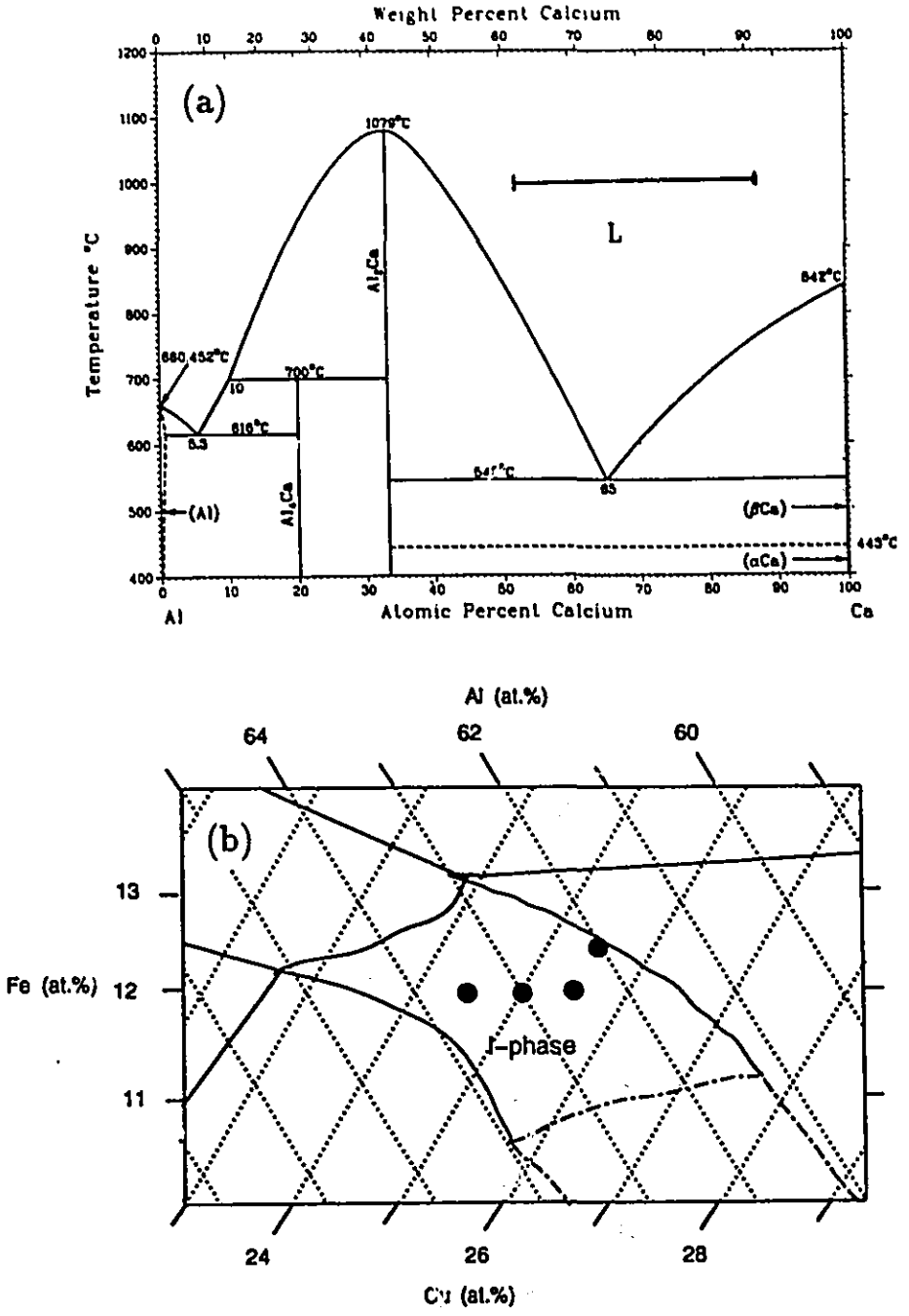

Figure 3.1: Phase diagrams,
a) Phase diagram of binary Ca-Al from reference [77]. The solid bar limits the glass forming region according to reference [78].
b) Phase diagram of Al-Cu-Fe. The dashed line limits the region of formation of icosahedral phases [37]. The solid points are the four compositions selected in this thesis.

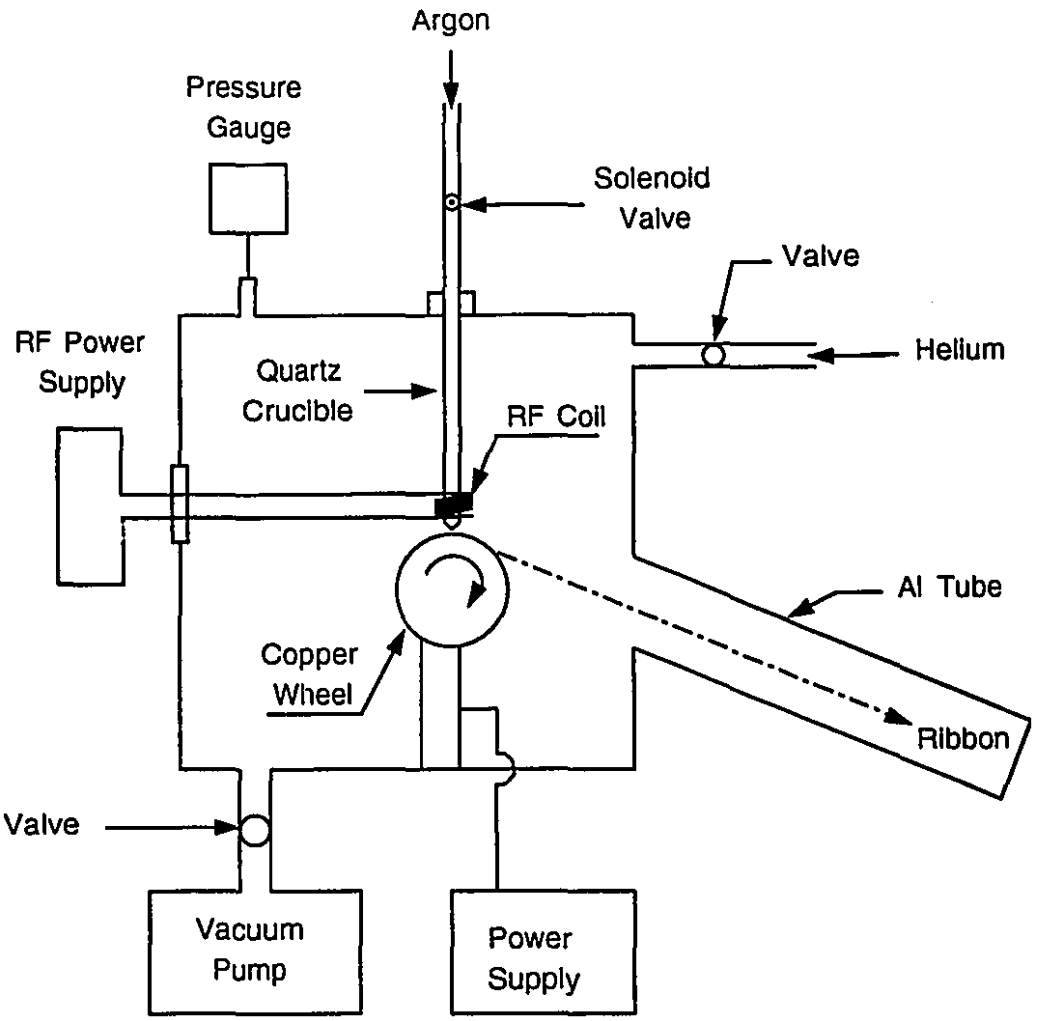

Figure 3.2: Schematic of the melt-spinning apparatus.

the $Ca_{70}Al_{30}$ composition lies in the middle of the glass forming region which extends from 12.5 to 47.5 at.% Al [78]. The substitution of Al by small amounts of Ag or Au is not expected to affect the glass forming ability of the system as was confirmed from X-ray diffraction patterns (see below). An alloy pellet of $\sim$ 0.5 g placed in a quartz tube is induction melted. The liquid is then ejected through the orifice (about 0.5 mm in diameter) onto the rotating wheel by high purity argon at a pressure of approximately 50 kPa above the atmospheric pressure. The liquid solidifies as a thin ribbon on the wheel surface and is collected in a long Al tube; see Figure 3.2. The tangential velocity was typically 42 m/s for Ca-Al-(Ag,Au) alloys and the resulting

ribbons were 1-2 mm wide, 1-1.5 meters long and about 20 microns thick. Because of the high brittleness of Al-Cu-Fe alloys the wheel speed was lowered to 25-30 m/s. This allowed preparation of relatively long ribbons (1-3 cm). To avoid oxidation and also to obtain ribbons with uniform geometry, the melt-spinning chamber was, in all cases, evacuated and back-filled with He to a pressure of 30 kPa.

In order to prevent crystallization and oxidation, the Ca-Al-(Ag,Au) ribbons were stored in liquid nitrogen (Ca reacts easily with oxygen and water). The Al-Cu-Fe on the other hand were kept in glass vials at room temperature.

3.2 Sample Characterization

3.2.1 X-ray diffraction

The main technique used to check the structure of the samples was X-ray diffraction with a Cu K_α radiation (λ = 1.5418Å). Impurity phases down to a level of 2% can be detected by this method. The configuration of the NICOLET/STOE L11 automated powder diffractometer used is shown in Figure 3.3. The beam passes through a graphite monochromator and X-rays reflected by the sample are detected with a photo-multiplier system.

A. Amorphous Alloys

The diffraction pattern of Ca-Al-(Ag,Au) samples consisted of a very broad peak a characteristic of amorphous materials as shown in Figure 3.4. However for some samples a few crystalline peaks were superposed on the amorphous background. Using the JCPDS data files [79] those peaks were identified as due to Ca oxides and hydroxides. The peaks disappeared after polishing the surface implying that they are not in the bulk of the samples but only on the surface. Their presence does therefore not affect our measurements.

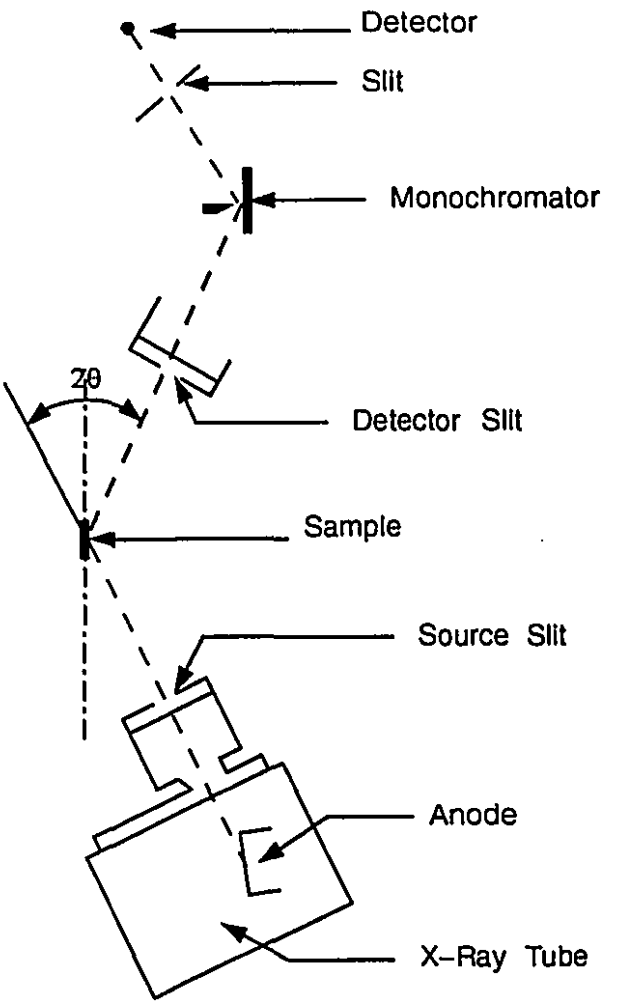

Figure 3.3: Schematic diagram of the X-ray diffractometer.

B. Icosahedral Al-Cu-Fe alloys

The as-quenched ribbons of Al-Cu-Fe always contain two phases: the icosahedral phase together with a small amount of a simple cubic Fe_3Al crystalline phase (lattice parameter $a = 2.91$Å [76]). This impurity phase however could be easily removed by high temperature annealing to obtain single phased icosahedral samples. In fact, as it may be seen in Figure 3.5.a, the FeAl crystalline peak at $2\theta = 43.9°$ disappears completely after the ribbons were annealed at 750 °C for 3 hours under vacuum. At the same time the quasicrystalline peaks become sharper indicating an improvement of the structural quality of the icosahedral phase.

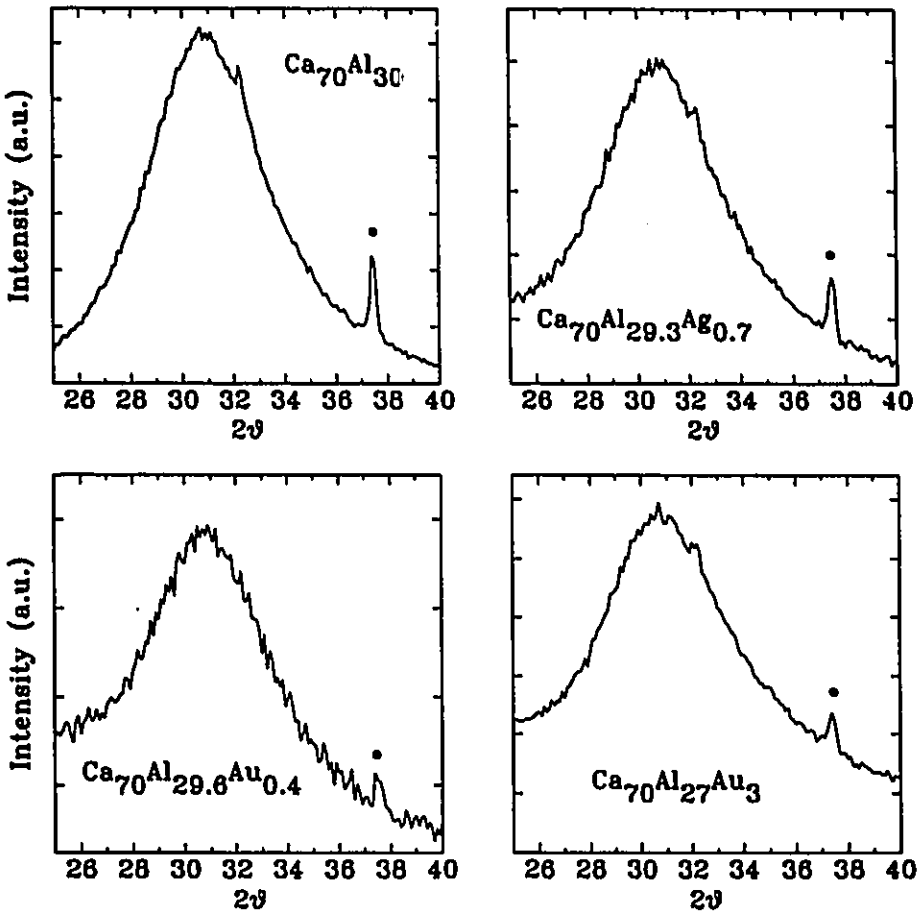

Figure 3.4: X-ray diffraction patterns of amorphous Ca-Al-(Ag,Au) alloys. The alloy chemical composition is indicated in the figure. The crystalline peak at $2\theta = 37.4^{o}$ (•) is due to Ca oxides on the surface of the ribbons.

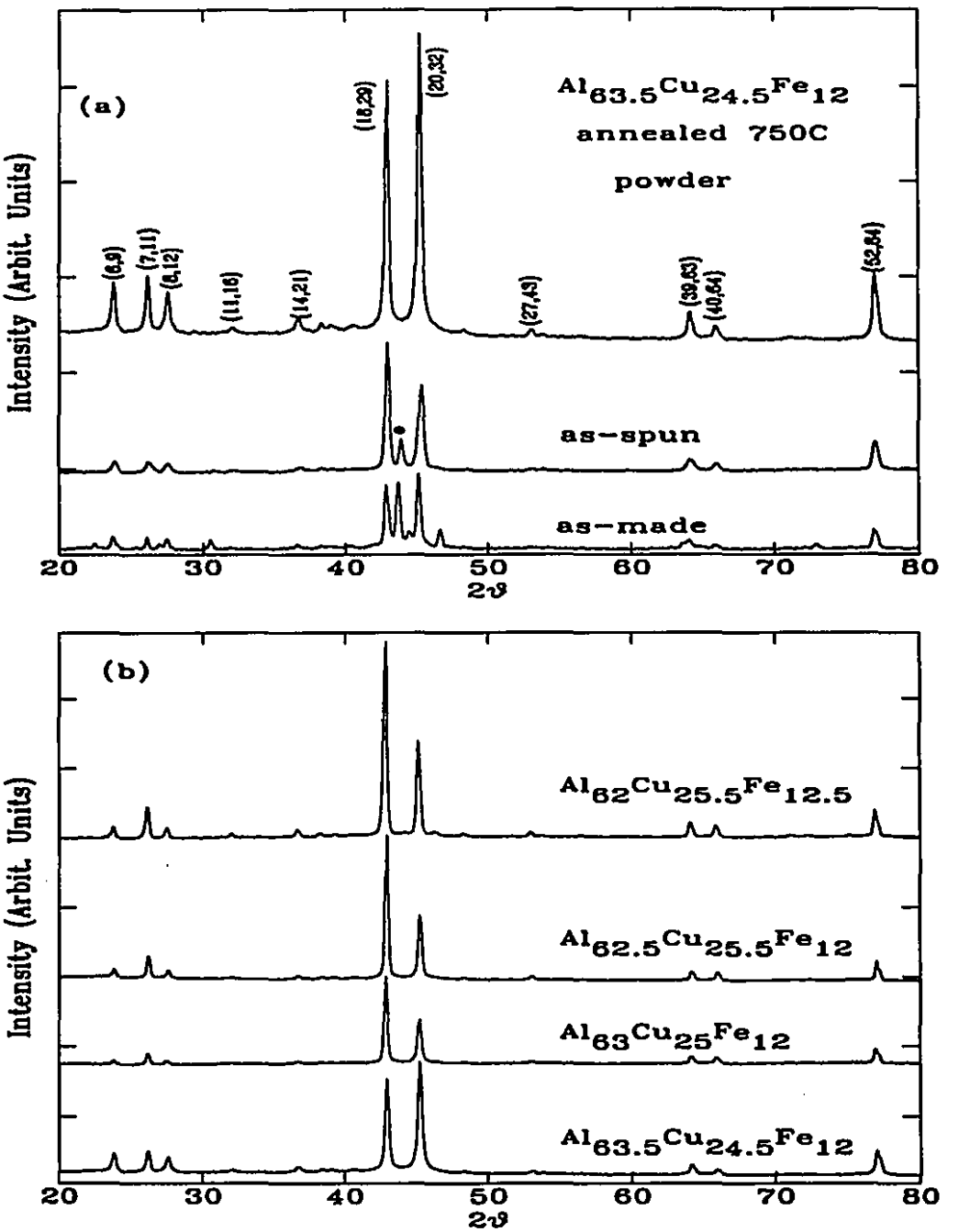

Figure 3.5: X-ray diffraction patterns of Al-Cu-Fe alloys.
a) Diffraction pattern of $Al_{63.5}Cu_{24.5}Fe_{12}$ before and after annealing ((•): AlFe-type crystalline phase).
b) Diffraction patterns of the four alloys selected in this thesis; the nominal composition is indicated in the figure. Note: all ribbons present texturing along the 5-fold axis corresponding to the (18,29) peak.

The diffraction peaks of the annealed ribbons, for the four different compositions, exactly index to an icosahedral structure. The indexing was done using the scheme proposed by Cahn *et al.* [80] as explained in Appendix B. It is important to note that for proper indexing of the x-ray diffraction patterns, which is based on the relative intensities of the peaks, it is preferable to perform powder diffraction scans as most of the ribbons prepared with low quenching rates, such as the ones considered here, present appreciable texturing (along the 5-fold axis for Al-Cu-Fe ribbons). However, the texturing has no effect on the measurements of the resistivity and magnetoresistance because of the high symmetry of the icosahedral structure. According to Bessière *et al.* [76] the perfect icosahedral phase exists only at a composition very close to $Al_{62.5}Cu_{25}Fe_{12.5}$ and small deviations from it lead to a relative broadening of the diffraction peaks.

3.2.2 Transmission and scanning electron microscopy

The quality of the quasicystalline structure was also checked by transmission electron microscopy (TEM) and scanning electron microscopy (SEM). The TEM analysis was performed using a Philips CM20 transmission electron microscope with an accelerating voltage of 200 keV. The samples were thinned to the desired thickness by electrochemical thinning. Diffraction patterns were taken in the standard bright field mode along the high symmetry axis; i.e. 5-fold, 3-fold and 2-fold axis, on several regions of the samples. Equally good quality diffraction patterns were observed for the four different alloy compositions (Figure 3.6). It was also possible by using the high resolution capability of the microscope to obtain a clear picture of the high degree of topological order of the icosahedral phase over relatively large areas, see Figure 3.7. The SEM was done on a JEOL scanning electron microscope. The accelerating voltage was 20 keV. The samples were glued to an Al sample holder using silver paste. Relatively large single "quasicrystals" are observed embedded in a fine single quasicrystals matrix (Figure 3.8.a). The average size of the crystals is reduced when the composition approaches the composition where the ideal icosahedral phase has been

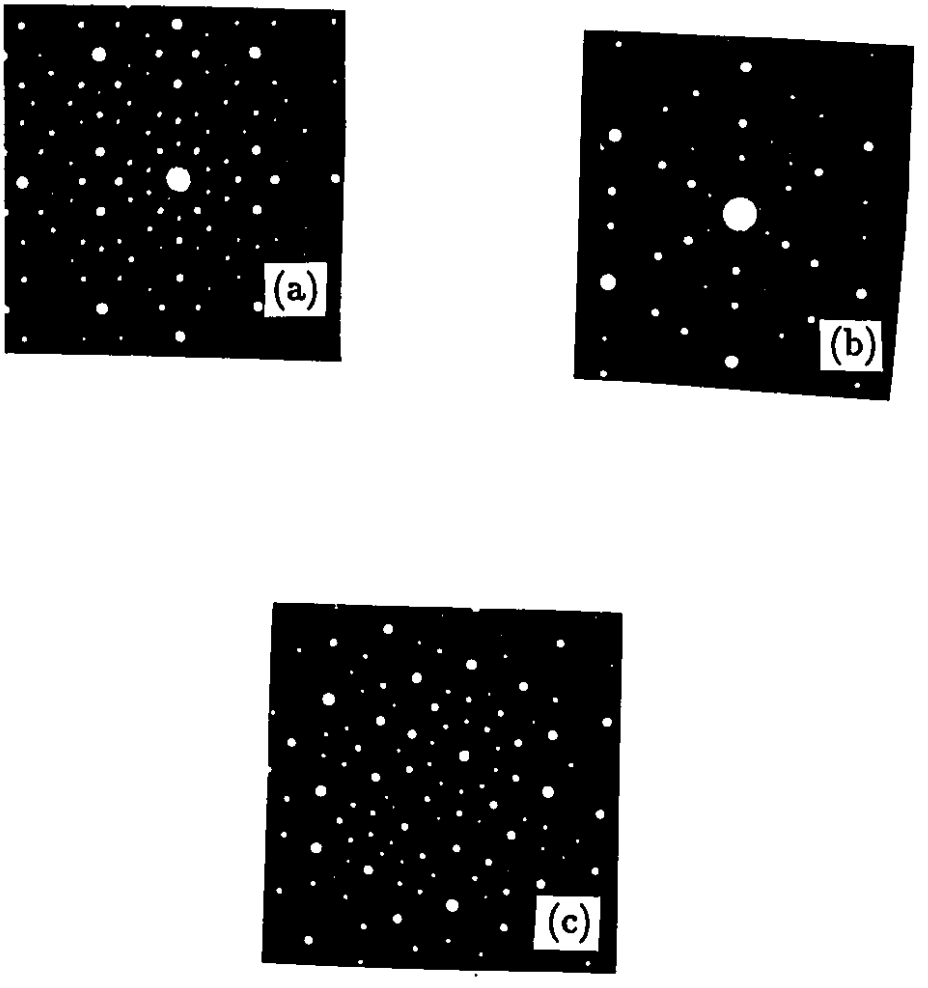

Figure 3.6: Electron diffraction patterns of icosahedral $Al_{63.5}Cu_{24.5}Fe_{12}$ alloy along (a) 2-fold, (b) 3-fold, (c) 5-fold axis, respectively.

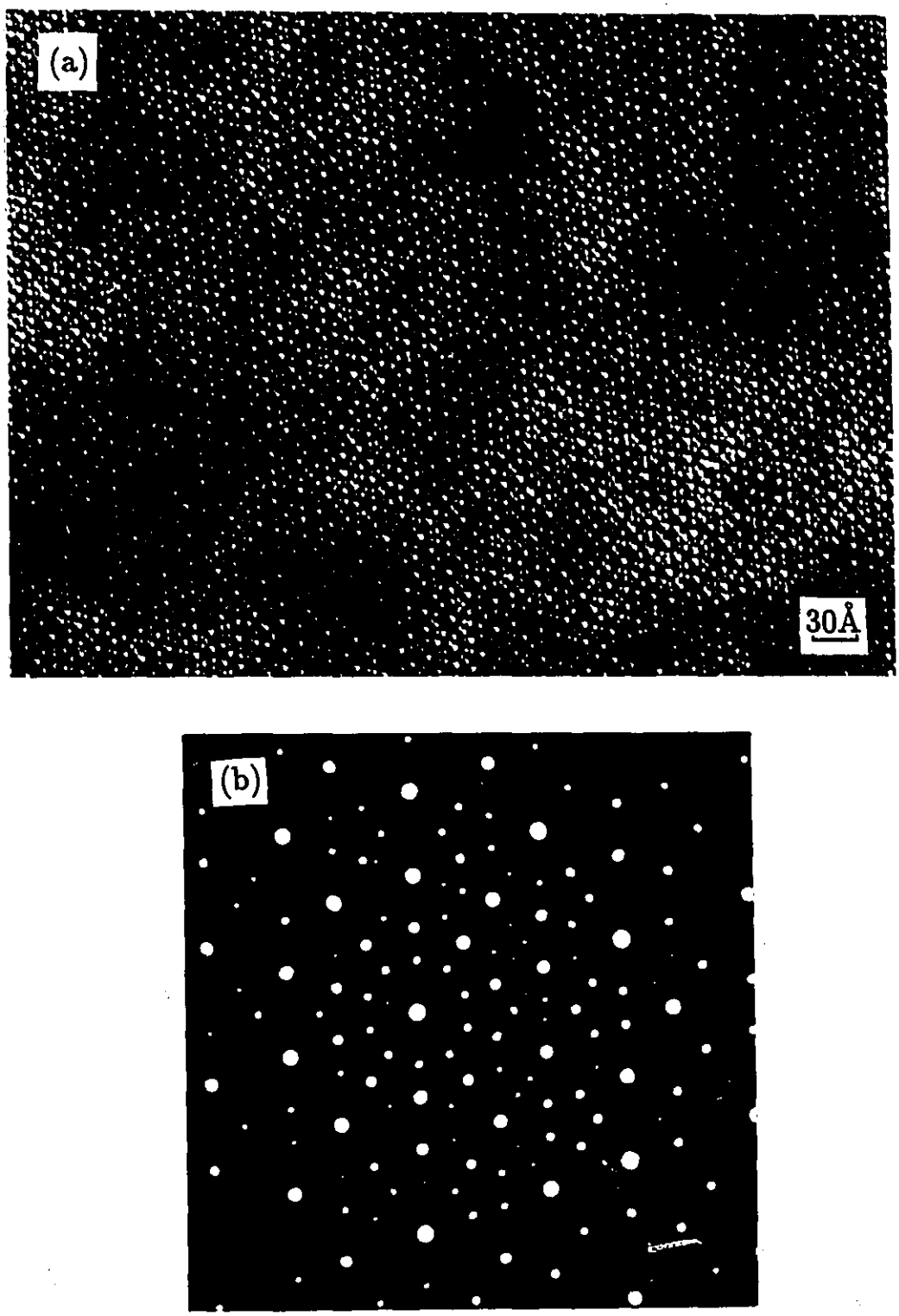

Figure 3.7: High-resolution electron transmission image of icosahedral $Al_{63.5}Cu_{24.5}Fe_{12.5}$ (a) along the fivefold axis. (b) The electron diffraction pattern used to obtain image (a).

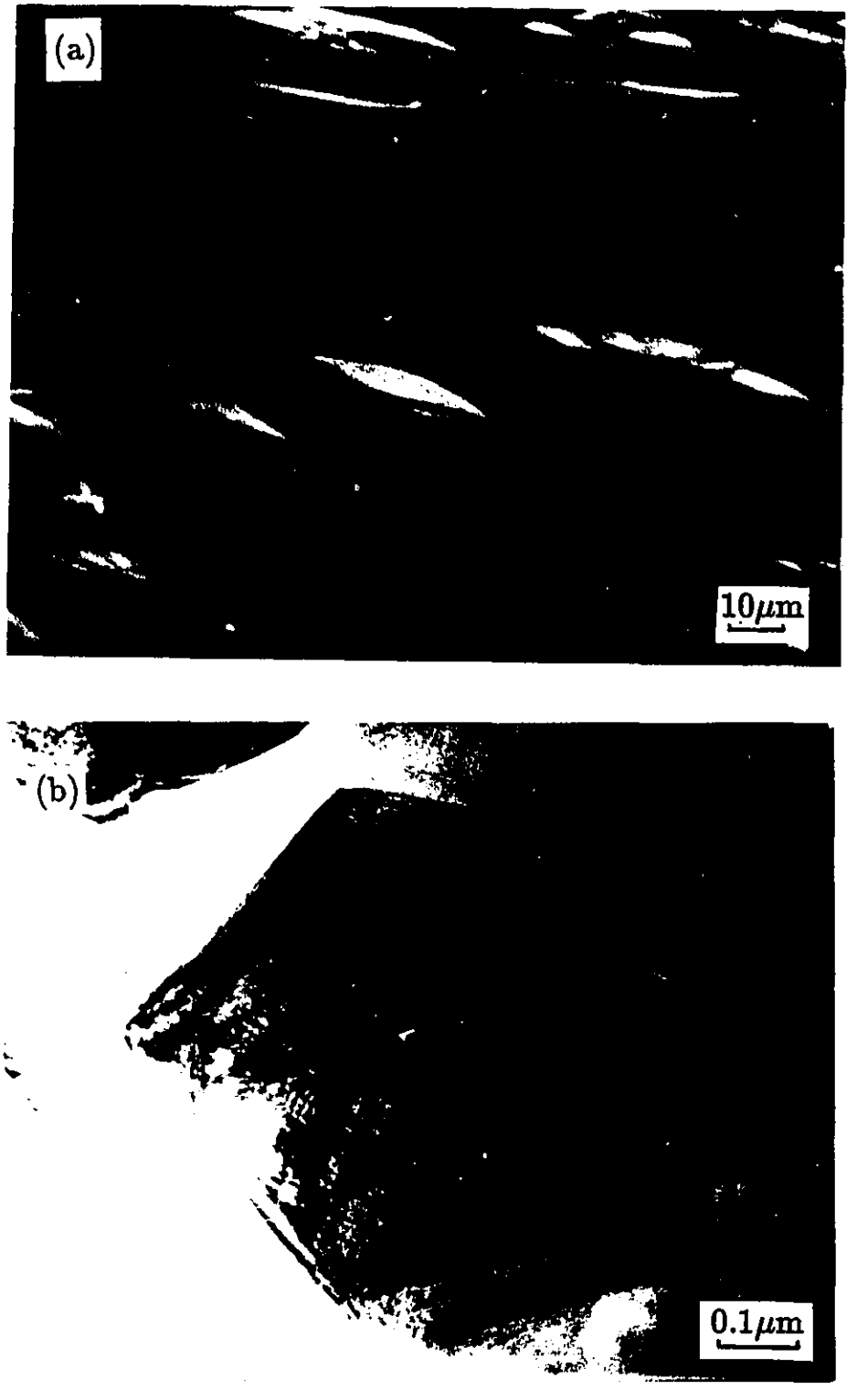

Figure 3.8: Scanning (a) and high-resolution electron transmission (b) micrographs of icosahedral $Al_{63.5}Cu_{24.5}Fe_{12}$ showing the symmetry and the large size of the quasicrystallites.

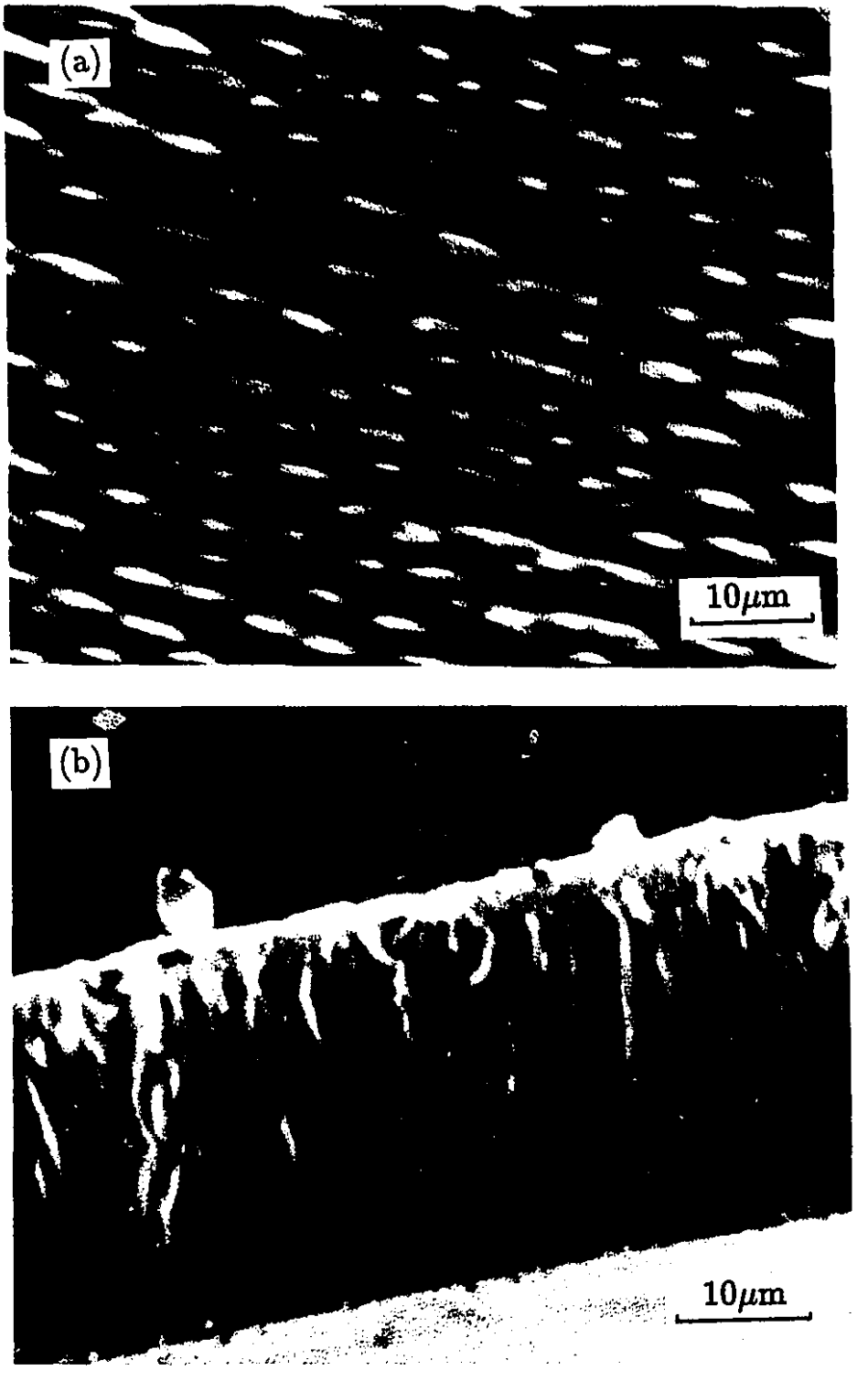

Figure 3.9: Scanning electron micrographs of icosahedral Al-Cu-Fe alloys.
(a) $Al_{62}Cu_{25.5}Fe_{12.5}$ showing a more homogeneous structure, (b) $Al_{63}Cu_{25}Fe_{12}$: cross sectional view showing texture along the 5-fold axis.

shown to exist [76] (3.9). On the other hand, cross section micrographs confirmed the presence of texturing in the alloys (see Figure 3.9.b).

3.2.3 Mass density and room temperature resistivity

Mass density measurements of the Ca-Al alloys were carried out using the Archimedes method with toluene as the working fluid. In order to reduce surface tension effects, a thin fiber glass wire was used to suspend the sample in the liquid. The weight in air W_{air} and in toluene W_{tol} was measured with a mechanical balance (Mettler H20T) to an accuracy of 10^{-3} gram. The mass density is then simply given by:

$$d_s = \frac{W_{air}}{W_{air} - W_{tol}}(d_{tol} - d_{air}) + d_{air}, \tag{3.1}$$

where $d_{tol} = 0.8669$ g/cm^3 is the mass density of toluene at room temperature and d_{air} the mass density of air ($\sim 10^{-3}$ g/cm^3 at 293K and 100 kPa). However because of the very low density of Ca-Al alloys it was difficult to accommodate more than $\sim$ 30 mg of material in the buoyancy balance which resulted in large error bars in d_s (about 10% or more). To overcome this problem, small buttons of the crystalline alloys were used instead and the accuracy was then 1% or better. The mass density of the amorphous samples is then obtained by subtracting 2% of the measured value to account for the volume difference [81]. In this way the error on the final values is estimated to be only about 3% or less. Within the error bars the mass density is a linear function of the Ag and Au concentration as shown in Figure 3.10 (see also Table 3.2). The present mass density value for $Ca_{70}Al_{30}$ is in good agreement with our previous results [18, 30] and with that reported by Mizutani and coworkers [31, 32].

In the case of Al-Cu-Fe samples it was not possible to measure their mass densities because of the large amounts of material required for a precise determination and we quote here the value reported by other authors [42].

The room temperature resistivity was measured by a four terminal technique using an LR400 resistance bridge (see subsection 3.3.4). For Ca-Al alloys, long ribbons (0.3

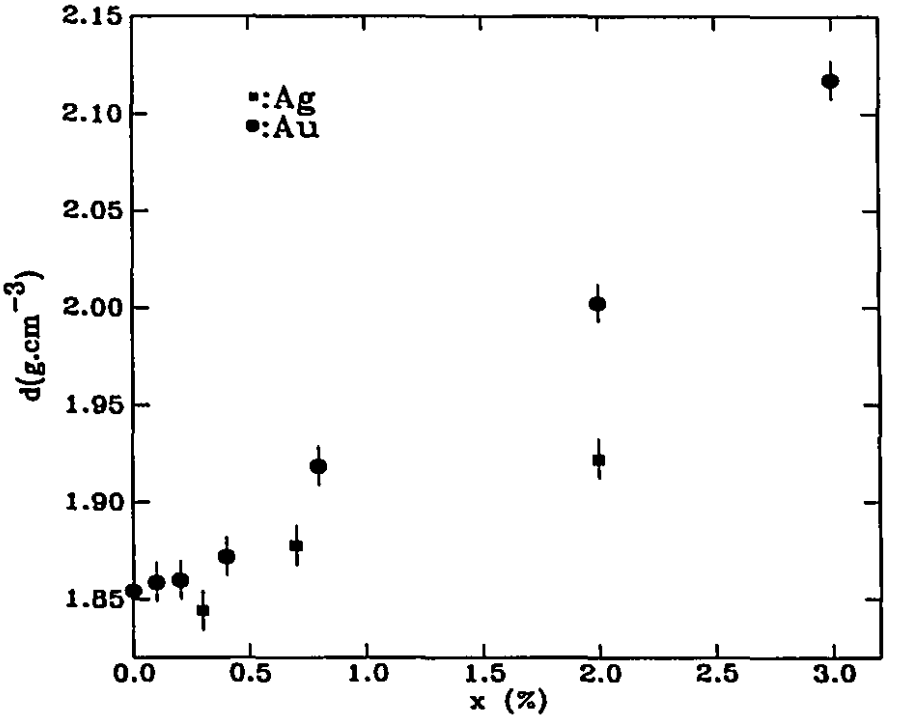

Figure 3.10: Mass density of amorphous Ca-Al-(Ag,Au) alloys.

m) were used and the cross sectional area needed for converting the resistance to resistivity was determined from measured mass densities. Then the resistivity is simply given by:

$$\rho = \frac{Rm}{dL^2} = \frac{R.A}{L}. \tag{3.2}$$

R being the resistance, L the ribbon length and d the mass density. The resistivity of Al-Cu-Fe specimens was estimated from the measured length, width and thickness of the samples. However in this way, large error bars especially for Al-Cu-Fe samples are encountered because of the uncertainty in measuring the exact dimensions of relatively short ribbons (about 5 - 20 mm). But in general the extracted values agree well with the reported results of other workers [43, 44, 52, 82]. The room temperature resistivities of all samples studied in this work is listed in Table 3.2.

Alloy	d (g/cm^3)	$\rho(\mu\Omega.\text{cm})$
$Ca_{70}Al_{30}$	1.85 ± 0.04	310 ± 16
$Ca_{70}Al_{29.7}Ag_{0.3}$	1.84 ± 0.04	264 ± 13
$Ca_{70}Al_{29.3}Ag_{0.7}$	1.84 ± 0.04	270 ± 13
$Ca_{70}Al_{28}Ag_2$	1.92 ± 0.04	245 ± 12
$Ca_{70}Al_{29.9}Au_{0.1}$	1.86 ± 0.04	297 ± 15
$Ca_{70}Al_{29.8}Au_{0.2}$	1.86 ± 0.04	280 ± 14
$Ca_{70}Al_{29.6}Au_{0.4}$	1.87 ± 0.04	280 ± 14
$Ca_{70}Al_{29.2}Au_{0.8}$	1.92 ± 0.04	290 ± 15
$Ca_{70}Al_{28}Au_2$	2.00 ± 0.04	220 ± 14
$Ca_{70}Al_{27}Au_3$	2.12 ± 0.04	210 ± 14
$Al_{63.5}Cu_{24.5}Fe_{12}$	4.5†	4620 ± 460
$Al_{63}Cu_{25}Fe_{12}$	4.5†	5330 ± 530
$Al_{62.5}Cu_{25.5}Fe_{12}$	4.5†	6700 ± 670
$Al_{62}Cu_{25.5}Fe_{12.5}$	4.5†	9730 ± 970

Table 3.2: Mass density and room temperature resistivity of amorphous Ca-Al-(Ag,Au) and icosahedral Al-Cu-Fe samples. †: From reference [42].

3.3 Low temperature resistivity and magnetoresistance measurements

Low temperature resistivity and magnetoresistance measurements were carried out in a standard liquid He cryostat between room temperature and 1.5 K and, in a dilution refrigerator down to 150 mK. All magnetoresistance measurements were done in the longitudinal field configuration, i.e. $\vec{B}//\vec{J}//\vec{E}$.[1]

[1]On one occasion, measurements in the perpendicular configuration, $\vec{B} \perp \vec{J}$, were performed to confirm that texturing has no effect on the magnetoresistance of icosahedral Al-Cu-Fe alloys.

3.3.1 Liquid helium cryostat

The temperature dependence of the resistivity and the magnetoresistance up to 8.8T and down to 1.5K was measured in the bore (2.54cm) of a Nb-Ti superconducting solenoid (from American Magnetics, Inc; Model # 2468) installed in a stainless-steel dewar system (Hoffmann, Airco). The setup is shown in Figure 3.11. The solenoid is immersed in liquid He and a set of Allen-Bradley 1/8 watt resistors placed below and above it served as level detectors. The He bath is thermally shielded by liquid nitrogen in the outer dewar. The sample holder is placed inside a thin-wall stainless-steel dewar made in the laboratory [83]. Measurements between 1.5 and 4.2K were performed by first immersing the sample in the liquid and lowering the temperature of the bath by reducing the pressure in the sample chamber. A system of valves, gauges and a heater allows temperature control to within 1% or better. Above 4.2K the temperature is stabilized by thermally linking the sample space to the magnet He bath and heating the sample holder by the non inductively wound heater. Typically, the pressure in the sample chamber and the interspace were 0.1 mbar and 10^{-4} mbar, respectively. The heater current was controlled by an analog feedback mechanism.

The magnet was energized by a HP Harrison 6260A DC power supply through two diode protection stacks. The role of the diode stacks is to limit the rate of current change through the solenoid below its maximum rated value (I_{max} = 78.4 Amps) and also to protect the source from overload voltages from the solenoid. The current through the solenoid and hence the field strength was varied manually by a discrete Keithley K2601 nanovoot source and was monitored as a voltage drop across a 0.5 mΩ resistor. The voltage was read by a 175A Keithley digital multimeter. According to the manufacturer's specifications the superconducting solenoid's field factor ratio is B/I = 0.11486 T/Amps and the field is uniform to within 0.2% over the sample. To further minimize liquid He loss during the field sweeps (by Joule heating and thermal dissipation), the vapor cooled leads carrying the magnet's current were made of two successive assemblies of 20 and 10 copper wires of 0.3 mm diameter each [84].

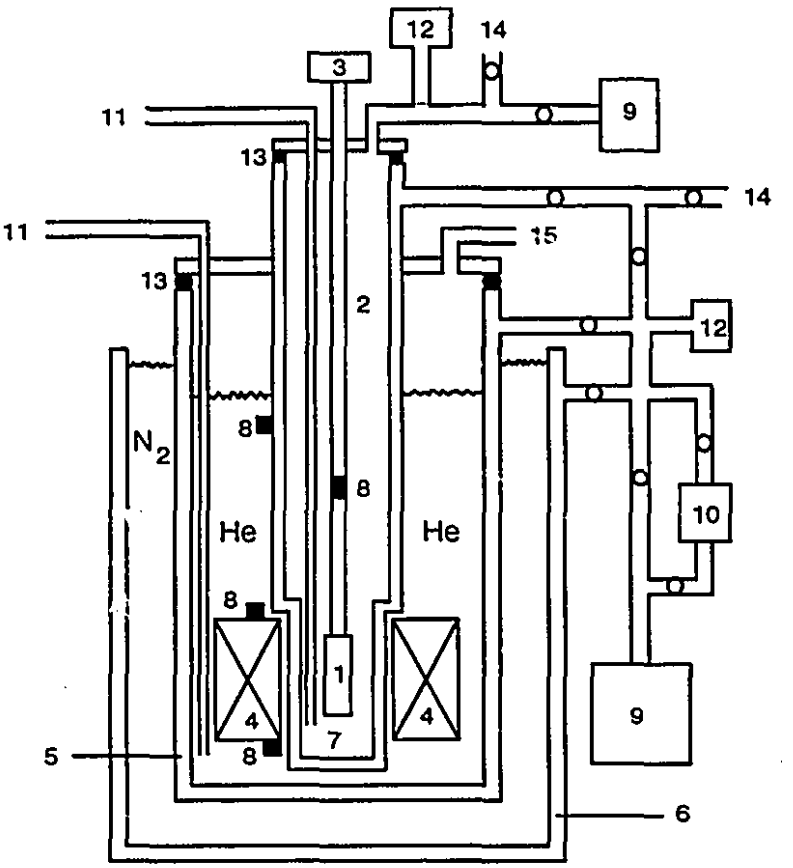

Figure 3.11: Schematic diagram of magnetoresistance cryostat. 1) Cu sample holder, 2) Stainless steel tubes, 3) Terminal lead box, 4) Superconducting magnet solenoid, 5) Liquid Helium dewar, 6) Liquid nitrogen dewar, 7) Sample holder dewar, 8) Liquid Helium level detectors, 9) Rotary vacuum pump, 10) Diffusion pump 11) Liquid Helium transfer tube, 12) Vacuum gauges, 13) O-ring, 14) He gas inlet, 15) He gas outlet.

3.3.2 Sample holder

Figure 3.12 shows the probe used for the measurements of the magnetic field and temperature dependence of the resistivity in the range 0 to 8.8T and 1.5 to 300 K respectively. To facilitate their installation the samples were first mounted on individual copper plates and electrically isolated from them with thin mylar foils. The plates were then glued (one on each side) with GE varnish to the copper block. The whole was suspended inside the sample chamber at the center of the magnet with four thin-wall stainless steel tubes that contains the thin ($\approx$ 70 μm diameter) copper leads for the samples, thermometer, heater and He level detector. We should note that the sample current and voltage leads were kept away from each other to avoid any interference between them. The Ca-Al-(Ag,Au) and Al-Cu-Fe samples are very brittle and vacuum grease was used to attach them to the copper plates, but only at the ends. In this way, sufficient thermal contact was ensured, without subjecting the sample to too much strain due to differential thermal contraction. Thin gold wires ($\sim$ 70 μm diameter) were used to make current and voltage contacts and, were attached to the sample with silver paste.

The temperature of the sample was measured with a calibrated carbon-glass resistor (CGR) from Lakeshore Cryotronics Inc. with an accuracy varying from $\pm$0.1% at 1.5 K to $\pm$0.05% at 300 K. Its conductance was monitored with a PCB 4-terminal a.c. conductance bridge (from SHE Inc, now Biomagnetic Technologies Inc.). The low-power PCB bridge can measure conductances from 200 $\mu\Omega^{-1}$ to 200 Ω^{-1} to an accuracy of $\pm$0.05%. Hence the only limit on the accuracy of the measured temperature is the small magnetoresistance of the carbon-glass resistor which causes a misreading of less than 2.3% at 4.2K and 8T. The differential analog voltage output feature on the PCB was used as a driver to control the sample heater current as mentioned earlier.

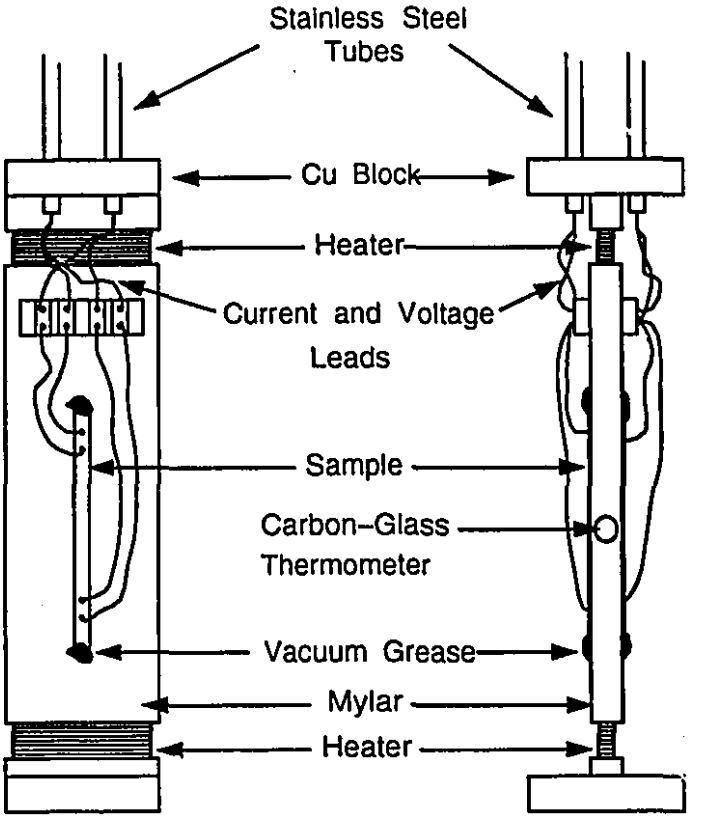

Figure 3.12: The sample holder used for magnetoresistance and resistivity measurements

3.3.3 Dilution refrigerator

Measurements of the resistivity of Al-Cu-Fe and Mg-Cu samples down to 150 mK were performed in a SHE mini-dilution refrigerator. A schematic of the apparatus is shown in Figure 3.13. The Al-Cu-Fe were mounted directly on a copper block in the same way as above. The copper block was then tightly screwed to the bottom of the stage. To increase thermal contact a thin layer of vacuum grease mixed with copper powder was used. The working principle of the dilution refrigerator has been explained in detail by several authors (see for example the recent book by Betts [85]). The cooled stage is contained in an evacuated stainless steel jacket surrounded by a ^{4}He bath. At the top of this stage a chamber that draws ^{4}He from the bath is kept at

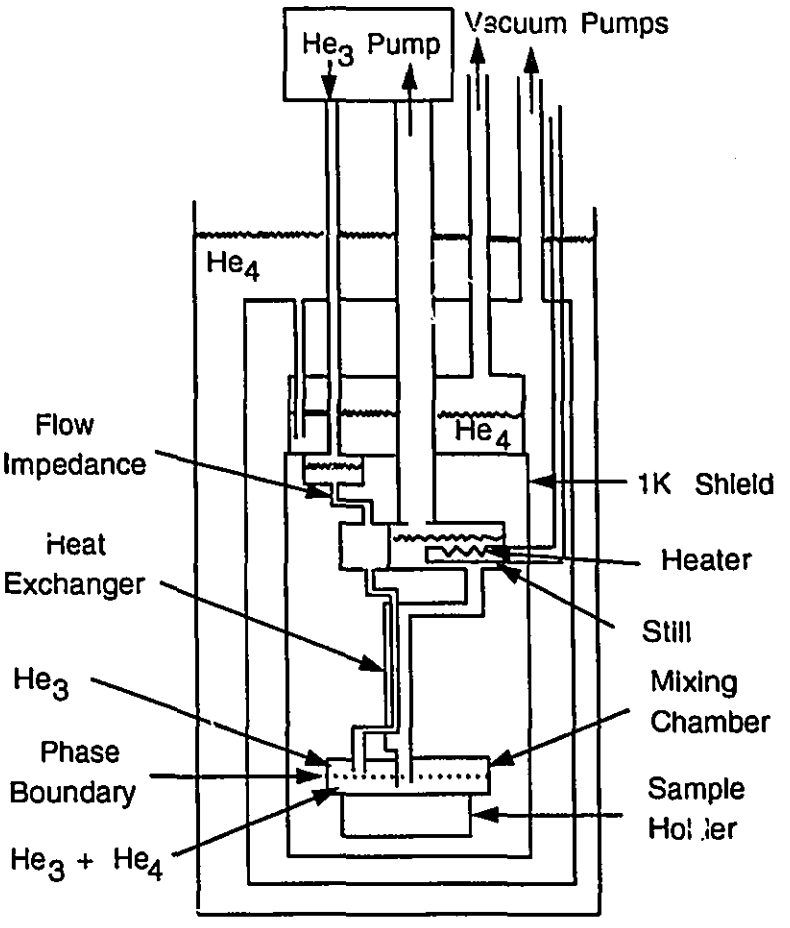

Figure 3.13: Schematic of the dilution refrigerator cold stage

1K by pumping on the liquid. Sample cooling is produced in the mixing chamber by the continuous dilution of ^{3}He atoms in the ^{4}He rich mixture. When measuring the resistance great care was taken to avoid self-heating effects of the sample. Self-heating occurs when the energy dissipated by the sensing current can not be conducted at the same rate into the sample holder (mixing chamber) due to the poor thermal conductivity at low temperatures. Thus, the sensing current was reduced to about 1μA for the resistivity measurements in the dilution refrigerator resulting in a few tens of pW of power being dissipated by the sample and the contacts.

3.3.4 Resistance bridge and data acquisition

A low-power LR400 a.c. resistance bridge (from Linear Research, USA) was used to measure the resistance of the different samples considered in this thesis. Depending on the alloy, the sample resistance varied from 1 to 15Ω. The main features of the bridge are its high stability, sensitivity and wide range of applications. It can measure resistances from 20mΩ to 200$k\Omega$ to a precision of one part in 10^6. Furthermore the bridge has a variable excitation level which can be very useful for measurements at dilution refrigerator temperatures.

The resistance changes in our samples due to phenomena described in Chapter 2 are expected to range from 10^{-5} to 10^{-1}. Hence the LR400 bridge has enough sensitivity to extract the signal. A filter with a time constant of 3 seconds was used to reduce the noise level further.

For data acquisition, all voltages: PCB, LR400, and the voltage across the 0.5mΩ resistor (which is proportional to the magnetic field) were measured by Keithly Instruments, models 197A and 175 auto-ranging multimeters as shown in Figure 3.14. The multimeter readings were then fed into an IBM PC through an IEEE 488 interface. To reduce even more the noise, which decreases as the inverse of the number of readings $\sqrt{N}$, each data point is the average of four separate readings of the voltmeter. For further processing the data were transferred to a SUN computer system.

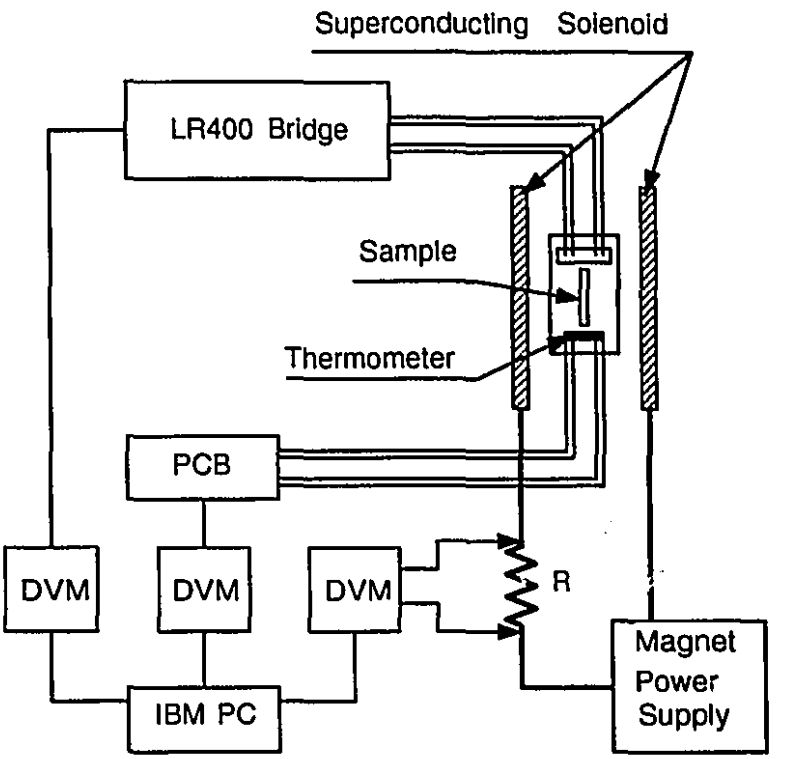

Figure 3.14: Schematic diagram of the experimental setup for magnetoresistance and resistance measurements and the data acquisition system

Chapter 4

Results and Discussion

In this Chapter we present and discuss our experimental measurements of the magnetic field and temperature dependences of the resistivity in ten different Ca-Al-(Au,Ag) metallic glasses and four Al-Cu-Fe icosahedral quasicrystals. In most cases, the measurements were done between 1.5 and 30 K in fields up to 8.8 T using the standard liquid He cryostat described in the previous Chapter. But measurements of the temperature dependence of the resistivity of two Al-Cu-Fe samples were made down to 150 mK in the dilution refrigerator and are also presented here.

The chapter is made of two main sections. The first one (section 4.1) contains all the results and discussion of the Ca-Al-(Ag,Au) amorphous alloys. For clarity the section is divided into several subsections. In 4.1.1, the magnetoresistance data are presented and described qualitatively within the framework of quantum corrections to the conductivity. Then a quantitative comparison between the theory and experiment is presented in 4.1.2. Discussions of the dephasing rate τ_ϕ, the spin-orbit scattering rate τ_{so}, and the influence of spin-orbit scattering on the enhanced electron-electron interaction follow in 4.1.3-5, respectively. In subsection 4.1.6 we discuss in detail the temperature dependence of the resistivity between 1.5 and 4.3 K. A summary is given at the end of the section in 4.1.7. Section 4.2 is dedicated to icosahedral Al-Cu-Fe samples and is structured in very much the same way as section 4.1. The main features of the Al-Cu-Fe icosahedral alloys magnetoresistance are commented on in 4.2.1. The

analysis of the experimental data and the discussion of the dephasing rate τ_ϕ and the interaction constant $\tilde{F}_\sigma$ follow in subsections 4.2.2, 4.2.3 and 4.2.4, respectively. The temperature dependence of the resistivity down to 150 mK is presented in 4.2.5. Finally a summary of the discussion is given in 4.2.6.

4.1 Amorphous Ca-Al-(Ag,Au)

4.1.1 Magnetoresistance

In this subsection we present our experimental results of the magnetoresistance of $Ca_{70}Al_{30-y}X_y$; X = Ag, Au and y = 0, 0.3, 0.7, 2 for Ag and, y = 0.1, 0.2, 0.4, 0.8, 2, 3 for Au respectively. These are shown in Figures 4.1-10 for different temperatures ranging between 1.5 and 25 K. Note that measurements at 30 K were also carried out for $Ca_{70}Al_{28}Au_2$ and $Ca_{70}Al_{27}Au3$. The error in the data is estimated to be much less than the size of the points ($\approx 4\times10^{-6}$) and is mainly due to temperature fluctuations.

The magnetoresistance is much larger than what would be expected form the orbital magnetoresistance resulting from the Lorentz force on the conduction electrons (Eq. 2.1). In all samples it is positive at low fields reflecting the presence of finite spin-orbit scattering. At high fields however it is either positive or negative depending on the concentration of Ag or Au. As the temperature increases the overall magnitude of the magnetoresistance is reduced, due to increasing inelastic scattering, which, as explained in Chapter 2 destroys the phase coherence of the electron wavefunction. Moreover in samples with small Ag or Au content, the region of positive magnetoresistance at low fields disappears completely at high temperatures. This is because the effect of the spin-orbit scattering becomes overwhelmed by the dephasing due to the inelastic scattering by phonons at high temperatures. For samples with large Au concentration (i.e. 2 and 3 at.%), however, the magnetoresistance remains positive over the full range of field and temperature because of the more intense spin-orbit scattering in these alloys. We also note that the data of the $Ca_{70}Al_{30}$ alloy are identical with earlier results [18, 19, 30]. However our data are in conflict with previous

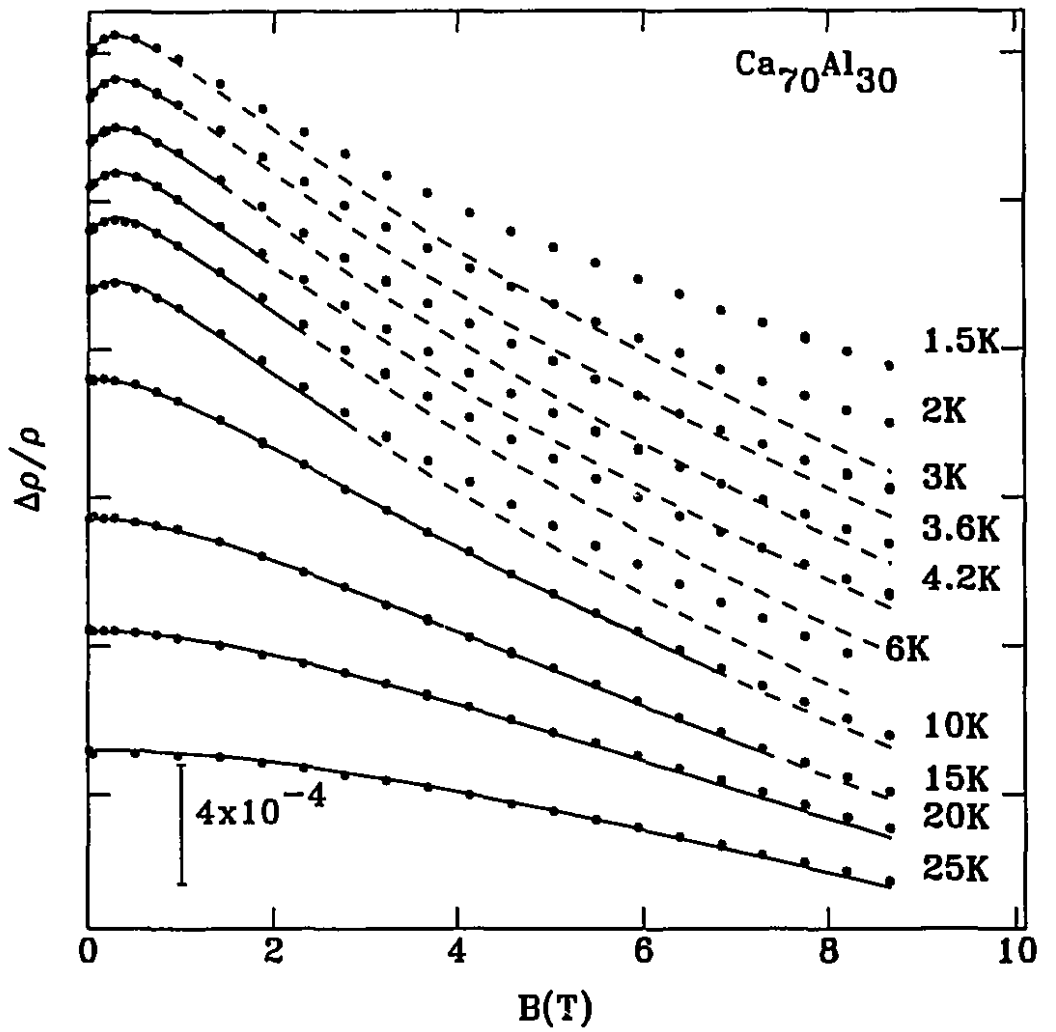

Figure 4.1: Normalized magnetoresistance of $Ca_{70}Al_{30}$. The scale and temperatures are indicated in the figure. The points are the experimental data, the solid line the fitted magnetoresistance (Eq. 2.14) and the dashed line its extrapolation as described in the text.

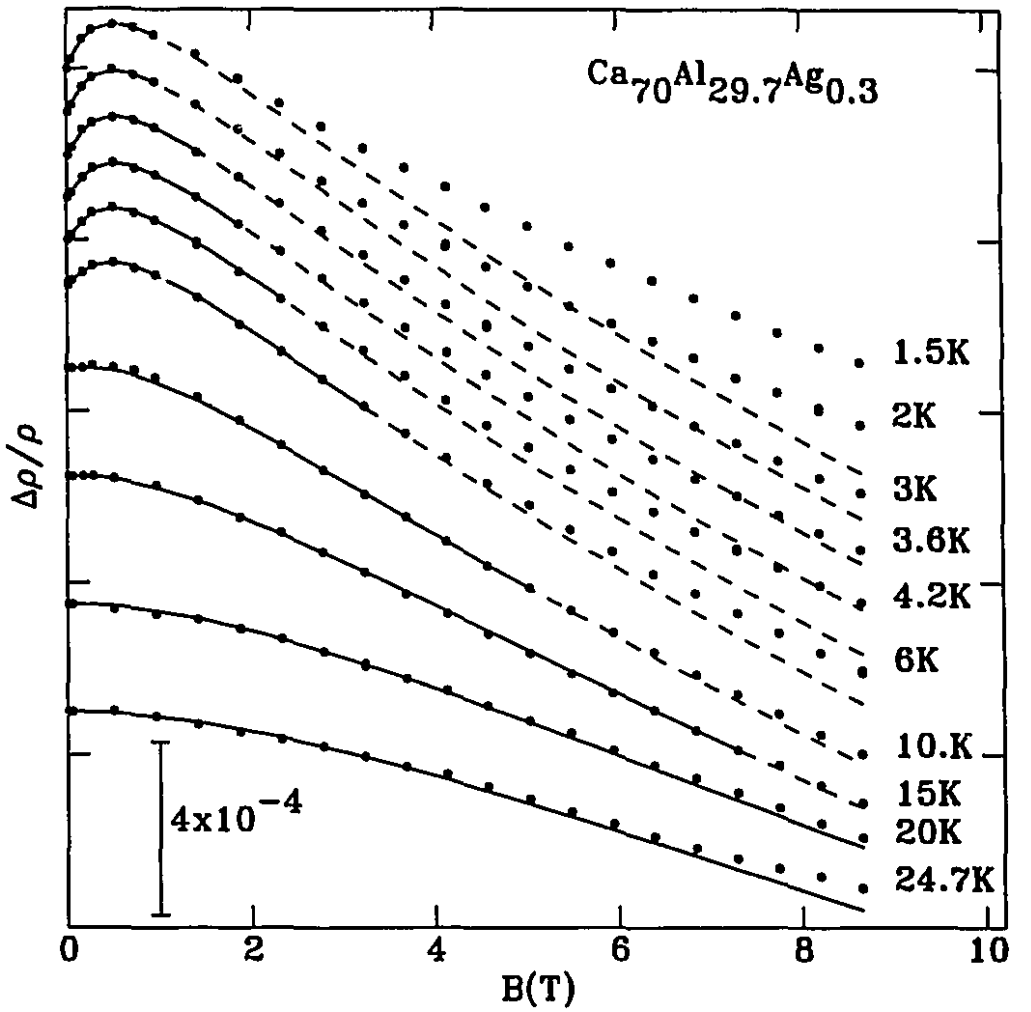

Figure 4.2: Normalized magnetoresistance of $Ca_{70}Al_{29.7}Ag_{0.3}$. The scale and temperatures are indicated in the figure. The points are the experimental data, the solid line the fitted magnetoresistance (Eq. 2.14) and the dashed line its extrapolation as described in the text.

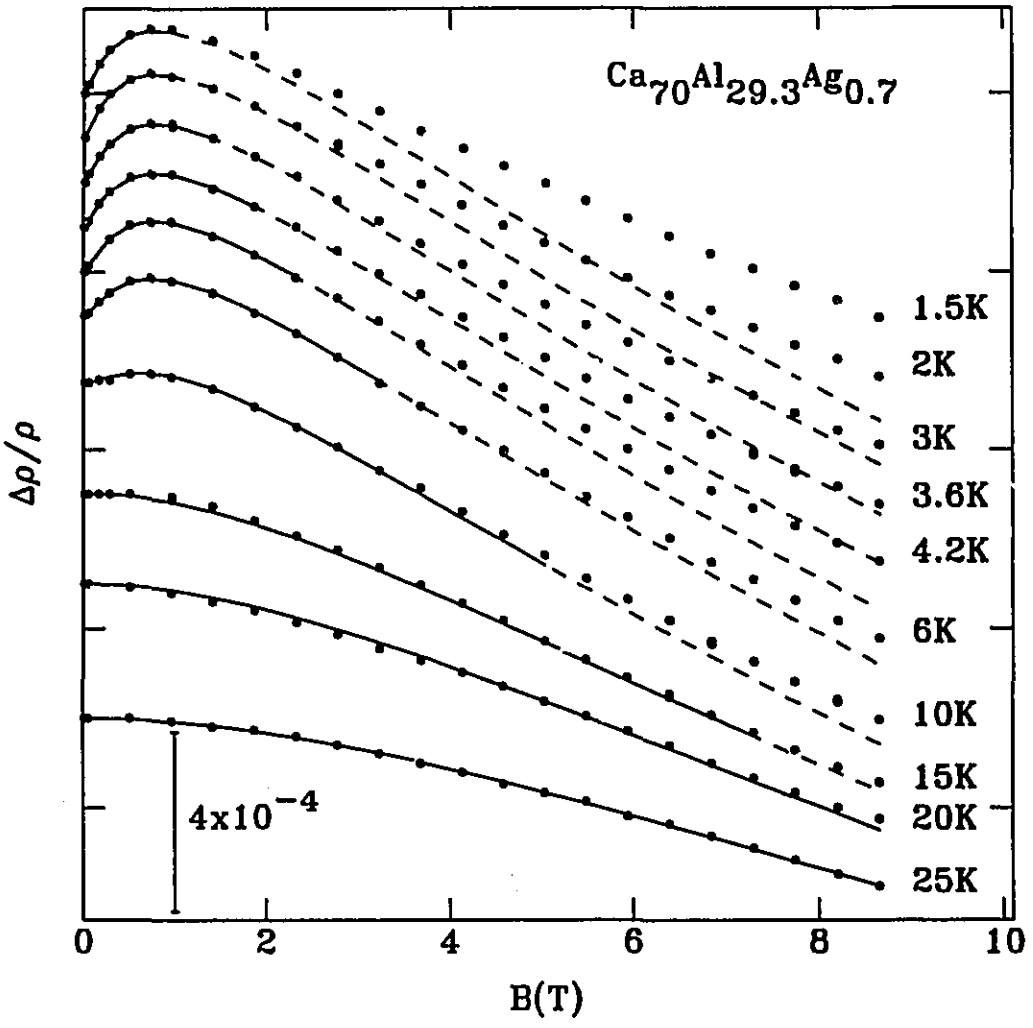

Figure 4.3: Normalized magnetoresistance of $Ca_{70}Al_{29.3}Ag_{0.7}$. The scale and temperatures are indicated in the figure. The points are the experimental data, the solid line the fitted magnetoresistance (Eq. 2.14) and the dashed line its extrapolation as described in the text.

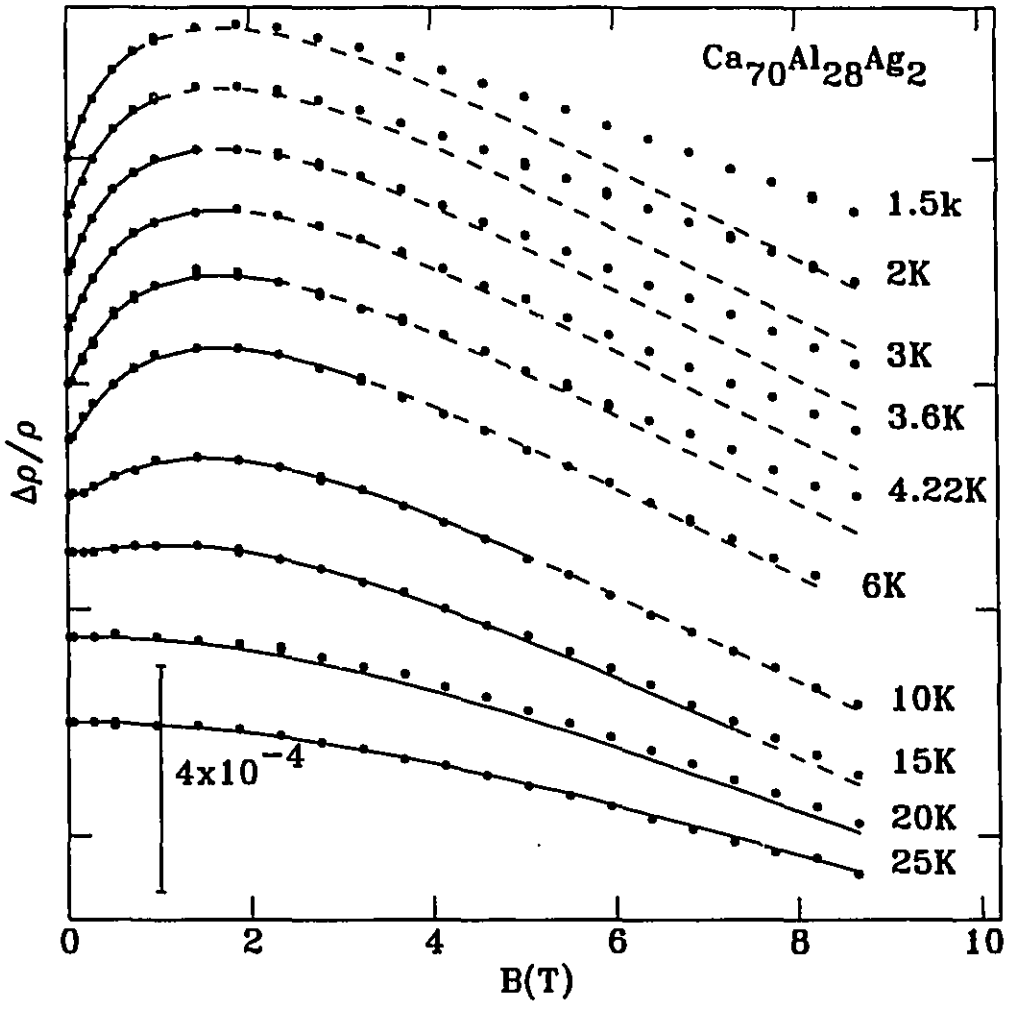

Figure 4.4: Normalized magnetoresistance of $Ca_{70}Al_{28}Ag_2$. The scale and temperatures are indicated in the figure. The points are the experimental data, the solid line the fitted magnetoresistance (Eq. 2.14) and the dashed line its extrapolation as described in the text.

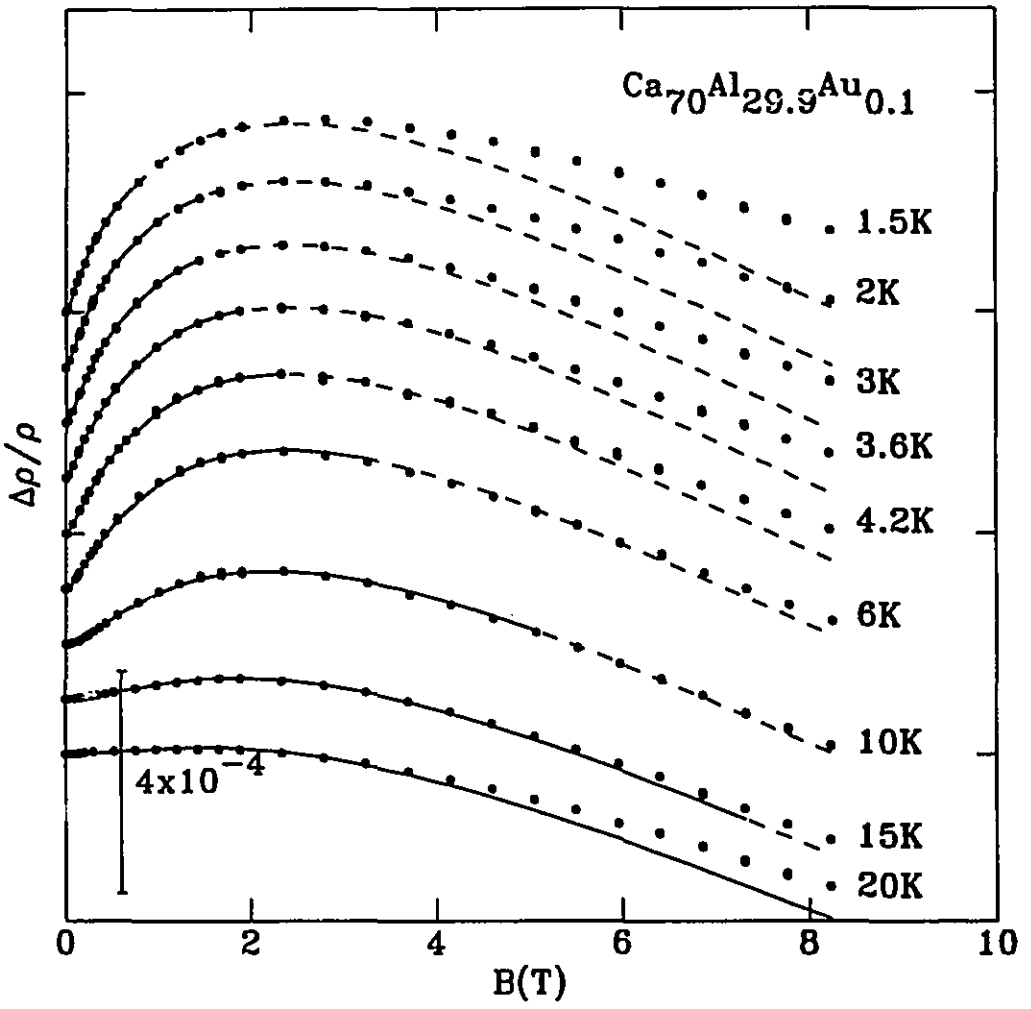

Figure 4.5: Normalized magnetoresistance of $Ca_{70}Al_{29.9}Au_{0.1}$. The scale and temperatures are indicated in the figure. The points are the experimental data, the solid line the fitted magnetoresistance (Eq. 2.14) and the dashed line its extrapolation as described in the text.

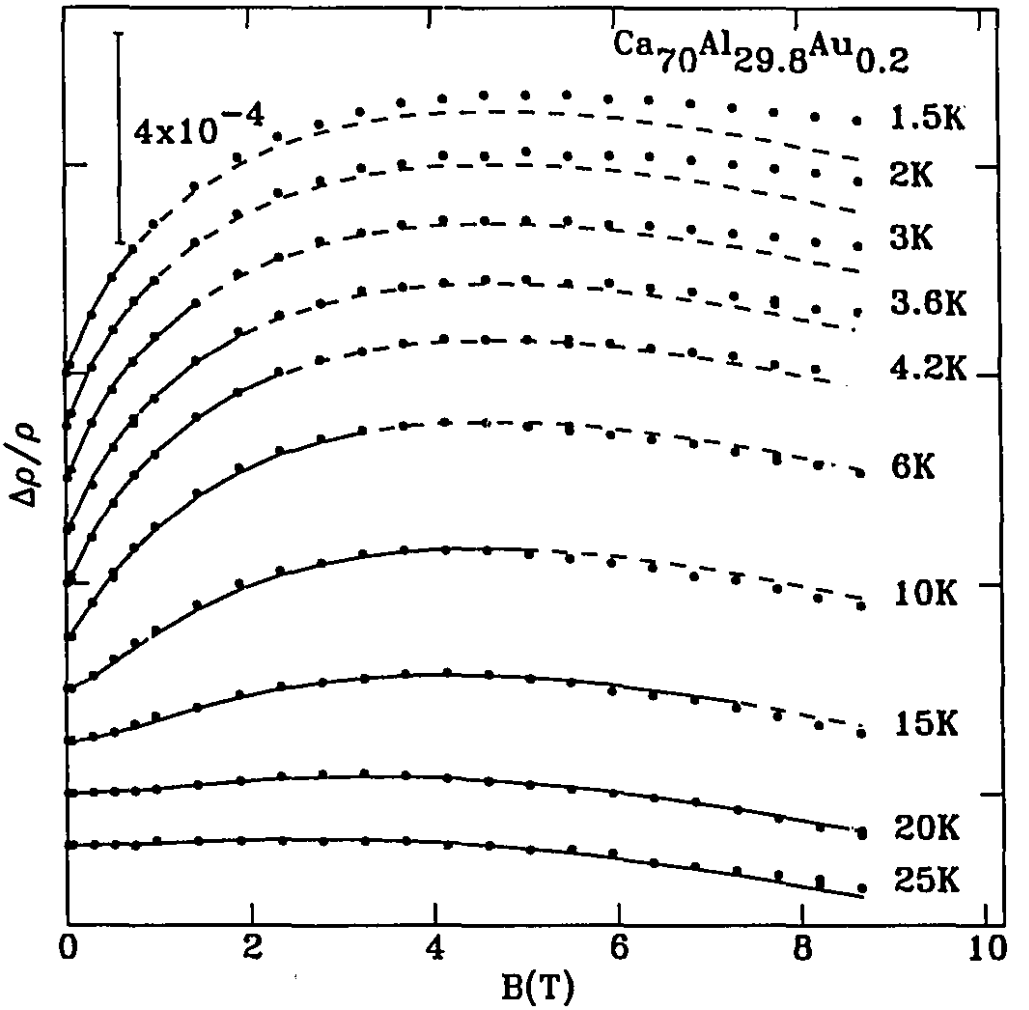

Figure 4.6: Normalized magnetoresistance of $Ca_{70}Al_{29.8}Au_{0.2}$. The scale and temperatures are indicated in the figure. The points are the experimental data, the solid line the fitted magnetoresistance (Eq. 2.14) and the dashed line its extrapolation as described in the text.

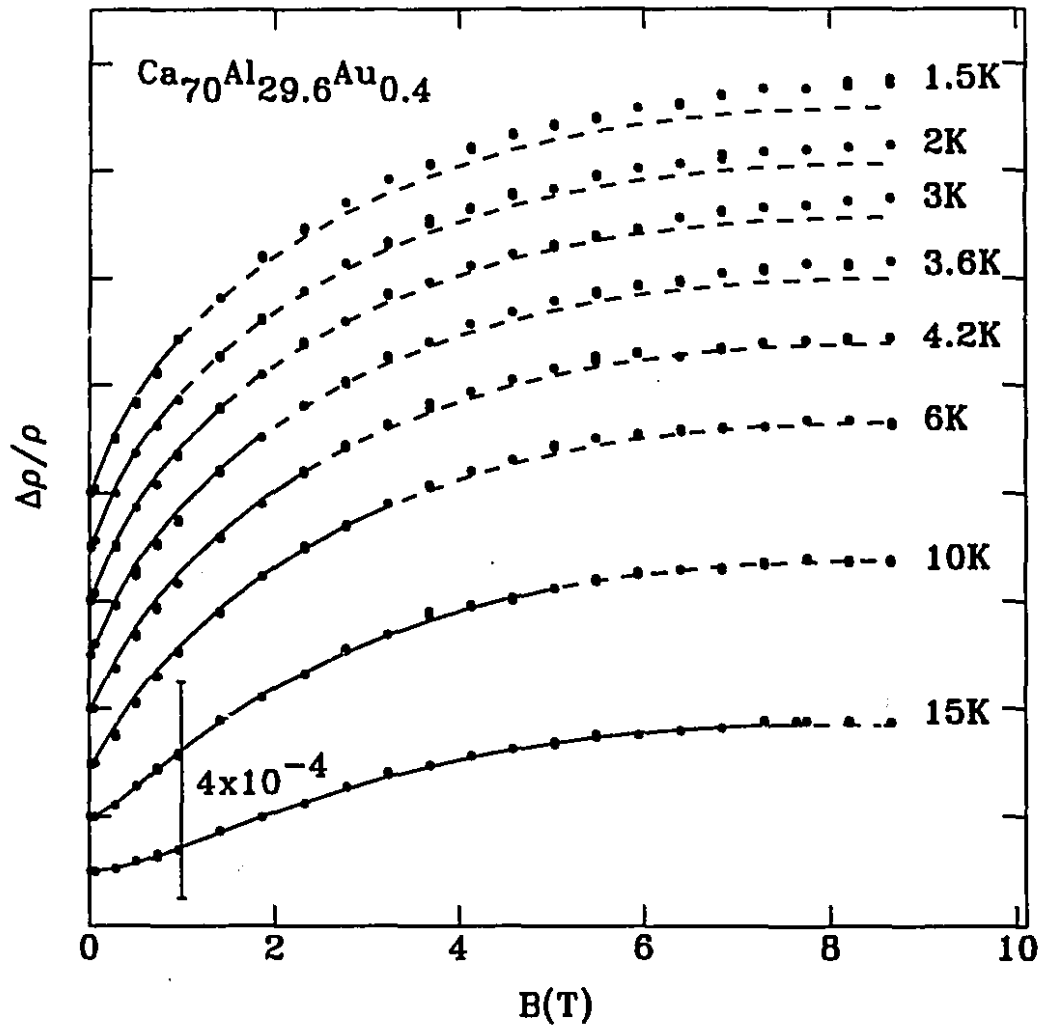

Figure 4.7: Normalized magnetoresistance of $Ca_{70}Al_{29.6}Au_{0.4}$. The scale and temperatures are indicated in the figure. The points are the experimental data, the solid line the fitted magnetoresistance (Eq. 2.14) and the dashed line its extrapolation as described in the text.

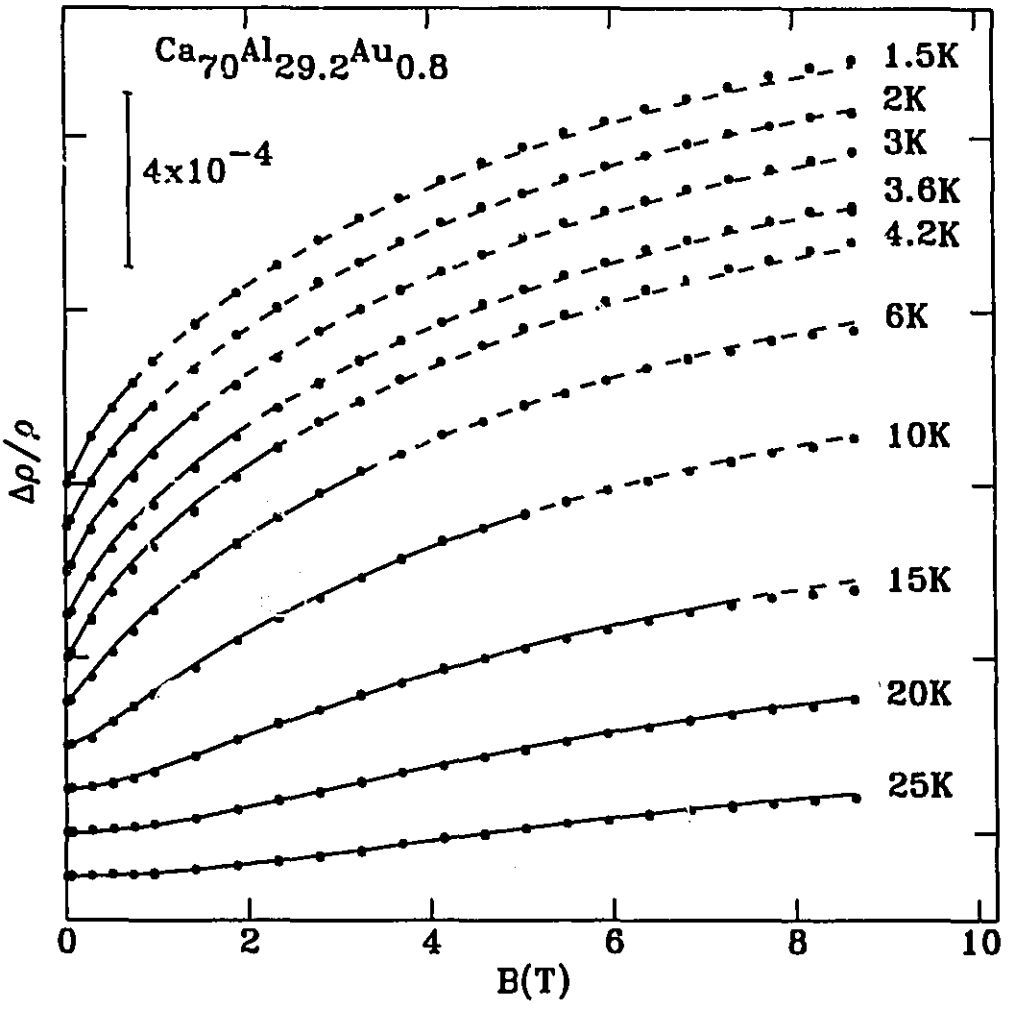

Figure 4.8: Normalized magnetoresistance of $Ca_{70}Al_{29.2}Au_{0.8}$. The scale and temperatures are indicated in the figure. The points are the experimental data, the solid line the fitted magnetoresistance (Eq. 2.14) and the dashed line its extrapolation as described in the text.

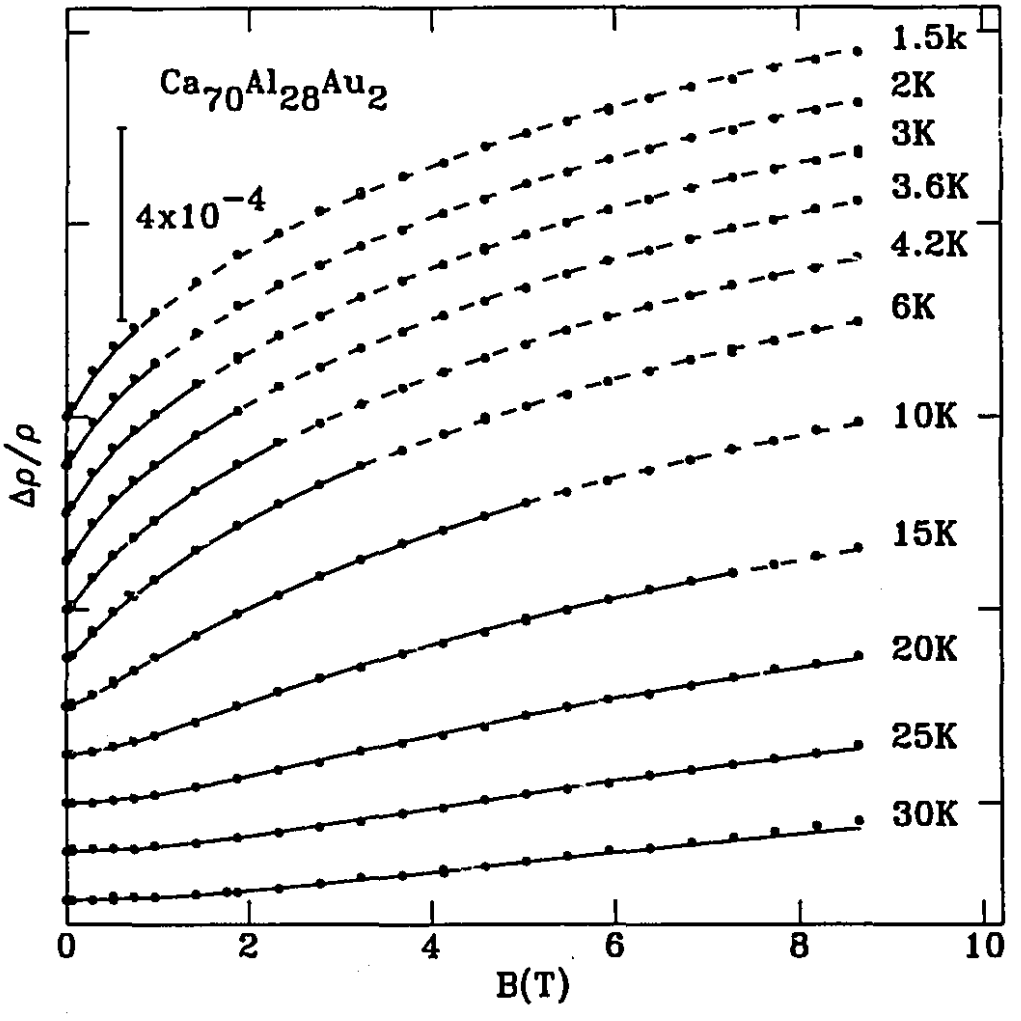

Figure 4.9: Normalized magnetoresistance of $Ca_{70}Al_{28}Au_2$. The scale and temperatures are indicated in the figure. The points are the experimental data, the solid line the fitted magnetoresistance (Eq. 2.14) and the dashed line its extrapolation as described in the text.

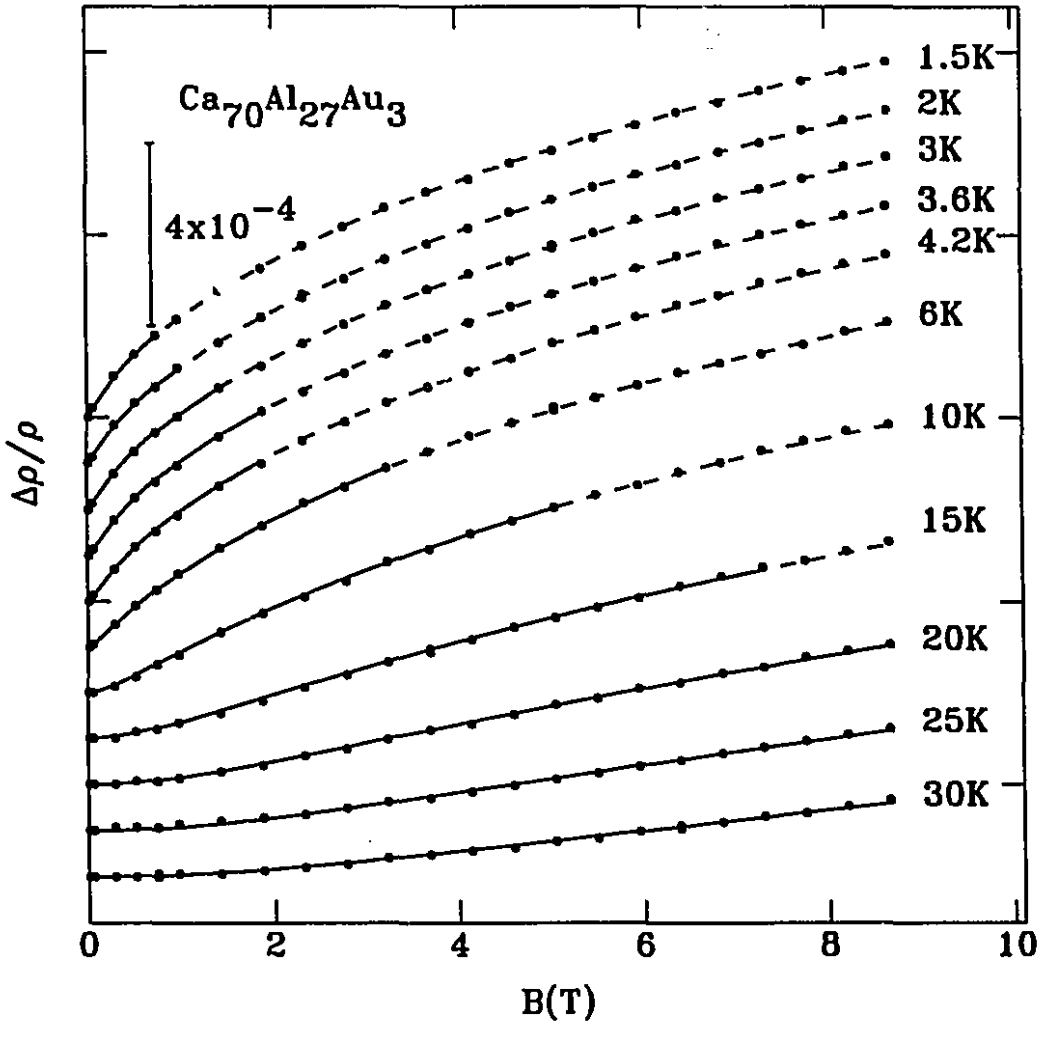

Figure 4.10: Normalized magnetoresistance of $Ca_{70}Al_{27}Au_3$. The scale and temperatures are indicated in the figure. The points are the experimental data, the solid line the fitted magnetoresistance (Eq. 2.14) and the dashed line its extrapolation as described in the text.

measurements reported by Tsai and Lu [86] on Ca-Al alloys and by Howson *et al.* [87] on Ca-Al-(Au) where the positive part of the magnetoresistance in the pure alloy (i.e. $Ca_{70}Al_{30}$) was not observed. We shall show later that this is characteristic of the presence in their samples of a relatively high amount of magnetic impurities, which both destroy phase coherence and also give rise to a negative magnetoresistance (see sections 2.1 and 2.3). As has been pointed out by Baxter *et al.* [88], the level of magnetic impurities is of particular importance since it can lead to erroneous results when quantitative analysis of the experimental data is made. This point will be further commented on below when we discuss the dephasing rate and the spin-orbit scattering rate. Here we estimate only the magnetoresistance due to the manganese, which is the only impurity present in our alloys which is expected to hold a moment in Ca-Al (see section 4.1.3). Using Eq. (2.36) with $J = -0.24$ eV and $S = 2.2$ [69, 70], we find that the contribution to the magnetoresistance of 4 ppm Mn impurity level is of the order of 2×10^{-6} and is therefore negligible compared with the contributions due to quantum corrections to the conductivity.

4.1.2 Fitting procedure

We now test whether the theoretical predictions of weak localization and enhanced electron-electron interaction provide a quantitatively accurate description of the experimental data. To do so we make use of the fact that weak localization is more sensitive to low magnetic fields than the enhanced electron-electron interaction as was demonstrated in Chapter 2 (see Figure 2.11).

A- Low field range

We start the fitting by restricting it to low fields ($B/T \leq 0.5$T/K) where only weak localization contributes to the magnetoresistance [1]. The contribution from

[1]The same procedure was successfully used in references [18, 23] to test the validity of weak localization theory in three dimensional systems. Also, a similar approach was adopted by Bergmann in quantitative analysis of the magnetoresistance of two dimensional Mg, Cu, Ag, and Au films

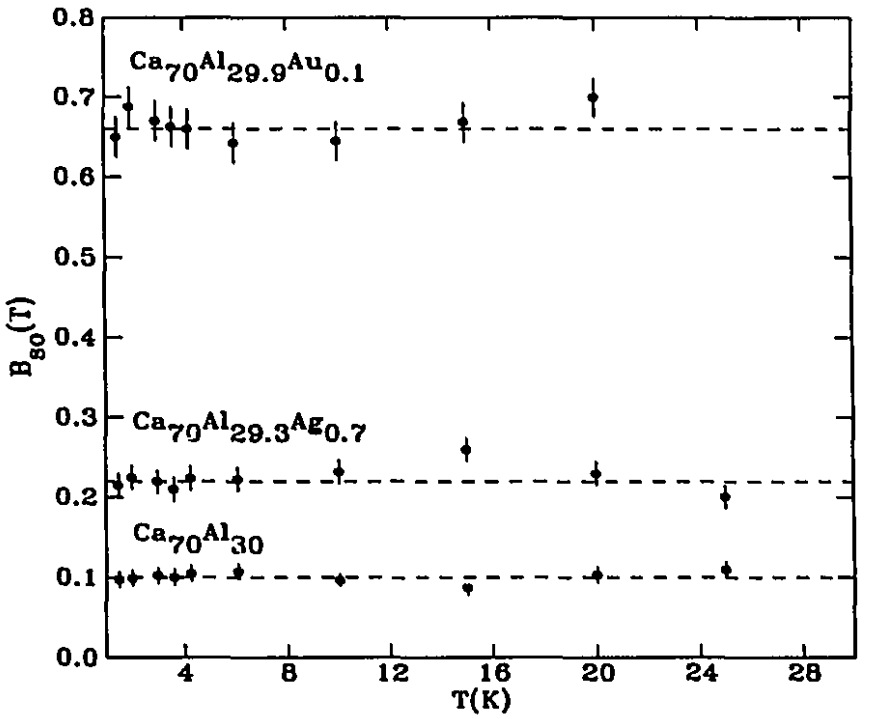

Figure 4.11: The spin-orbit scattering field, B_{so}, as a function of temperature in three different alloys. The dashed line represent the average value of B_{so}.

enhanced electron-electron interaction being negligible ($\sim 10^{-6}$). In doing so we will determine the unknown parameters; the spin-orbit field B_{so} and the dephasing field B_ϕ, in the weak localization expression (Eq. 2.14). Hence B_{so} and B_ϕ are kept as free parameters in a multiparameter least-squares fitting routine. The process stops when the deviation between the data and the theoretical expression is a minimum. In carrying out the fitting, we found that B_{so} is temperature independent (the scatter for different temperatures is less than 15% in the low spin-orbit alloys, see Figure 4.11) whereas B_ϕ increases with temperature, as expected.

To obtain an internally consistent fit, we then fix B_{so} to its average value and repeat the analysis. B_ϕ is now the only adjustable parameter. Our analysis therefore yields a well defined value of the spin-orbit field B_{so} and one value for the dephasing field B_ϕ at each temperature for each alloy. The results are given in Table 4.1. The

[10, 11, 59].

x	y	B_{so} (T)	$\bar{F}_\sigma$	B_ϕ (mT)										
				T(K)										
				1.5	2	3	3.6	4.2	6	10	15	20	25	30
0	0	0.1	0.56	12	11	16	16	18	27	190	500	960	1750	-
0.3	0	0.15	0.47	7	10	12	15	17	32	180	420	910	1280	-
0.7	0	0.22	0.40	9	9	12	15	17	29	98	480	810	1610	-
2	0	0.46	0.24	7	8	10	12	16	26	106	290	900	1620	-
0	0.1	0.66	0.18	9	10	14	17	22	35	115	320	-	-	-
0	0.2	1.3	0.10	8	9	11	14	16	32	113	320	750	1030	-
0	0.4	2.4	0.07	9	10	10	13	17	30	105	340	400	555	-
0	0.8	5.0	0.01	12	12	13	17	15	33	107	350	730	1270	-
0	2	7.0	0.0	12	14	15	17	22	34	100	300	620	1000	1490
0	3	12	0.0	9	12	12	13	15	31	109	330	670	1100	1590

Table 4.1: Least-squares fitting parameters for amorphous Ca-Al-(Ag,Au). x and y refer to the Ag and Au concentrations, respectively.

significance of these results for each parameter will be discussed later.

It may be seen (Figures 4.1-10) that the agreement between the theory and the experiment is excellent in the field range over which the fit is made. Moreover the fit is equally good at all temperatures and for all samples. Similar results were found by several authors in various systems [14, 15, 16, 23, 28].

B- Full field range

Now if we extrapolate the weak localization contribution to higher field values one can immediately see that it underestimates the measured data especially at lower temperatures and in alloys containing small amounts of Ag or Au (the dashed lines in Figures 4.1-10). This gap is in fact a direct reflection of the missing positive enhanced electron-electron interaction which is expected to be important in this field

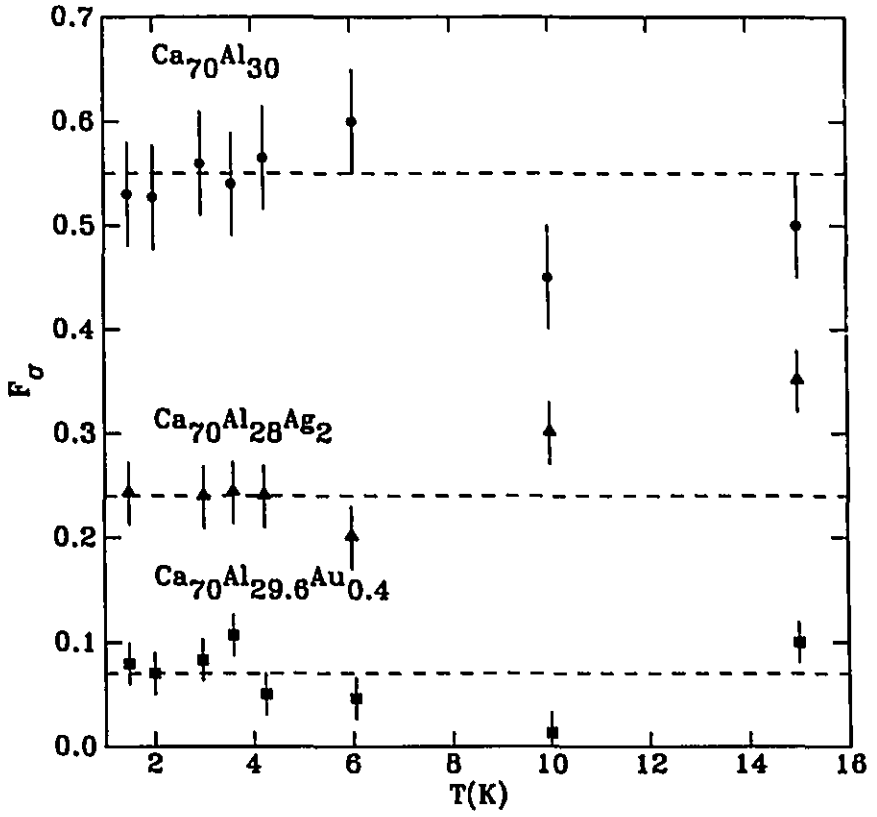

Figure 4.12: The interaction constant, $\tilde{F}_\sigma$, as a function of temperature in three different alloys.

range. We therefore, as a second step, extend the fit to the entire field range including the enhanced electron-electron contribution with the only free parameter being the interaction constant $\tilde{F}_\sigma$. As mentioned in section 2.3, only the diffusion channel contribution is retained in the fitting.

Like B_{so}, $\tilde{F}_\sigma$ should also be temperature independent (see Figure 4.12; at high temperatures, $T \geq 15$K, the diffusion channel contribution is so small that the values of $\tilde{F}_\sigma$ are not reliable).

Hence the final theoretical curves in Figures 4.13-22 are generated with common values of B_{so} and $\tilde{F}_\sigma$ and a value of B_ϕ at each temperature for each family of curves. Again, the agreement between the theory and experiment is excellent but now over the full range of field and temperature. Furthermore, the quality of the fit is equally good for all alloys irrespective of their chemical composition. Thus our first signifi-

cant conclusion is that quantum corrections to the conductivity expressions give the right field and temperature dependence of the magnetoresistance in this alloy system, regardless of the level of the spin-orbit scattering. Furthermore there was no need to include the Cooper channel contribution in the fitting. Weak localization and diffusion channel contributions are sufficient to describe the experimental data; provided the interaction constant $\tilde{F}_\sigma$ is allowed to vary from one alloy to the other (for details on this point see subsection 4.1.5). Moreover we stress that our analysis effectively involved only one temperature dependent variable, (B_ϕ), the dephasing field, the interaction constant $\tilde{F}_\sigma$ and the spin-orbit field B_{so} being constant in each alloy.

In most previous work on bulk systems reported by different workers, quantum corrections to the magnetoresistance fail to account for the experimental data over the whole field range. Bieri and coworkers [15, 89] have investigated weak localization and enhanced electron-electron interaction in a large series of metallic glasses ($Mg_{80}Cu_{20}$, $Cu_{57}Zr_{43}$, $Pd_{80}Si_{20}$, $\cdots$ etc). Although the theory describes the data very well at low fields, there is a substantial discrepancy at large fields. The same problem was encountered by Ousset *et al.* for amorphous V-Si alloys [16], Olivier *et al.* for Y-Al [17] and Richter *et al.* for the simple Mg-Cu alloys [23, 83]. The deviations observed between the theory and experiment in these systems at high magnetic fields have been attributed to a variety of sources. First according to Isawa [90], the weak localization magnetoresistance is overestimated because of the approximations used in deriving expressions (2.14). However Baxter *et al.* [88] have numerically shown that the difference between the proposed magnetoresistance of Isawa [90] and that given in (2.14) is completely negligible in metallic glasses such as the Ca-Al alloys considered here. Consequently Isawa's argument cannot justify the observed failure of weak localization theory for these systems. Another suggestion was that the magnetoresistance expression (2.14) is only adequate in the limit of weak spin-orbit scattering [19]. This argument is however discredited by the excellent agreement between the data and the theory in the present Ca-Al-(Ag,Au) system and by the results of Bergmann

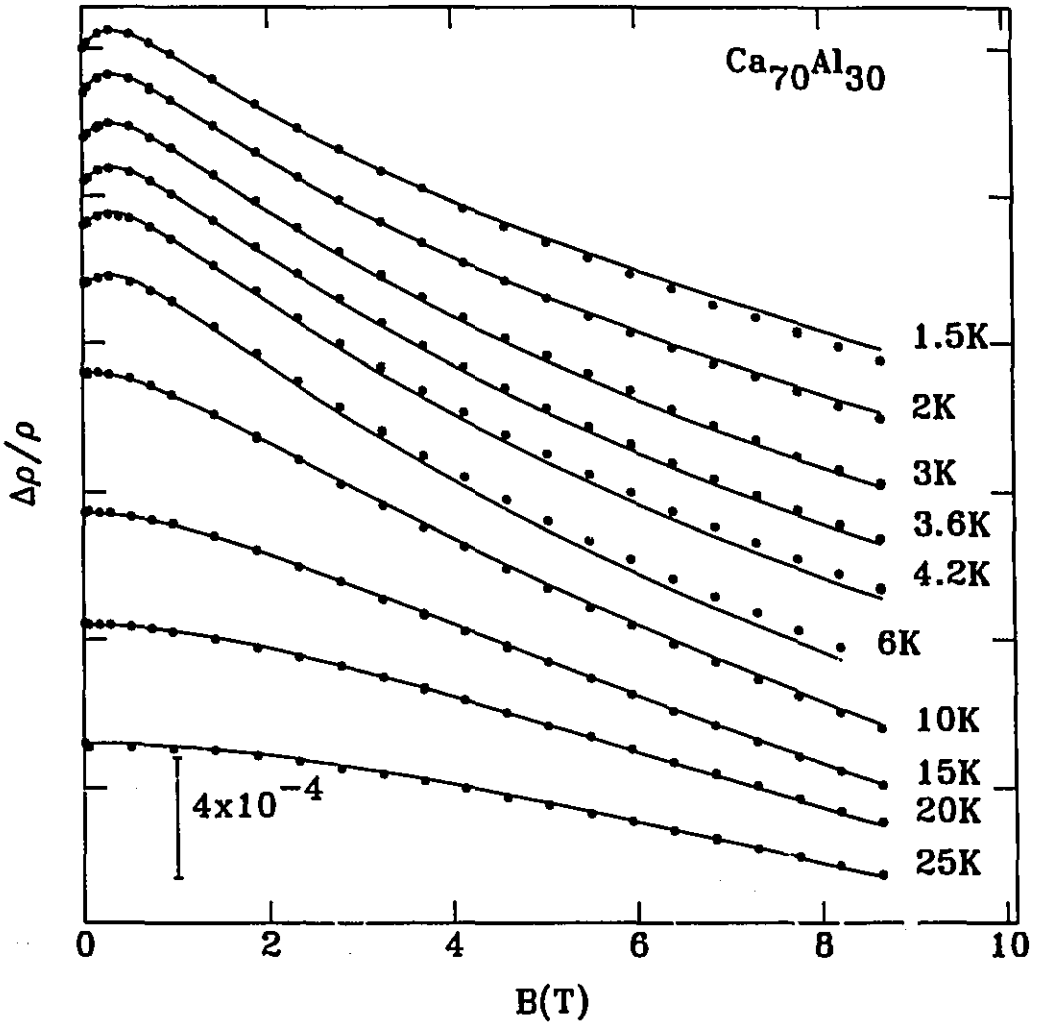

Figure 4.13: Normalized magnetoresistance of $Ca_{70}Al_{30}$. The scale and temperatures are indicated in the figure. The points experimental data and the solid line the fitted magnetoresistance (Eq. 2.14, 2.29) as explained in the text.

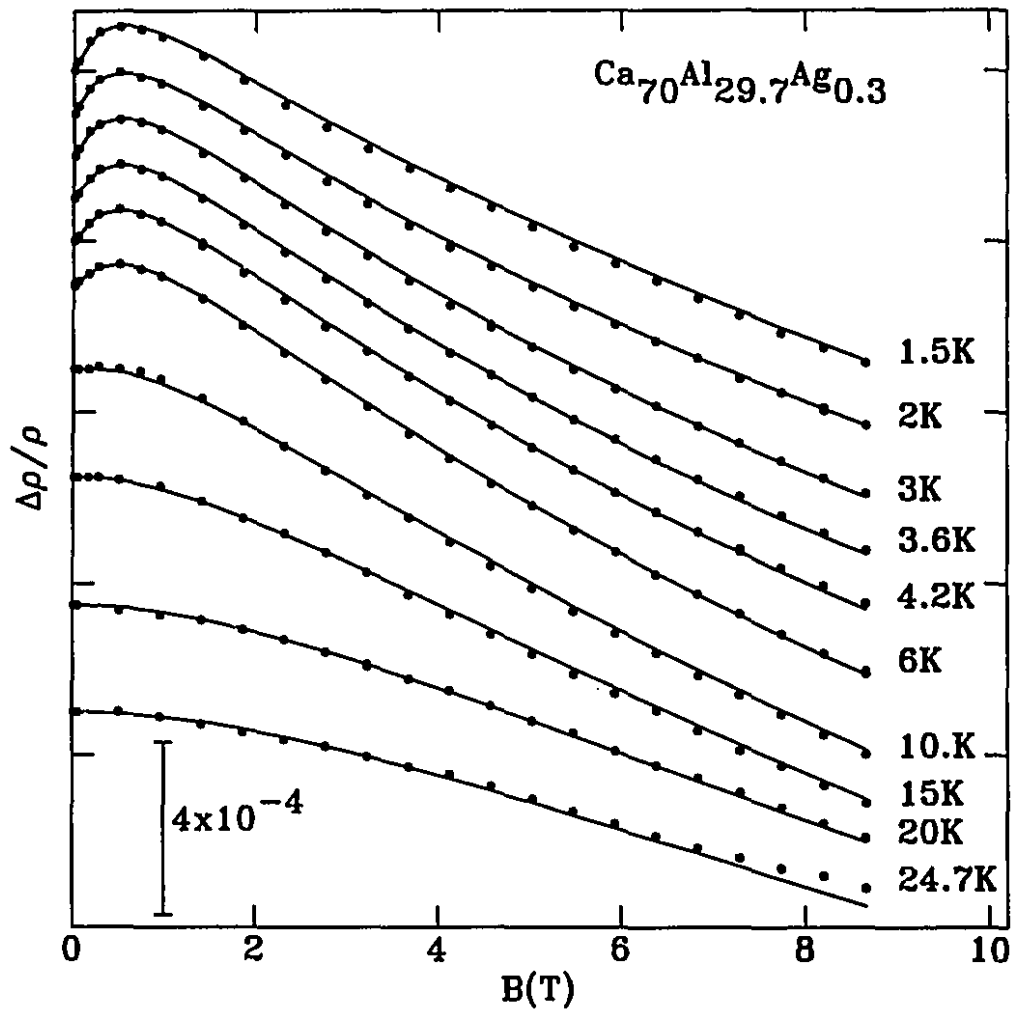

Figure 4.14: Normalized magnetoresistance of $Ca_{70}Al_{29.7}Ag_{0.3}$. The scale and temperatures are indicated in the figure. The points experimental data and the solid line the fitted magnetoresistance (Eq. 2.14, 2.29) as explained in the text.

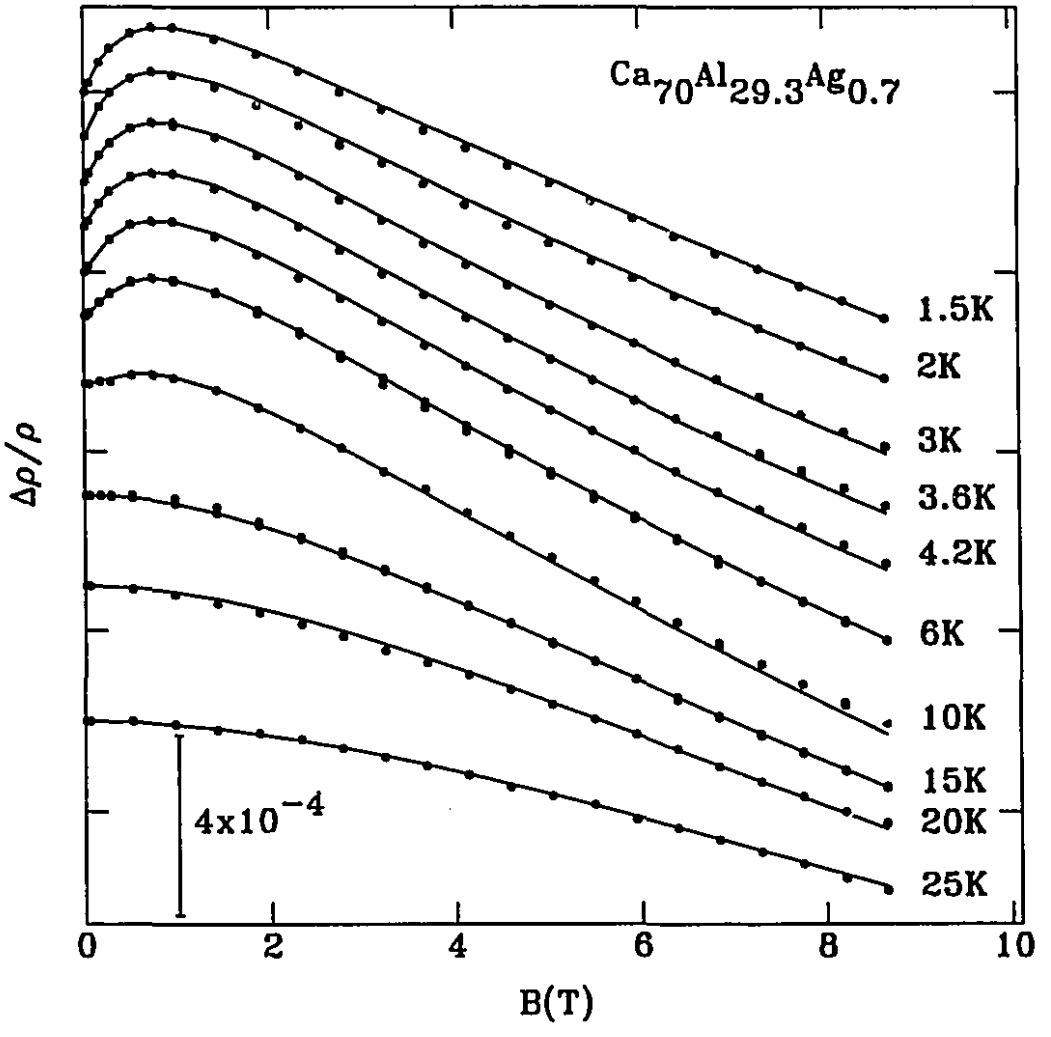

Figure 4.15: Normalized magnetoresistance of $Ca_{70}Al_{29.3}Ag_{0.7}$. The scale and temperatures are indicated in the figure. The points experimental data and the solid line the fitted magnetoresistance (Eq. 2.14, 2.29) as explained in the text.

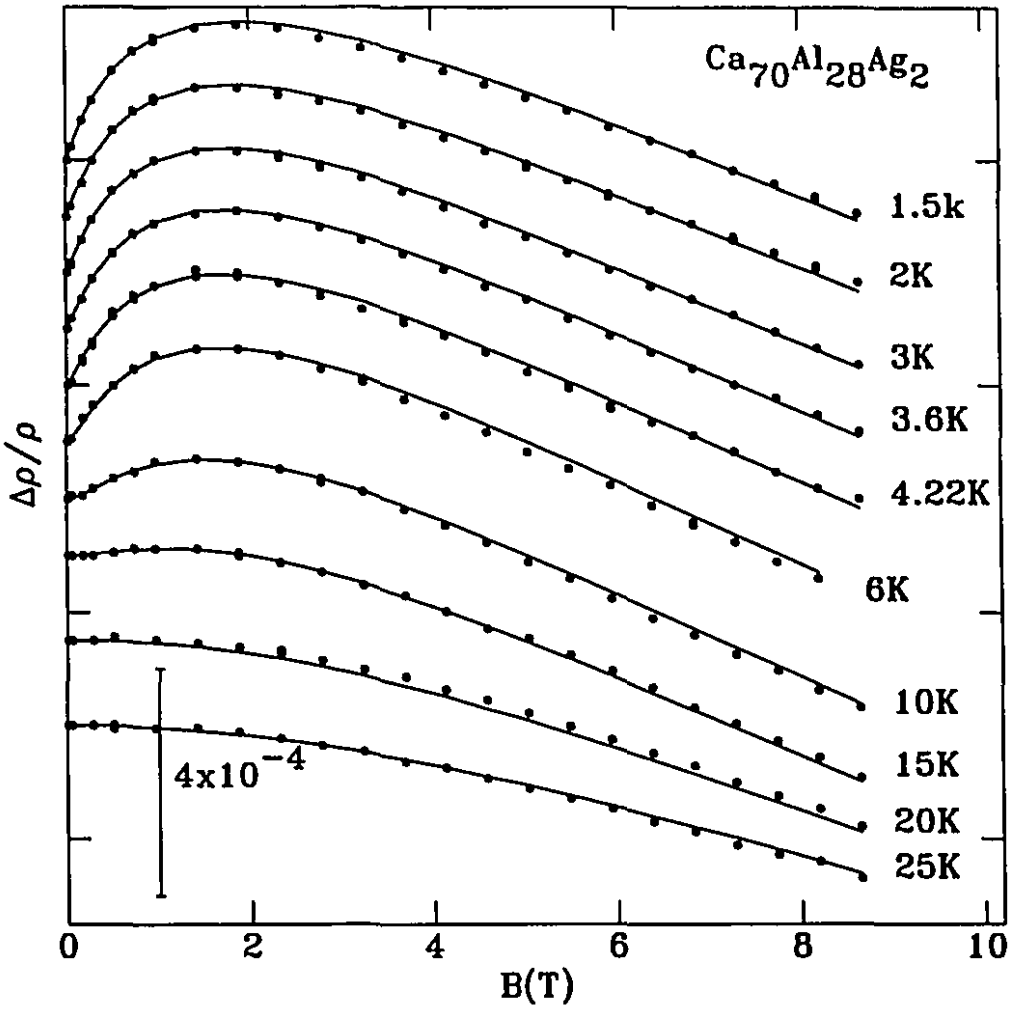

Figure 4.16: Normalized magnetoresistance of $Ca_{70}Al_{28}Ag_2$. The scale and temperatures are indicated in the figure. The points experimental data and the solid line the fitted magnetoresistance (Eq. 2.14, 2.29) as explained in the text.

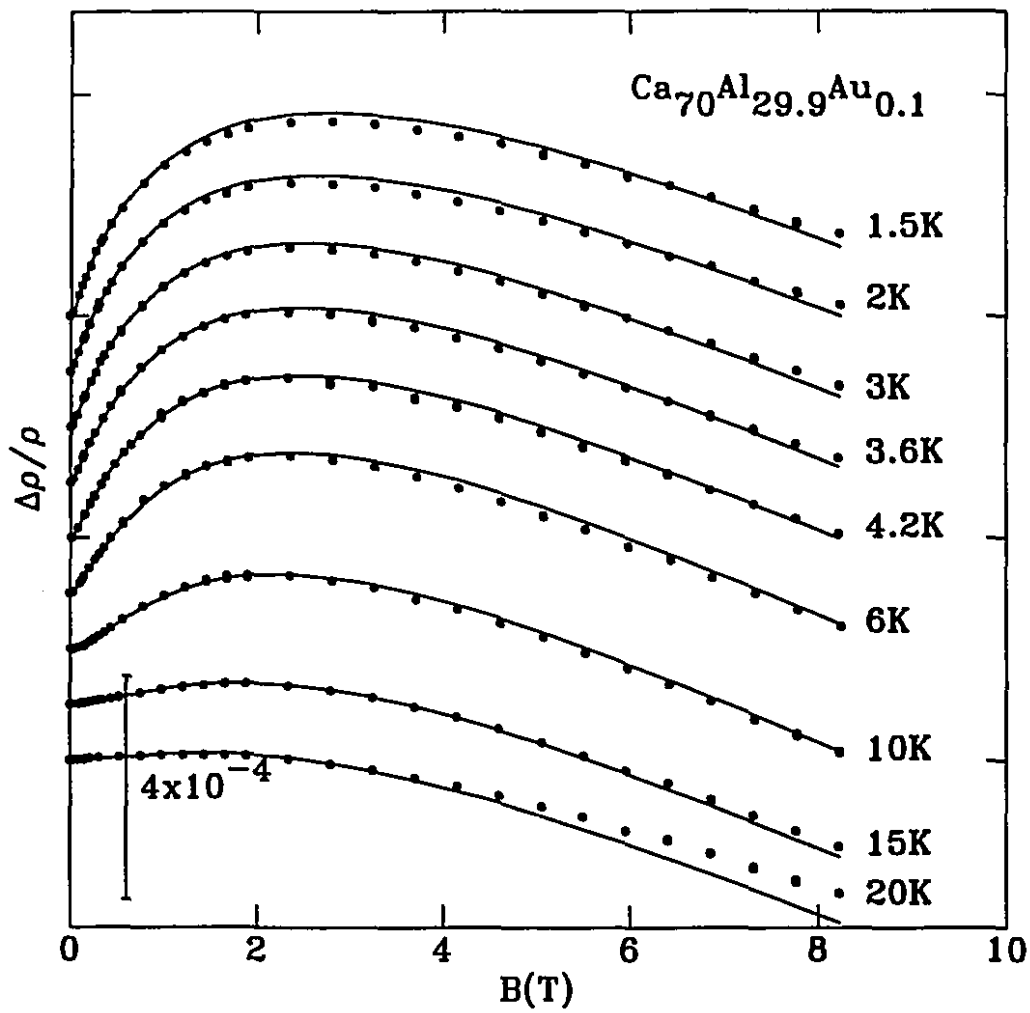

Figure 4.17: Normalized magnetoresistance of $Ca_{70}Al_{29.9}Au_{0.1}$. The scale and temperatures are indicated in the figure. The points experimental data and the solid line the fitted magnetoresistance (Eq. 2.14, 2.29) as explained in the text.

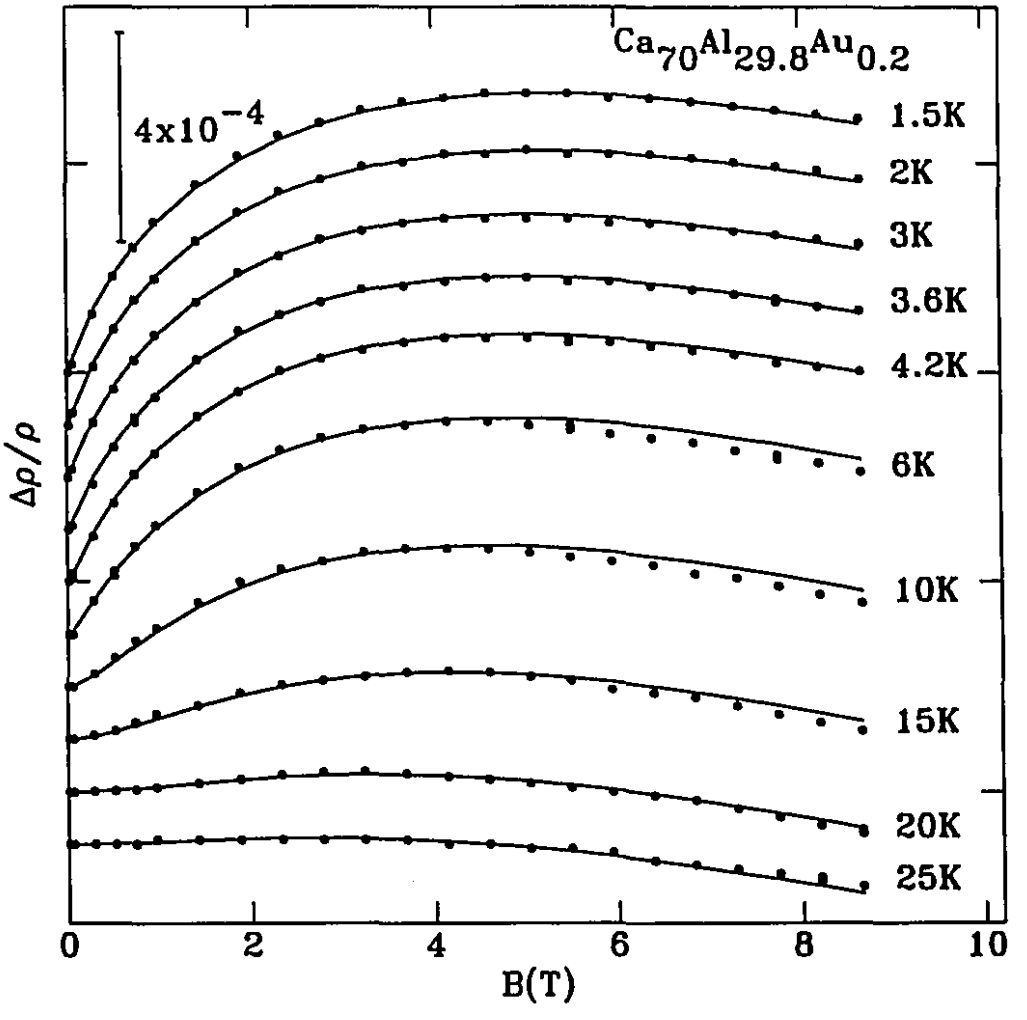

Figure 4.18: Normalized magnetoresistance of $Ca_{70}Al_{29.8}Au_{0.2}$. The scale and temperatures are indicated in the figure. The points experimental data and the solid line the fitted magnetoresistance (Eq. 2.14, 2.29) as explained in the text.

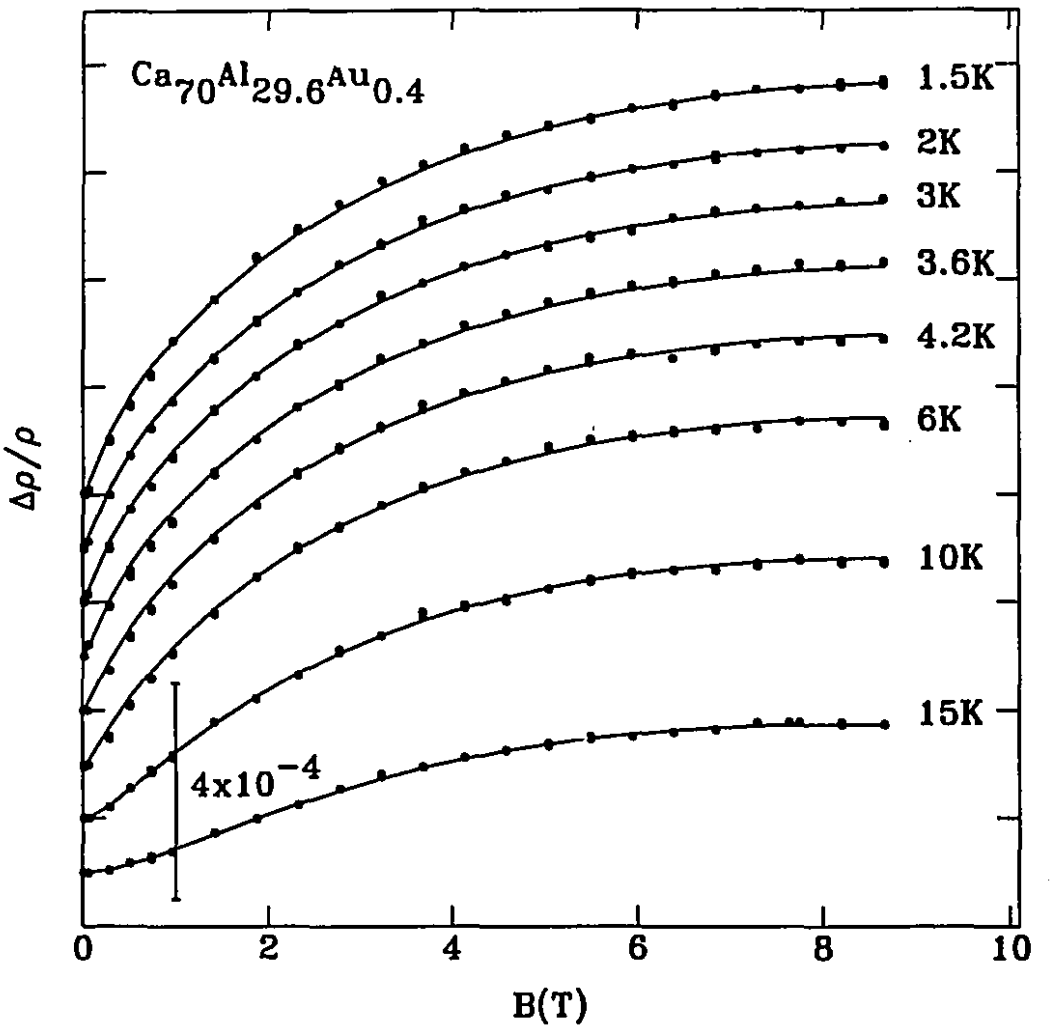

Figure 4.19: Normalized magnetoresistance of $Ca_{70}Al_{29.6}Au_{0.4}$. The scale and temperatures are indicated in the figure. The points experimental data and the solid line the fitted magnetoresistance (Eq. 2.14, 2.29) as explained in the text.

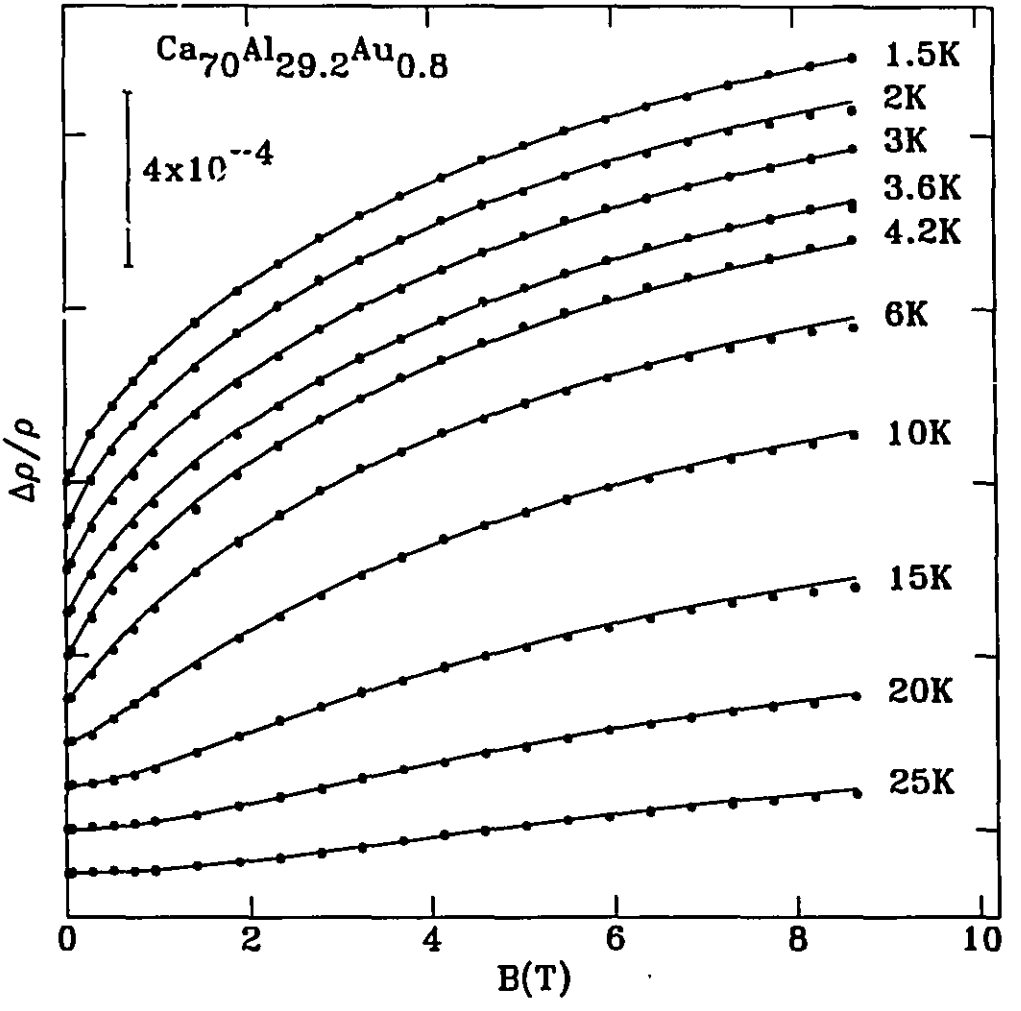

Figure 4.20: Normalized magnetoresistance of $Ca_{70}Al_{29.2}Au_{0.8}$. The scale and temperatures are indicated in the figure. The points experimental data and the solid line the fitted magnetoresistance (Eq. 2.14, 2.29) as explained in the text.

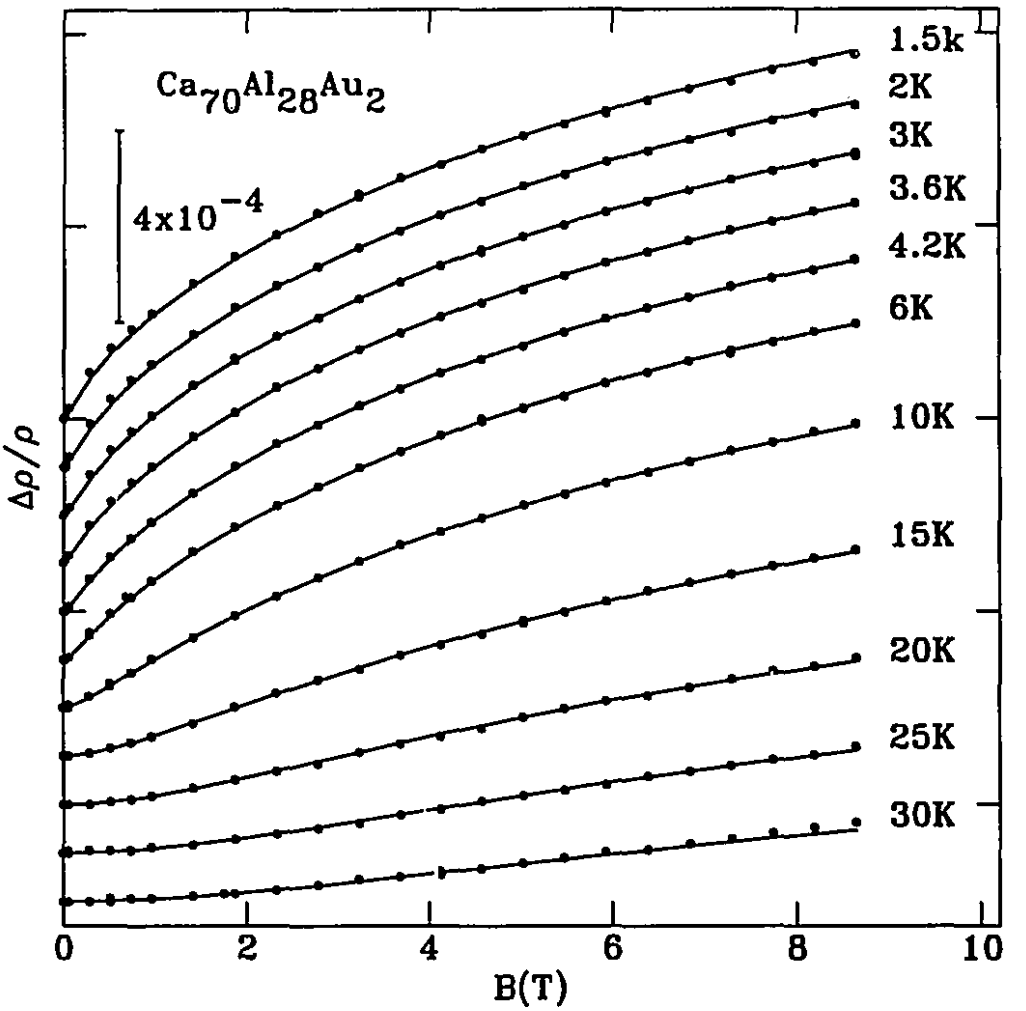

Figure 4.21: Normalized magnetoresistance of $Ca_{70}Al_{28}Au_2$. The scale and temperatures are indicated in the figure. The points experimental data and the solid line the fitted magnetoresistance (Eq. 2.14, 2.29) as explained in the text.

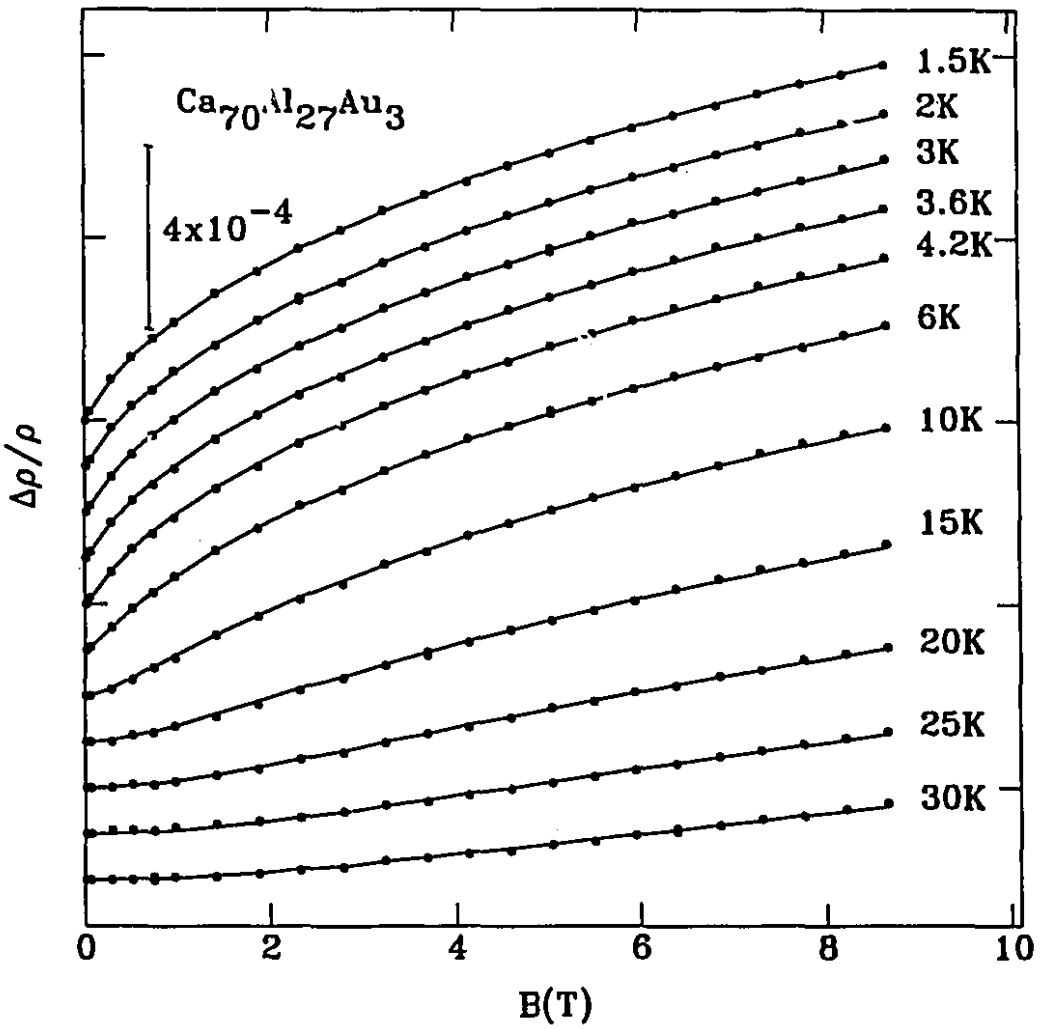

Figure 4.22: Normalized magnetoresistance of $Ca_{70}Al_{27}Au_3$. The scale and temperatures are indicated in the figure. The points experimental data and the solid line the fitted magnetoresistance (Eq. 2.14, 2.29) as explained in the text.

in Mg/Au and thin films where a remarkable quantitative description of the data by weak localization was also found [11, 59].

Before we start the analysis of the results for B_ϕ, B_{so} and $\tilde{F}_\sigma$ we note that very recently Gey *et al.* [91] and Mayeya and Howson [92] have studied the Ca-Al and Ca-Al-(Ag,Au) systems respectively, and confirmed our measurements and thus lend strong support to our results. Discarding the Cooper channel contribution in the analysis is well justified. As we mentioned before, the Cooper channel contribution is very small in these alloys. Approaches similar to ours were adopted by several authors [93, 28, 92, 94]. In particular Trudeau and Cochrane have found, using the weak localization and diffusion channel contributions only, an excellent agreement between the magnetoresistance data in paramagnetic amorphous Fe-Zr alloys and the theory. More closely related to the present work is the recent report of Mayeya and Howson on the Ca-Al-(Ag,Au) in which the authors followed the same analysis procedure [92]. To summarize, based on the results presented here and on our earlier work [18, 19, 30], we have shown using a strict fitting procedure that the current quantum corrections to the conductivity as given in Chapter 2 provide a very good tool to describe the low temperature magnetoresistance of amorphous Ca-based alloys not only over a wide range of B/T [19] but also over a wide range of spin-orbit scattering (see subsection 4.1.4). The observed discrepancy in other systems is still not understood. However it is worth mentioning that, unlike the Ca-based alloys considered here, most of those systems present serious complications: d-band conduction due to the presence of transition metal elements [17, 24, 28, 89], superconductivity [28, 95], magnetic behavior [96] or high level of magnetic impurities [15], render the analysis difficult and less conclusive. Thus a comprehensive investigation of quantum corrections to the conductivity in such systems will only be possible once the contributions, for example from the effects just cited above, are separated and well understood.

4.1.3 The dephasing rate $1/\tau_\phi$

Figure 4.23 shows the dephasing rate, $1/\tau_\phi = 4eDB_\phi/\hbar$, plotted as a function of temperature. An immediate remark is that there is a universal behavior of the dephasing rate in all the samples. It has the same magnitude and is independent of the alloy composition, hence providing a powerful consistency check to the results. The temperature dependence of the dephasing rate $1/\tau_\phi$ is well described by the expression:

$$\frac{1}{\tau_\phi} = \frac{1}{\tau_\phi^0} + AT^p. \tag{4.1}$$

The most important parameter here is the exponent p from which one can in principle determine the mechanism responsible for the destruction of the electron's wavefunction phase coherence. The best fit is obtained for $p = 3.0 \pm 0.3$, $A \approx 1.1 \times 10^8 \mathrm{s}^{-1}/\mathrm{K}^3$ and $1/\tau_\phi^0 = 1.05 \times 10^{10}\mathrm{s}^{-1}$ (the solid line in Figure 4.23). This means that at high temperatures ($T \geq 6\mathrm{K}$) $1/\tau_\phi$ varies rapidly with temperature and obeys a T^3. A similar power law dependence has also been reported by other workers using different materials but in some cases their results give smaller values of the exponent p. In Mg films [6, 10] and in various metallic glasses [15, 17, 94] $1/\tau_\phi$ varies as T^2. On the other hand Hickey and coworkers found a T^3 dependence in Cu-Ti-(Au) glasses over a wide range of composition. Also, Richter *et al.* [83] found in Mg-based amorphous alloys that $1/\tau_\phi$ is also described by the same equation as Eq. (4.1).

Below 4.2 K, the dephasing rate $1/\tau_\phi$ saturates to the value $1/\tau_\phi^0$. Many authors have discussed this behavior and suggested a number of causes. Among them are: residual spin scattering from magnetic impurities present in the samples; dephasing due to zero-point motion; decoupling of the electron gas from the thermal bath; or scattering by paramagnetic states. In our alloys the last two explanations are ruled out. Thermal decoupling of the electron gas from the thermal bath above 1.5 K is unlikely. Bergmann and coworkers [97] and Liu *et al.* [98] have shown in Au and Ag films respectively, that the electron gas can only be overheated when the current densities exceed $\sim 2 \times 10^9$ A/m^2 at 4.2 K. In the present measurements of the resistivity above 1.5 K, the current densities were always less than 200 A/m^2,

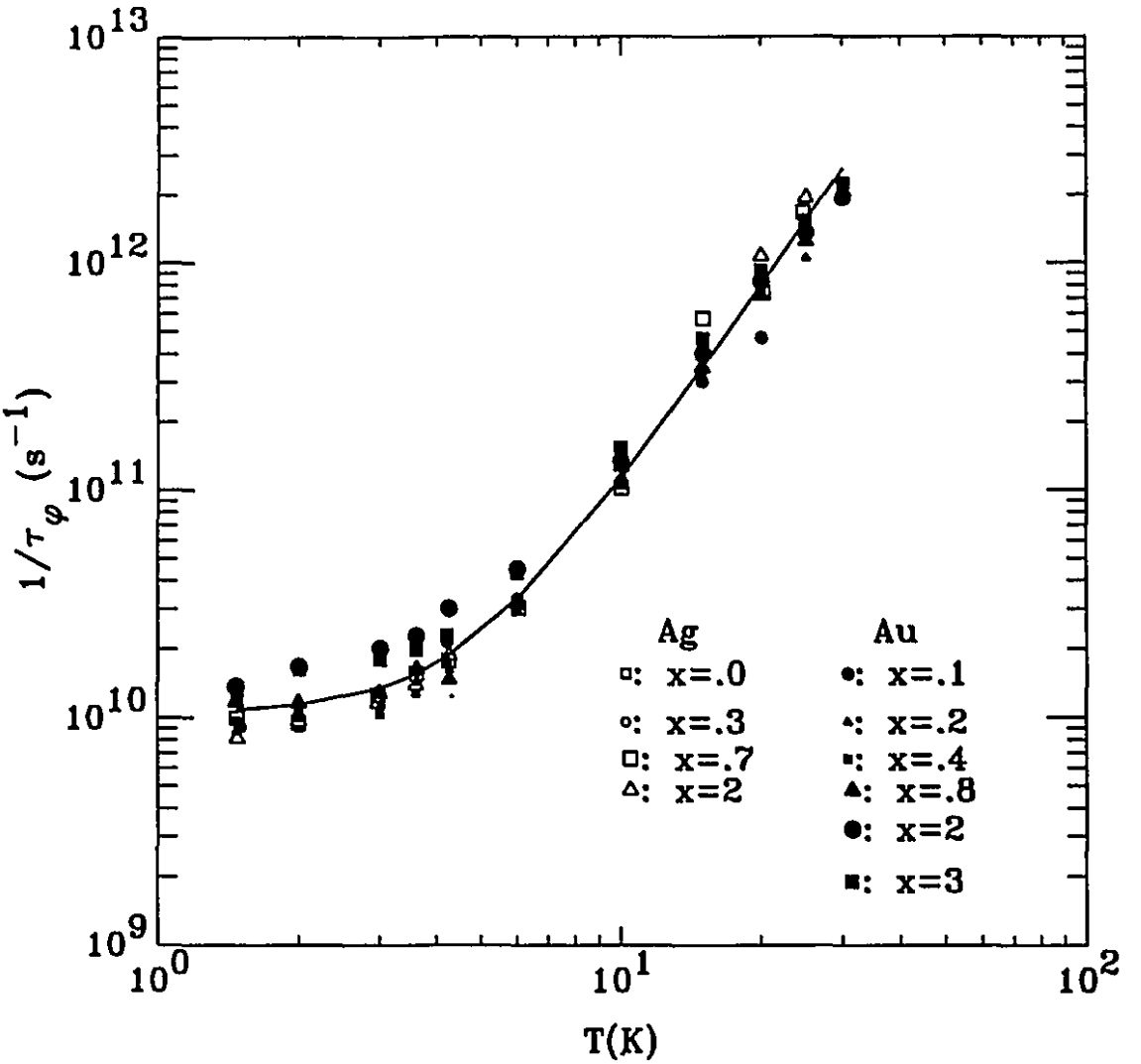

Figure 4.23: The dephasing rate $1/\tau_\phi$ in amorphous Ca-Al-(Ag,Au) alloys as a function of temperature. The solid line is a fit as described in the text.

besides the fact that the samples were directly immersed in liquid helium below 4.2 K. The scattering by paramagnetic surface effects is also unlikely to influence $1/\tau_\phi$; this mechanism is expected to be important only in very thin films and not in thick bulk materials like the ones considered here.

The third alternative for the low temperature behavior of $1/\tau_\phi$ is dephasing due to zero-point motion. This possibility has been proposed by Kumar *et al.* [99], based on the results of the dephasing rate in Mg-Cu and Mg-Zn amorphous alloys [23], where none of the other sources, listed above, could explain the saturation of $1/\tau_\phi$. Thermal decoupling of the electron gas and paramagnetic surface effects were ruled out for the same reasons as above. Magnetic impurity contamination was too low ($\leq$ 0.2 ppm) to give a significant contribution to $1/\tau_\phi$. The model is based on the idea that virtual phonon exchange could lead to dephasing by independently changing the phase of the two complementary electron paths around a closed loop (see section 2.1) even though the final energy of the electron is unchanged. Although this view has recently received some support [100, 101, 102] many workers have questioned its validity [103, 104, 105]. Unfortunately, because of the presence of the magnetic impurities in our samples (see below), it is not possible from our results to either confirm or disprove this model.

As mentioned before, there is about 4 ppm Mn content in our samples. Therefore a possible explanation for the saturation is spin-scattering by this magnetic impurity. Indeed, using the expression (2.23) for the magnetic spin scattering rate, we obtain for 4 ppm impurity level of Mn atoms:

$$\frac{2}{\tau_s} \simeq 9.6 \times 10^9 \mathrm{s}^{-1}, \tag{4.2}$$

where we have taken $S = 2.2$ and $J = -0.24$ eV on the Mn atom [69, 70]. This value is very close to the saturation value:

$$\frac{1}{\tau_\phi^0} \simeq 1.05 \times 10^{10} \mathrm{s}^{-1}. \tag{4.3}$$

However, we should notice that, since there is no data available in the literature about the magnetic moment of dilute Mn in pure Ca which represents 70% of our alloys, it

was assumed that Mn atoms hold a moment in our Ca-based alloys just on the basis that they have a moment in Mg [83] which has a similar electronic configuration as that of Ca.

To conclude, based on our estimation of $1/\tau_s$, we are led to attribute the observed saturation of $1/\tau_\phi$ at low temperatures in Ca-Al-(Ag,Au) system to residual magnetic spin-scattering. The same conclusion was also reached in the recent work by Mayeya and Howson [92] on the same alloy system.

4.1.4 The spin-orbit scattering rate $1/\tau_{so}$

The spin-orbit scattering rate,$1/\tau_{so} = 4eDB_{so}/\hbar$, as deduced from the low field range fitting using the weak localization expression, is shown in Figure 4.24. The large error bars at 2 and 3 at.% of Au are due to the fact that the relatively featureless magnetoresistance data at these concentrations are relatively insensitive to the exact value of $1/\tau_{so}$. Where spin-orbit scattering is low the magnetoresistance changes sign at accessible magnetic fields and this defines τ_{so} much more precisely. The spin-orbit scattering rate changes by more than two orders of magnitude from 8.2×10^{10} to $1.52 \times 10^{13}\text{s}^{-1}$ (see Table 3.1). The value for $Ca_{70}Al_{30}$ is consistent with our previous results. However the value reported by Howson and coworkers [87] is significantly different ($\sim 10^4\text{s}^{-1}$). This unphysically low value is probably an artifact of a high value of magnetic impurities which suppress the positive part of the magnetoresistance at low field as was shown in Figure 2.6.b. In fact, using our value of $1/\tau_{so}$ we find that in order to reproduce their data $1/\tau_\phi$ must take a value of $\approx 2 \times 10^{11}\text{s}^{-1}$. From this we can infer a magnetic impurity contamination (assuming Mn is the impurity and using the same parameters as above) of about 50 ppm in the samples used in reference [87], which again underscores the need to use materials of the highest purity when studying the quantum corrections to the conductivity in disordered systems. It is also interesting to note that even at the largest concentration of Au, i.e. 3 at.%, the condition $1/\tau_e \gg 1/\tau_{so}$ (τ_e is the elastic scattering time) under which the weak localization expression (Eq. 2.14) was derived is still satisfied since $1/\tau_e \sim 10^{15}\text{s}^{-1}$

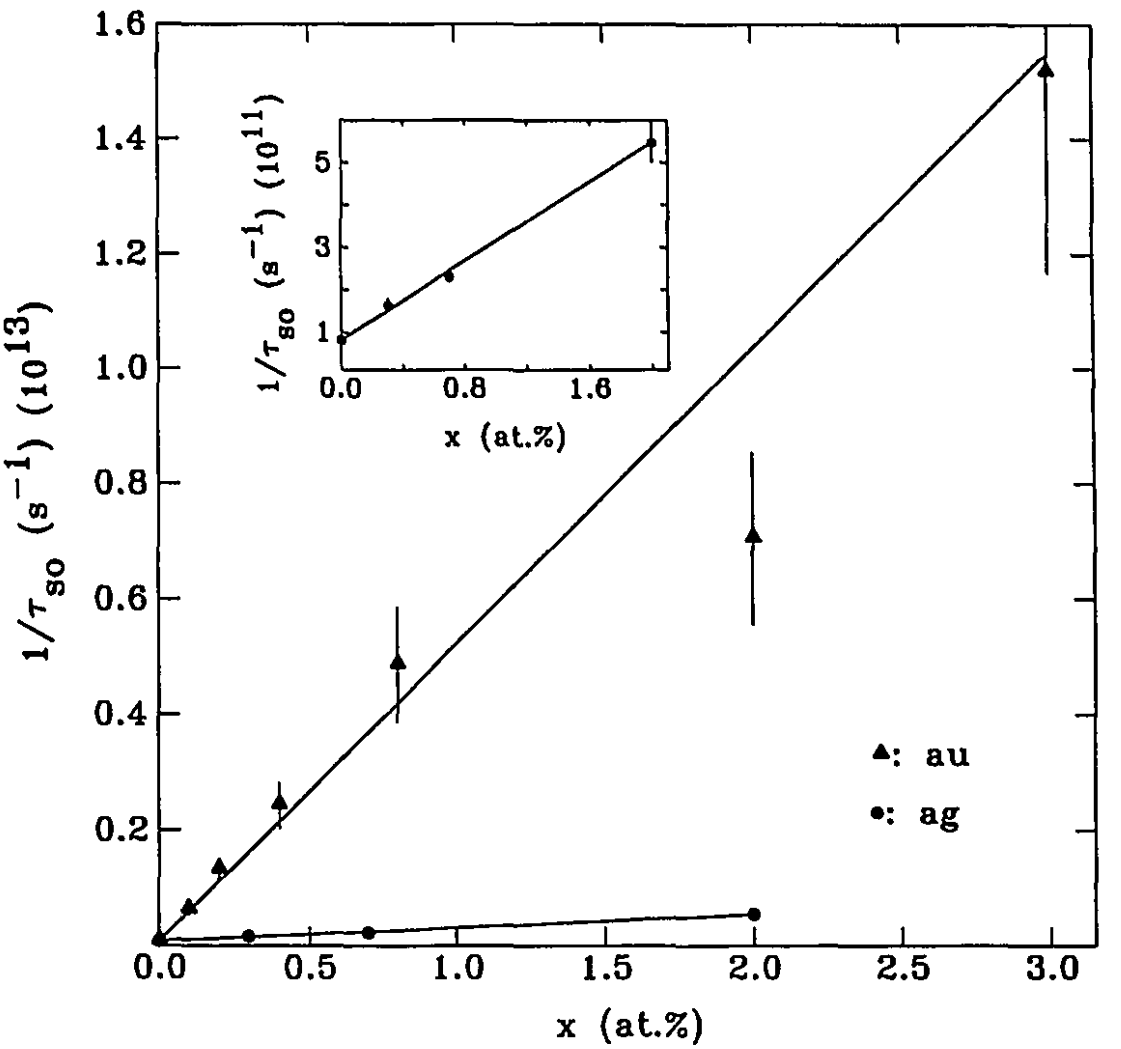

Figure 4.24: The spin-orbit scattering rate $1/\tau_{so}$ as a function of the Ag and Au concentration in amorphous Ca-Al-(Ag,Au) alloys. Inset: $1/\tau_{so}$ for $Ca_{70}Al_{30-x}Ag_x$ on an enlarged scale. The solid line is a guide to the eye.

(see subsection 2.1.1).

It may be seen from Figure 4.24 that the spin-orbit scattering rate increases linearly with concentration; however the increase is much faster for Au than Ag, as expected. The ratio between the slopes is $\simeq 21$. A similar result was found by Mayeya and Howson [92] in this alloy system and by Richter *et al.* [23, 83] in Mg-Cu and Mg-Zn amorphous alloys also doped with Ag and Au over the same concentration range, although the absolute value of the spin-orbit scattering rate at a given Ag or Au content is larger in the present case. As noted in section 2.1.3, in the simplest case where the electrons are assumed to move on hydrogenic orbits, the matrix element (M_{so}) in Eq. (2.22) is proportional to Z^4/n^3, where Z is the atomic number and n the principal quantum number [68]. This yields a spin-orbit scattering rate which should vary as Z^8/n^6. Then in our case, since $Z_{Au} = 79$ and $Z_{Ag} = 47$ and $n = 5$ and 4 respectively [2] one expects, if this description is valid, the ratio of the slopes of the two lines approximating the data in Figure 4.24 to be around $(Z_{Au}/Z_{Ag})^8 (n_{Ag}/n_{Au})^6 = 16.67$. Our value and that of references [23] and [92] range from 20 to 22.5, not too far from the estimated one. Therefore, even though the hydrogenic picture is a very simplistic idea, its predictions give a good estimate of the spin-orbit interaction dependence on atomic parameters.

Finally we should mention that there are different conventions in defining τ_{so} [93]. This has to be taken into account when specific comparisons with the results from different groups are made. In the present case we have assumed an isotropic spin-orbit scattering, i.e. $1/\tau_{so}^x = 1/\tau_{so}^y = 1/\tau_{so}^z = 1/(3\tau_{so})$ [3]. Therefore a factor of 3 exists, for example, between our definition of $1/\tau_{so}$ and that of reference [14].

[2] Following the work of Mayeya and Howson [92] we assume that it is the $5p$ and $4p$ orbitals that should be considered.

[3] Even though τ_{so} is not isotropic in general, this definition makes negligible difference in bulk disordered metals.

4.1.5 The influence of spin-orbit scattering on the diffusion channel contribution to the magnetoresistance

In this section we discuss the influence of spin-orbit scattering on the enhanced electron electron interaction through the third and last parameter we have deduced from the magnetoresistance fits; i.e. $\tilde{F}_\sigma$. As stated in Chapter 2 (section 2.2.1), the magnetic-field-dependent part of the diffusion channel correction to the resistivity (Eq. 2.29) is due to the interaction between the electrons with a total spin moment $j = 1$ and $M = \pm 1$ [3, 4, 26] [4]. In the presence of a spin scattering, this magnetic field dependence is suppressed when the Zeeman energy

$$g\mu_B B \ll \frac{\hbar}{t_s}, \tag{4.4}$$

where t_s is the total spin relaxation time given by Eq. (2.23). Physically, this is because, in the presence of a magnetic field the dephasing time for electron-electron interaction is controlled by the Zeeman energy gap $g\mu_B B$ between the spin-up and spin-down interacting electrons rather than just temperature. The spin-mixing effect of spin scattering shortens this dephasing time and leads to a field-independent electron-electron interaction for strong spin scattering. As a result the magnetoresistance from the triplet state with $M = \pm 1$ disappears. Following our discussion of the saturation of the dephasing rate at low temperatures, in subsection 4.1.3, we assume $1/\tau_s$ to be constant and equal to $1/\tau_\phi^0 \approx 1.05 \times 10^{10}\text{s}^{-1}$, the saturation value of $1/\tau_\phi$. The equality in the above condition (4.4) is then reached for $1/\tau_{so} \approx 1.2 \times 10^{12}\text{s}^{-1}$. It can be seen in Figure 4.25 that at this spin-orbit scattering rate, the diffusion channel contribution is already reduced to about a fifth of its low spin-orbit scattering rate value. Further increase in $1/\tau_{so}$ results in a complete removal of the effect. Note that we have used the interaction constant $\tilde{F}_\sigma$, since it appears as a scaling factor in the diffusion channel magnetoresistance expression (Eq. 2.29), as a measure of the progressive reduction of the diffusion channel contribution. It is also impor-

[4] Reference [26] contains several errors that were corrected later on by the authors in reference [106].

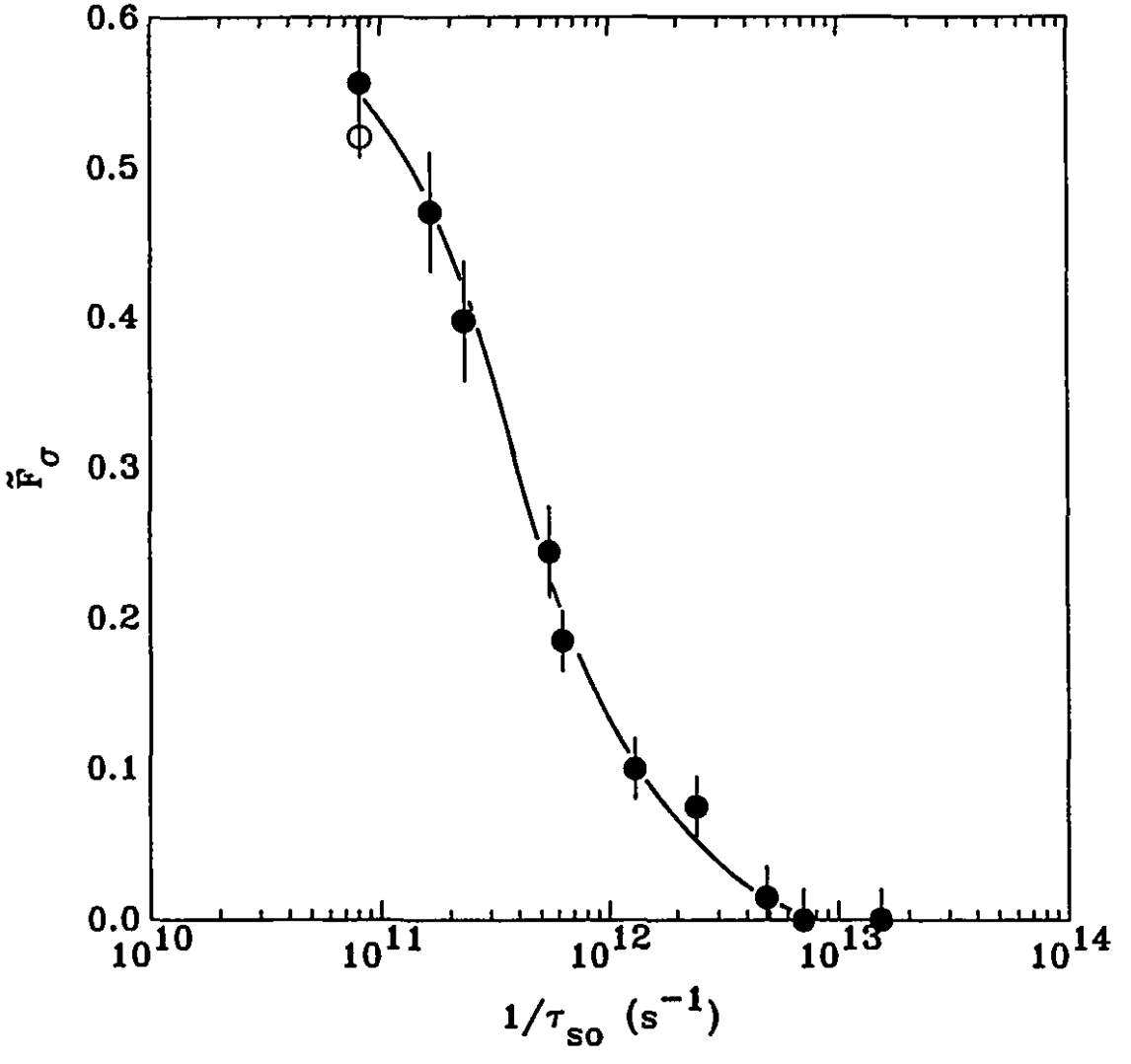

Figure 4.25: The diffusion channel contribution to the magnetoresistance ($\propto \tilde{F}_\sigma$) as a function of the spin-orbit scattering rate in amorphous Ca-Al-(Ag,Au) alloys. The open circle is the estimated free-electron value for $Ca_{70}Al_{30}$. The solid line is a guide to the eye.

tant to mention that in $Ca_{70}Al_{30}$, the value of $\tilde{F}_\sigma$ is very close to the free-electron value estimated using the Thomas-Fermi screening theory [72] (see Figure 4.25) and is therefore another indication that in this alloy we are in the limit of very weak spin-orbit scattering. In conclusion we have quantitatively shown for *the first time* the influence of spin-orbit scattering on the magnetoresistance arising from the diffusion channel [107][5]. The magnetoresistance decreases rather rapidly with increasing spin-orbit scattering. Unfortunately apart from predicting the disappearance of the diffusion channel magnetic field dependence contribution at extremely high spin-orbit scattering, there has been to our knowledge no explicit theoretical study of the effect. Therefore it is impossible to compare our finding with theory.

4.1.6 Temperature dependence of the resistivity

To complement our study of the low temperature magnetoresistance of amorphous Ca-Al-(Ag,Au) we present in this subsection the temperature dependence of the resistivity between 1.5 and 4.3 K. Figure 4.26 shows the data of all ten samples. The data are plotted as $\frac{\Delta\rho\sqrt{D}}{\rho^2}$ against $\sqrt{T}$ so that the effect of spin-orbit scattering can be clearly displayed. The solid line is a fit using the diffusion channel expression in the absence of magnetic field (see section 2.2, Eq. 2.33).

The weak localization contribution is very small and can be neglected since the temperature dependence of the resistivity comes from the dephasing time τ_ϕ which saturates over this temperature range as shown in subsection 4.1.3. As for the magnetoresistance, the fit is excellent for all alloys over the full temperature range. However the best fits are obtained for smaller values of the interaction constant $\tilde{F}_\sigma$ than those found from the magnetoresistance analysis (see Table 4.1). Moreover for large spin-orbit scattering alloys $\tilde{F}_\sigma$ has to be negative in order to fit the data. This is not an isolated case. Poon and coworkers [27] also found that it was necessary for $\tilde{F}_\sigma$ to take a negative value (-0.6) in order to account for the temperature dependence

[5]This observation has been recently confirmed, independently of this work, by Mayeya and Howson [92].

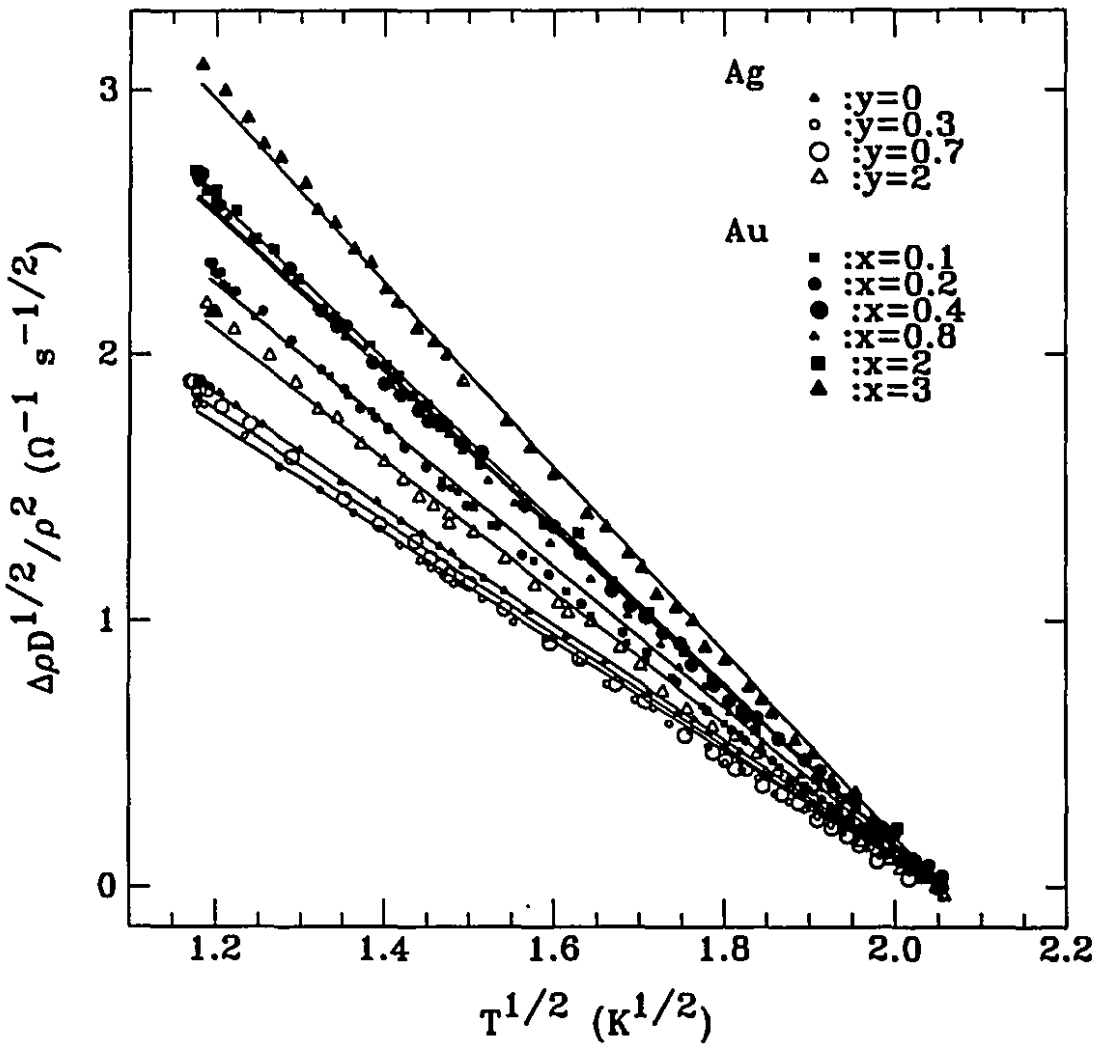

Figure 4.26: Low-temperature resistivity of amorphous Ca-Al-(Ag,Au) alloys as a function of temperature. The solid line is a fit using Eq. (2.33). The composition is indicated in the figure.

of the resistivity of amorphous Lu-Pd and Lu-Ni alloys which are characterized by a strong spin-orbit scattering ($1/\tau_{so} \sim 10^{14}\text{s}^{-1}$), about a factor of ten larger than that of $Ca_{70}Al_{27}Au_3$. Furthermore it has also been found by the same group that $\tilde{F}_\sigma \approx -0.05$ in amorphous Cu-Zr [27], where the spin-orbit scattering rate is $\approx 1.2 \times 10^{12}\text{s}^{-1}$ (Again one should note that in order to be consistent with our definition of τ_{so} the values given in reference [27] should be multiplied 3). This value is very close to that at which we observe the change of sign in our samples and is therefore consistent with our results. According to Altshuler, Aronov and Zuzin [25] the term $\frac{3}{2}\tilde{F}_\sigma$ in Eq. (2.33) should be replaced by $\frac{3}{8}\tilde{F}_\sigma$ in the limit of high spin-orbit scattering. However even with this adjustment it is not possible to account for the observed magnitude of the resistivity at large spin-orbit scattering rates. On the other hand it was suggested, since the Coulomb interaction parameter F, given by Eq. (2.27), include only the Coulomb repulsion of electrons, that F should be replaced by $F^* = F - 2\lambda$, λ being the electron-phonon mass-enhancement parameter, when attractive interaction between electrons due to the exchange of virtual phonons is included [4, 28, 87]. In this case negative values of $\tilde{F}_\sigma$ are allowed when F is small ($< 2\lambda$). But though this redefinition of F might explain the reduced values $\tilde{F}_\sigma$, it certainly fails to account for the systematic change with the spin-orbit scattering rate. Moreover, if this new definition is assumed to be valid, the attractive interaction should also be included in the magnetoresistance expression. Our results from the magnetoresistance analysis give no sign that this should be so. Therefore we are led to the conclusion that, even though it predicts the right functional dependence on temperature ($-\sqrt{T}$), the temperature dependence of the resistivity correction from the diffusion channel needs to be refined. In particular the role of spin-orbit scattering should be explicitly included in the final expression.

4.1.7 Summary

In what precedes we have shown the remarkable success of quantum corrections to the conductivity theories in predicting the low temperature magnetoresistance and

resistivity of Ca-Al-(Ag,Au) alloys, a typical high resistivity amorphous metals. This was achieved using a minimum number of free parameters and a strict fitting procedure. This allowed us to extract unambiguously the dephasing rate of the electron wavefunction and the spin-orbit scattering rate. Furthermore, our systematic study of spin-orbit scattering effect on the diffusion channel contribution to the resistivity has given an answer to a long standing question in the theory of quantum corrections to the conductivity. It is found that this contribution is very sensitive to the level of spin-orbit scattering and is completely suppressed at extremely high spin-orbit scattering rates. Even though we were not able to provide a model which incorporates this effect in the theory, our results can now serve as a benchmark for a further improvement of the diffusion channel correction to the resistivity expressions.

The next natural step is to make use of our understanding of the weak localization and enhanced electron-electron interaction contributions in amorphous metals, to gather more information on the transport properties of more complex systems. Bearing in mind that these quantum corrections to the conductivity were derived to account for the low temperature behavior of the resistivity in disordered conductors, their success or failure in describing the resistivity of non conventional metals, such as quasicrystals, offers an alternative route to the understanding of the real nature of electron conduction in these materials. It is the aim of the upcoming section to demonstrate how good this approach is.

4.2 Icosahedral Al-Cu-Fe

We follow here the same scheme as that followed in presenting the results of the Ca-Al-(Ag,Au) system in section 4.1.

4.2.1 Magnetoresistance

The magnetoresistance of the four different Al-Cu-Fe icosahedral alloys is shown in Figures 4.27-30 as a function of temperature from 1.5 to 41 K. Again, the dots rep-

resent the experimental data and the solid line the fit to the theoretical expressions, as will be shortly explained below. The magnetoresistance is at least an order of magnitude larger than that observed in amorphous systems and rises to about 12% in $Al_{62}Cu_{25.5}Fe_{12.5}$ at 1.5 K and 8.8 T (compare for example with the Ca-Al-(Ag,Au) magnetoresistance presented in 4.1.1). This behavior is expected since the quantum corrections to the conductivity theories predict $\frac{\Delta\rho}{\rho} \propto \rho$. The magnetoresistance is positive over the whole range of temperature and field reflecting a large spin-orbit scattering field. As the temperature increases its magnitude is reduced due to the destruction of phase-coherence by inelastic scattering events, in the same way as in amorphous metals. Before we describe the fitting procedure we should mention that no negative magnetoresistance was observed in any of the samples at any temperature considered here, in contrast to the data of reference [52] where a negative magnetoresistance is reported in $Al_{63}Cu_{25}Fe_{12}$ at 30 K. Apart from this our data are in very good agreement with that of other groups [44, 52, 53, 82].

4.2.2 Fitting procedure

The data are fitted to the predictions of weak localization and enhanced electron-electron interaction as given in Chapter 2. As a first step, the fitting is restricted to low fields ($B/T \leq 1\text{T.K}^{-1}$) [6] with the resistivity ρ, the dephasing field B_ϕ and the spin-orbit scattering field B_{so} as free parameters using only the weak localization expression (Eq. 2.14), enhanced electron-electron interaction contribution being important only at high fields. B_{so} is temperature independent. Using ρ as a free parameter in the weak localization expression allows us to determine the resistivity in a way which is independent of the sample geometry and microcracks that might exist in these very brittle samples. A similar procedure was first used by Baxter *et al.* to measure the

[6] To obtain consistent parameter values the fitting range is slightly larger than that for Ca-Al-(Ag,Au) samples. This is because the magnetoresistance in the present case is always positive and relatively featureless. Note that the enhanced electron-electron interaction contribution is still negligible (see Figure 2.11).

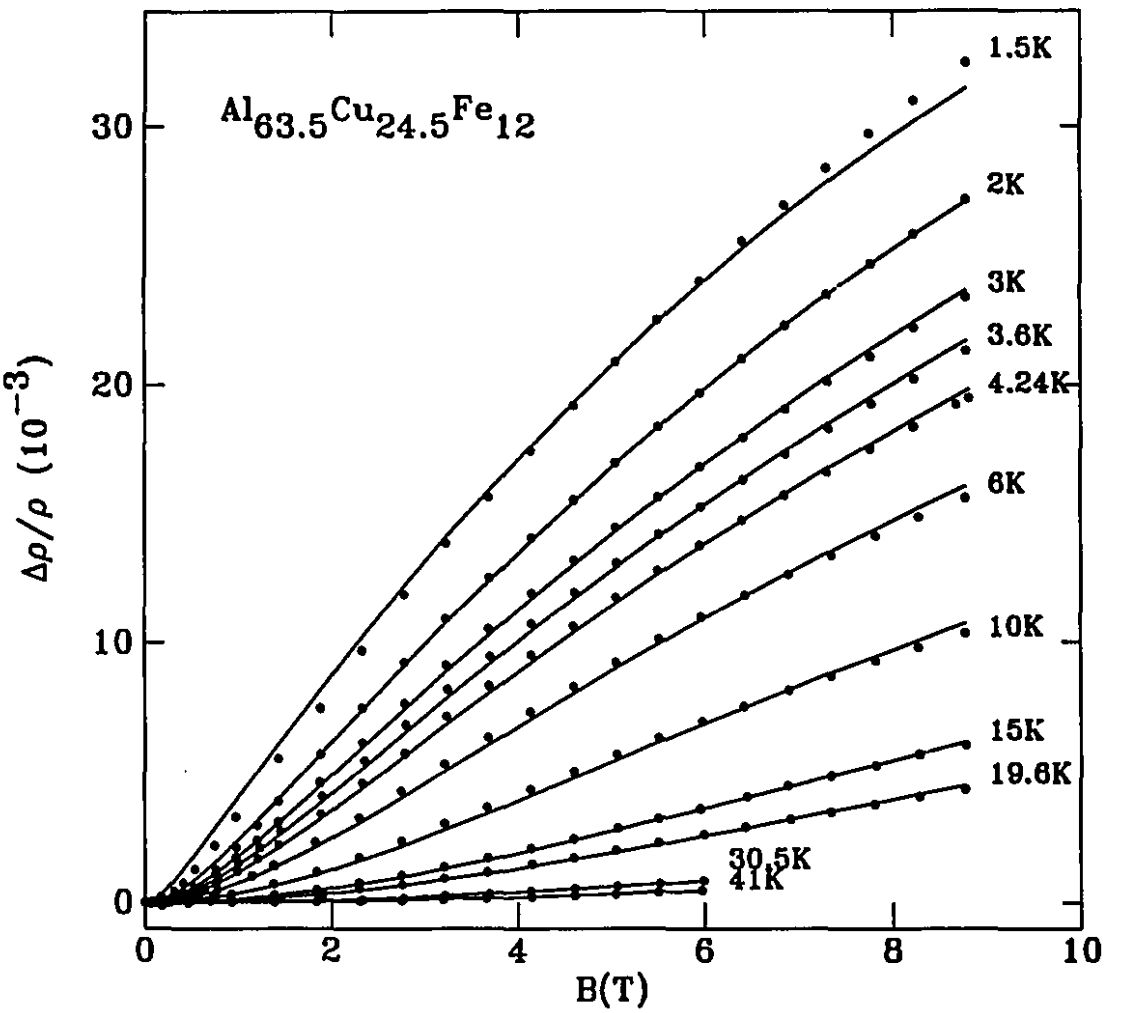

Figure 4.27: Normalized magnetoresistance of $Al_{63.5}Cu_{24.5}Fe_{12}$. The points are the experimental data, the solid line the fitted magnetoresistance (Eq. 2.14 and 2.29). Temperatures are indicated in the figure.

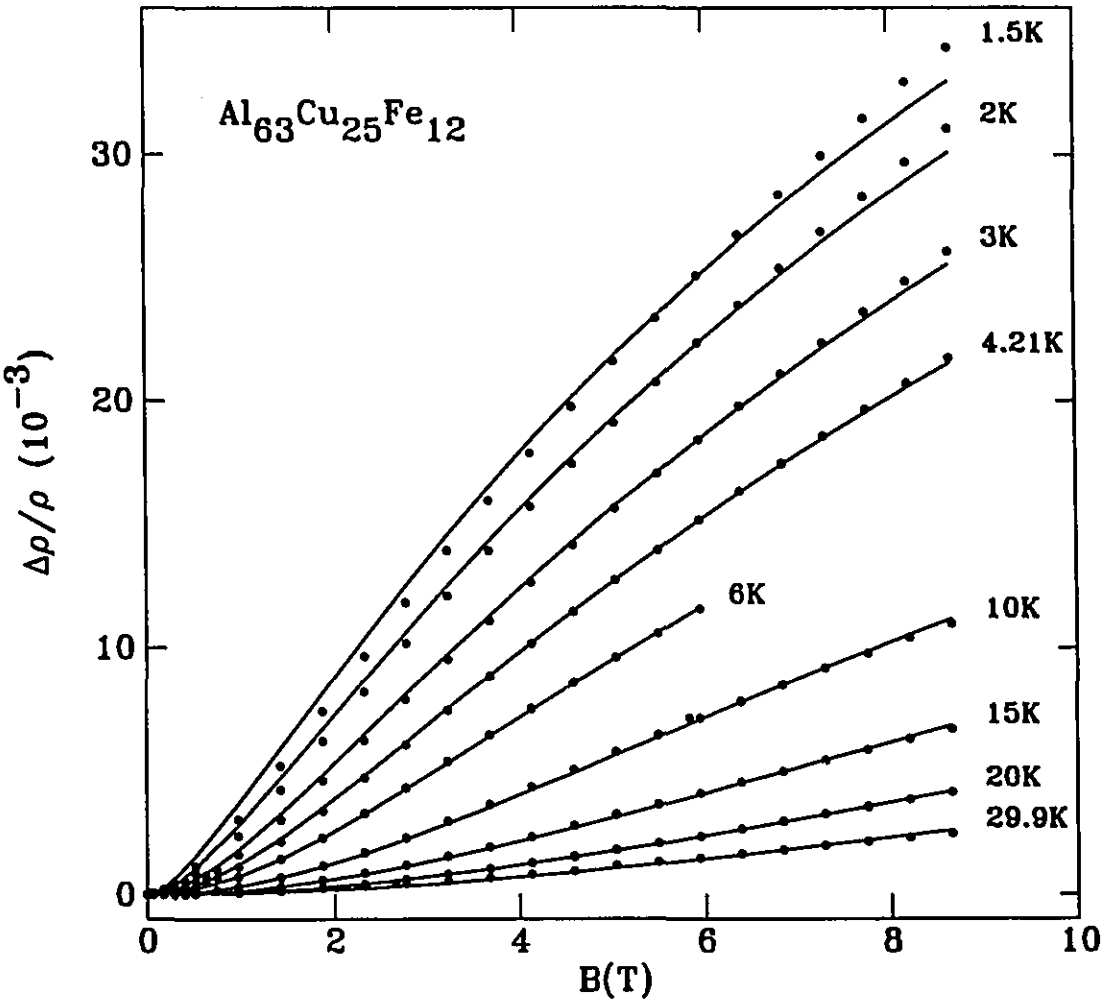

Figure 4.28: Normalized magnetoresistance of $Al_{63}Cu_{25}Fe_{12}$. The points are the experimental data, the solid line the fitted magnetoresistance (Eq. 2.14 and 2.29). Temperatures are indicated in the figure.

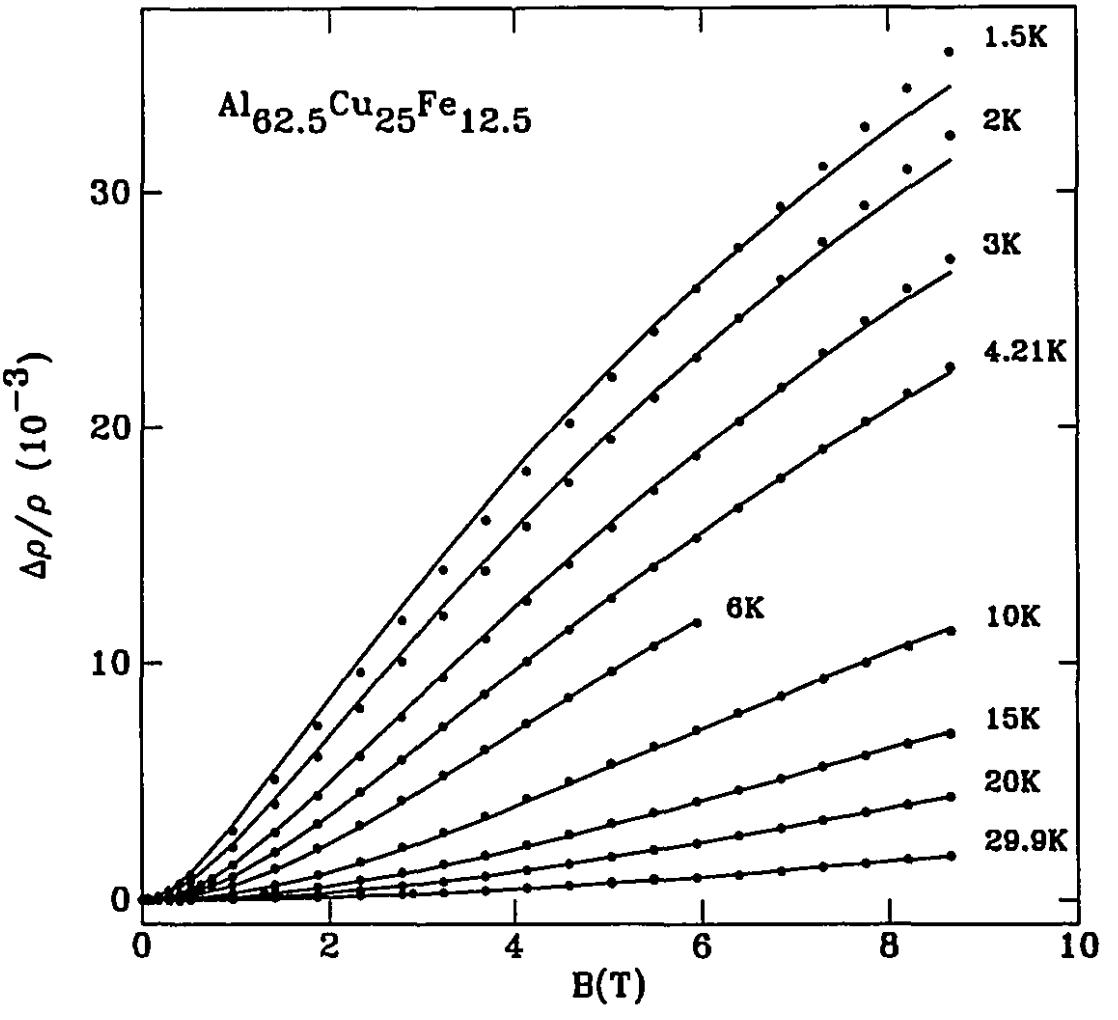

Figure 4.29: Normalized magnetoresistance of $Al_{62.5}Cu_{25.5}Fe_{12}$. The points are the experimental data, the solid line the fitted magnetoresistance (Eq. 2.14 and 2.29). Temperatures are indicated in the figure.

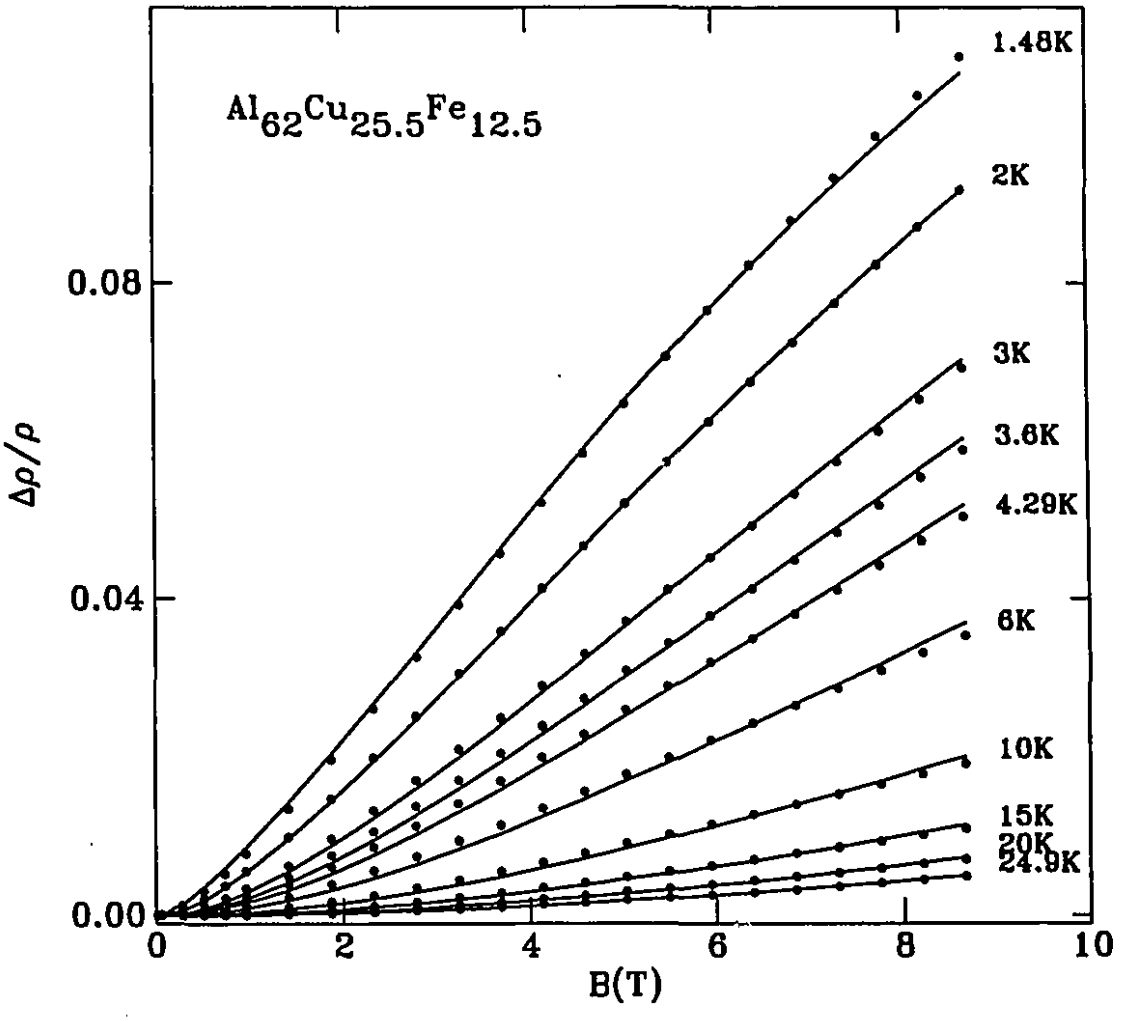

Figure 4.30: Normalized magnetoresistance of $Al_{62}Cu_{25.5}Fe_{12.5}$. The points are the experimental data, the solid line the fitted magnetoresistance (eq. 2.14 and 2.29). Temperatures are indicated in the figure.

resistivity of Al-Mg-Si quasicrystals [50].

The fitting is then extended to the entire field range, including the enhanced electron-electron interaction (diffusion channel) term with the screened Coulomb interaction constant $\tilde{F}_\sigma$ as the only variable. Thus, as for Ca-Al-(Ag,Au) system, each family of curves in Figures 4.27-30 is fitted with common values of $\tilde{F}_\sigma$ and B_{so} and one value of B_ϕ at each temperature. The results of the the fitting are given in Table 4.2.

It may be seen from the figures that agreement between the data and quantum corrections to the conductivity theories is very good over the entire range of field and temperature. In all cases, the enhanced electron-electron interaction contribution is important at high fields and even exceeds that of weak localization in $Al_{62}Cu_{25.5}Fe_{12.5}$ at low temperatures, in contrast to amorphous alloys (section 4.1) and thin films [6, 7, 10] where the magnetoresistance is always dominated by the weak localization contribution. A similar observation, though to a lesser degree, has also been reported by Chui *et al.* [108] in high resistivity granular Al films close to the metal-insulator transition [109]. This is consistent with the increasing role of the interaction effects when the resistivity becomes very large [108, 110]. The contribution is positive and comes from the diffusion channel only. The Cooper channel contribution is even smaller here and was neglected.

The values of the resistivity obtained from the fits at low temperatures are consistent with the measurements made at room temperature with the conventional four terminal measurements, as explained in section 3.2. Furthermore our values are in excellent agreement with the values reported by Biggs *et al.* [43] and Klein *et al.* [44, 52, 53]. The spin-orbit scattering field is found to be about 11 T ($1/\tau_{so} \sim 1.4 \times 10^{12} s^{-1}$) and is the same in all the samples. This was expected since their chemical compositions are very close. The fact that only $1/\tau_{so}$ remain constant while the other parameters vary (see Table 4.2) reinforces strongly our fitting procedure. It is worth noting that because of the large value of B_{so} it is not possible to see a maximum in the magnetoresistance which is normally seen when $B \geq B_{so}$. This

maximum is further delayed by the large positive enhanced electron-electron interaction contribution at high fields, as mentioned earlier and supported by the results of Klein *et al.* [52, 53] where they only observed a slight decrease in the slope of the magnetoresistance up to 35 T.

At this stage a remark about the use of weak localization and enhanced electron-electron interaction theories for this system is in order. Weak localization and electron-electron interaction expressions are first order terms in the disorder parameter $(k_F l_e)^{-1}$ of a perturbation treatment of the disorder and should be used, in principle, only when $(k_F l_e)^{-1} \ll 1$. The estimation, based on the free electron like formula (Eq. 2.38), of $(k_F l_e)^{-1}$ for the present alloys gives a value ~ 1.5. It is clear if that approach is valid the electron mean free path l_e will be much less than the interatomic distance. Using the value of $k_F = 1.52\text{Å}^{-1}$, obtained from the positions of the strongest peaks in the X-ray diffraction pattern (see appendix B) , one finds $l_e \approx 0.4\text{Å}$; less than the Bohr radius!. This unphysically low value of l_e definitely casts in doubt the free-electron approach. According to Poon [41] the electron effective mass in this systems is enhanced and therefore the disorder parameter, given in this case by:

$$(k_F l_e)^{-1} \approx 1.5 \left(\frac{m}{m_t^*}\right), \tag{4.5}$$

where $m_t^* = \hbar k_F/(\partial E/\partial k)_F$ is the tangential effective mass and m the free electron mass, can still be much less than unity. However by no means this implies that icosahedral Al-Cu-Fe alloys are ordered. Assuming a factor ten for the mass enhancement gives a mean free path of about 5Å which is much less than that of, for example, amorphous $Ca_{70}Mg_{30}$ [18] and still represents a high degree of disorder. The fact that l_e is short is consistent with the success of quantum corrections to the conductivity theories in describing the magnetoresistance as demonstrated above. Therefore, in conclusion, we have two indications of the disorder-induced nature of the low temperature electronic transport properties in icosahedral Al-Cu-Fe system: the short electron mean free path and the good agreement between the predictions of weak localization and enhanced electron-electron theories and the magnetoresistance data.

4.2.3 The dephasing rate $1/\tau_\phi$

The temperature dependence of the dephasing rate as deduced from the magnetoresistance analysis is shown in Figure 4.31. It may be described by an expression of the form:

$$\frac{1}{\tau_\phi} = AT^p. \tag{4.6}$$

In all samples, a best fit is obtained for $p \sim 1.5$ and $A \approx 1-2\times10^{10}\mathrm{s}^{-1}/\mathrm{K}^{3/2}$. Similar results have also been found by Haberkern *et al.* [82] in their magnetoresistance study of this alloy system. It is well known [3, 4, 62] that an exponent $\frac{3}{2}$ is expected for electron-electron scattering in the so-called dirty limit when $(k_F l_e)^{-1} > 1$. Moreover, the value $p = \frac{3}{2}$ is consistent with the theoretical expression of the dephasing rate due to electron-electron scattering given by equation (2.21). Note that this value of p is a further evidence of the presence of disorder in icosahedral Al-Cu-Fe alloys.

For a quantitative comparison of the data to the theory, (Eq. 2.21), we use the value of $(k_F l_e)^{-1}$ given above and take $E_F \sim 1\mathrm{eV}$ for the Fermi energy. Eq. (2.21) then yields:

$$\frac{1}{\tau_{ee}} = 4.4\times10^6 T^2 + 2\times10^9 T^{3/2}\mathrm{s}^{-1}. \tag{4.7}$$

Although the calculated value is about a factor five smaller than the one we find from the fits, it is consistent with the fact that the $T^{3/2}$ term dominates. The first term is expected to dominate when the disorder is not too strong. The difference in the magnitude between the estimated $1/\tau_\phi$ and the experimental one is not specific to the present case. The same problem has been encountered in several other systems where the theoretical expression of $1/\tau_{ee}$ always underestimates the observed dephasing rate (see Altshuler and Aronov [4], for example). The origin of the discrepancy is not understood and remains to be investigated. In summary, we conclude that dephasing is due to electron-electron scattering, in the strong disorder limit and that the electron-electron scattering rate expression, Eq. (2.21), needs to be reevaluated so that quantitative comparison with the experiment can be made.

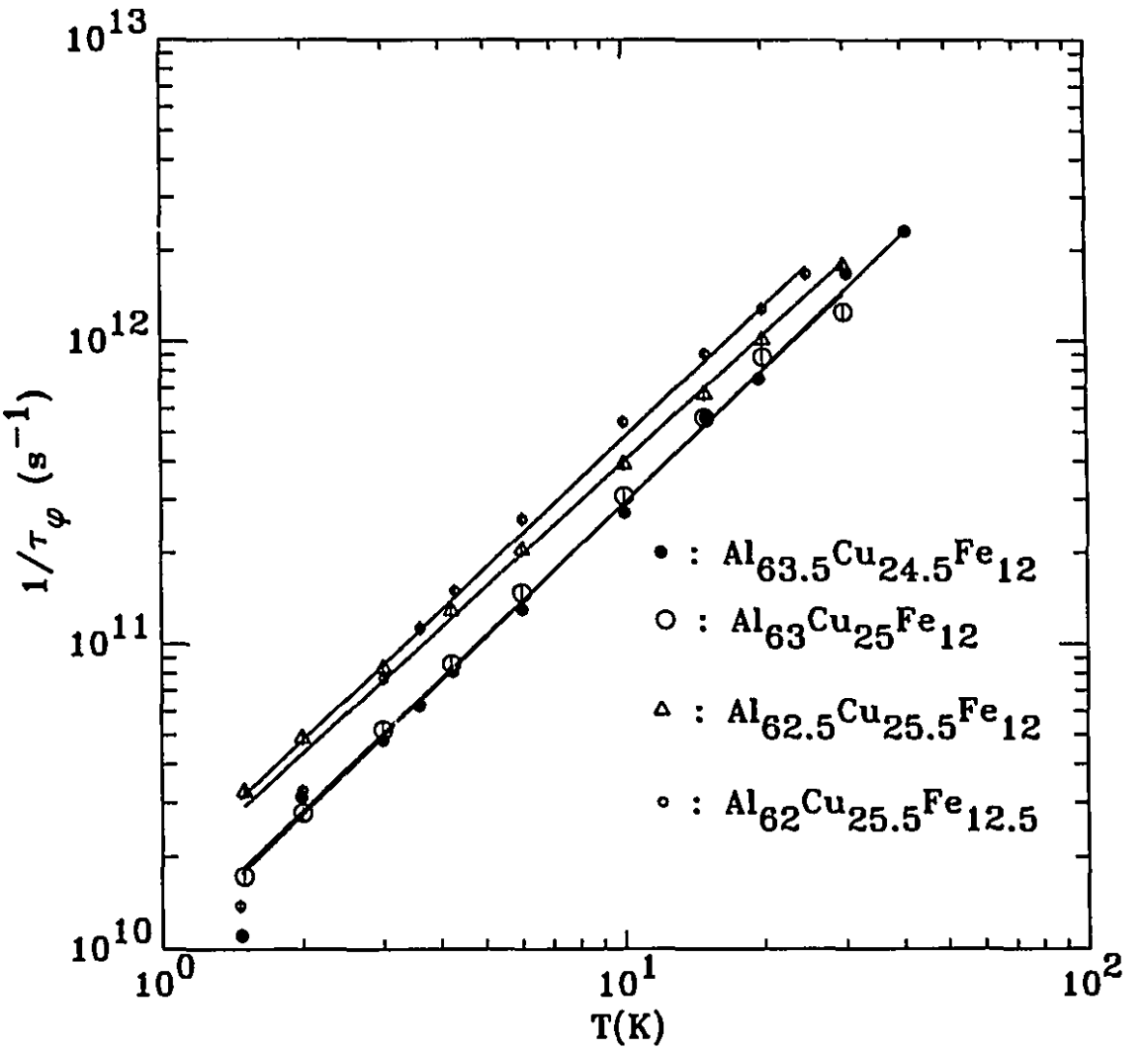

Figure 4.31: The dephasing rate, $1/\tau_\phi$, in icosahedral Al-Cu-Fe alloys as a function of temperature. The solid line is a fit as described in the text.

Alloy	$1/\tau_{so}(ps^{-1})$	$\tilde{F}_\sigma^a$	$\tilde{F}_\sigma^b$	$1/\tau_\phi(s^{-1})^a$	$1/\tau_\phi(s^{-1})^b$	$\rho(\mu\Omega.cm)$
$Al_{63.5}Cu_{24.5}Fe_{12}$	1.4	0.25	0.56	$9.9 \times 10^9 T^{1.47}$	$8.4 \times 10^8 T^2$	4500
$Al_{63}Cu_{25}Fe_{12}$	1.4	0.2	0.60	$1.0 \times 10^{10} T^{1.45}$	$8.6 \times 10^8 T^2$	5300
$Al_{62.5}Cu_{25.5}Fe_{12}$	1.4	0.1	0.64	$1.7 \times 10^{10} T^{1.38}$	$9.7 \times 10^8 T^2$	7000
$Al_{62}Cu_{25.5}Fe_{12.5}$	1.4	1.06	1.08	$1.8 \times 10^{10} T^{1.43}$	$2.0 \times 10^{10} T^{1.34}$	10000

Table 4.2: Least-squares fitting parameters of icosahedral Al-Cu-Fe alloys. Errors: τ_{so}, τ_ϕ,$\pm$10%.
[a]From the magnetoresistance.
[b]From the temperature dependence of the resistivity.

4.2.4 The interaction constant $\tilde{F}_\sigma$

The values of the interaction constant, $\tilde{F}_\sigma$, for the different Al-Cu-Fe alloys are listed in Table 4.2. Except in the most resistive alloy, these values compare well with those found in amorphous metals. They range from 0.1 to 0.65. In $Al_{62}Cu_{25.5}Fe_{12.5}$ the best fit is obtained for $\tilde{F}_\sigma = 1.06 \pm 0.3$ corresponding to a value of $F = 1.15$, F being the average of the screened Coulomb potential defined in Eq. (2.27). The large value of F may be an indication of the breakdown of the Thomas-Fermi theory when the density of electrons is very low as is the case in these alloys. In fact, as pointed out in section 2.4, measurements of the Hall coefficient revealed that the density of electrons is only $6.3 \times 10^{20} cm^{-3}$ in $Al_{63.5}Cu_{24.5}Fe_{12}$ and may be even less in $Al_{62}Cu_{25.5}Fe_{12.5}$. In such a situation the screening deteriorates rapidly and the screening length tends to diverge [110]. Another possibility for the large F may be band structure effects, as suggested by Klein *et al.* [53] and Thomas *al.* [111]. The suggestion is well justified since all the phenomena we consider here are the result of the electron diffusion which depends critically on the band structure of the system. If the conduction band contains, for example, n equivalent valleys, the constant F should be replaced by $(2n - 1/2)F$ [4]. As an illustration, in Si where $n = 2$, F is multiplied by a factor $\frac{7}{2}$. In the present case there is no detailed information on the band structure to test this approach.

4.2.5 Temperature dependence of the resistivity

Figure 4.32.a shows the measurement of the temperature dependence of the resistivity in the temperature range from 1.5 to 300 K. We see that the behavior of the resistivity depends strongly on alloy composition. In $Al_{63.5}Cu_{24.5}Fe_{12}$, ρ increases by only 67% between room temperature and 1.5 K whereas in $Al_{62}Cu_{25.5}Fe_{12.5}$ it increases by almost 225% in the same temperature range. Furthermore in this alloy a maximum in the resistivity is observed at low temperatures. These results are also in excellent agreement with those reported in references [43, 52, 53].

The temperature dependence of the zero-field conductivity change between 150 mK and 30 K is shown in Figure 4.32.b. In all samples, the resistivity increases as the temperature is lowered except in $Al_{62}Cu_{25.5}Fe_{12.5}$ where after reaching a maximum around 14 K it decreases down to the lowest temperatures. As for the magnetoresistance, the data are analyzed within the quantum corrections to the conductivity theories using Eqs. (2.19) and (2.33). In contrast to amorphous Ca-Al-(Ag,Au) system, the weak localization contribution in this high resistivity system is important and must be included in the analysis (the dephasing rate $1/\tau_\phi$ does not saturate in the present case). Moreover, it increases with increasing resistivity and dominates in $Al_{62}Cu_{25.5}Fe_{12.5}$. The values of ρ and B_{so} are the same as those extracted from the magnetoresistance fits. However the dephasing field and the Coulomb interaction constant were allowed to vary in order to fit the data over a wide range of temperature. Here also good fits are found from the lowest temperatures to approximately 15 K. However although the dephasing rate $1/\tau_\phi$ is found to follow a power law AT^p, the value of p is equal to 2.0 ± 0.1 and the coefficient $A \sim 9 \times 10^8 K^{-2}.s^{-1}$, in the low resistivity samples. Similar values of A and p were reported by Klein and coworkers [44, 52]. The present results are significantly different from the findings from the magnetoresistance analysis. They suggest perhaps that only the first term of the electron-electron scattering rate (Eq. (2.21)) is relevant to the temperature dependence of the resistivity in the relatively low resistivity samples. On the other hand, according to Takayama's expression for inelastic electron-phonon scattering [61] (Eq.

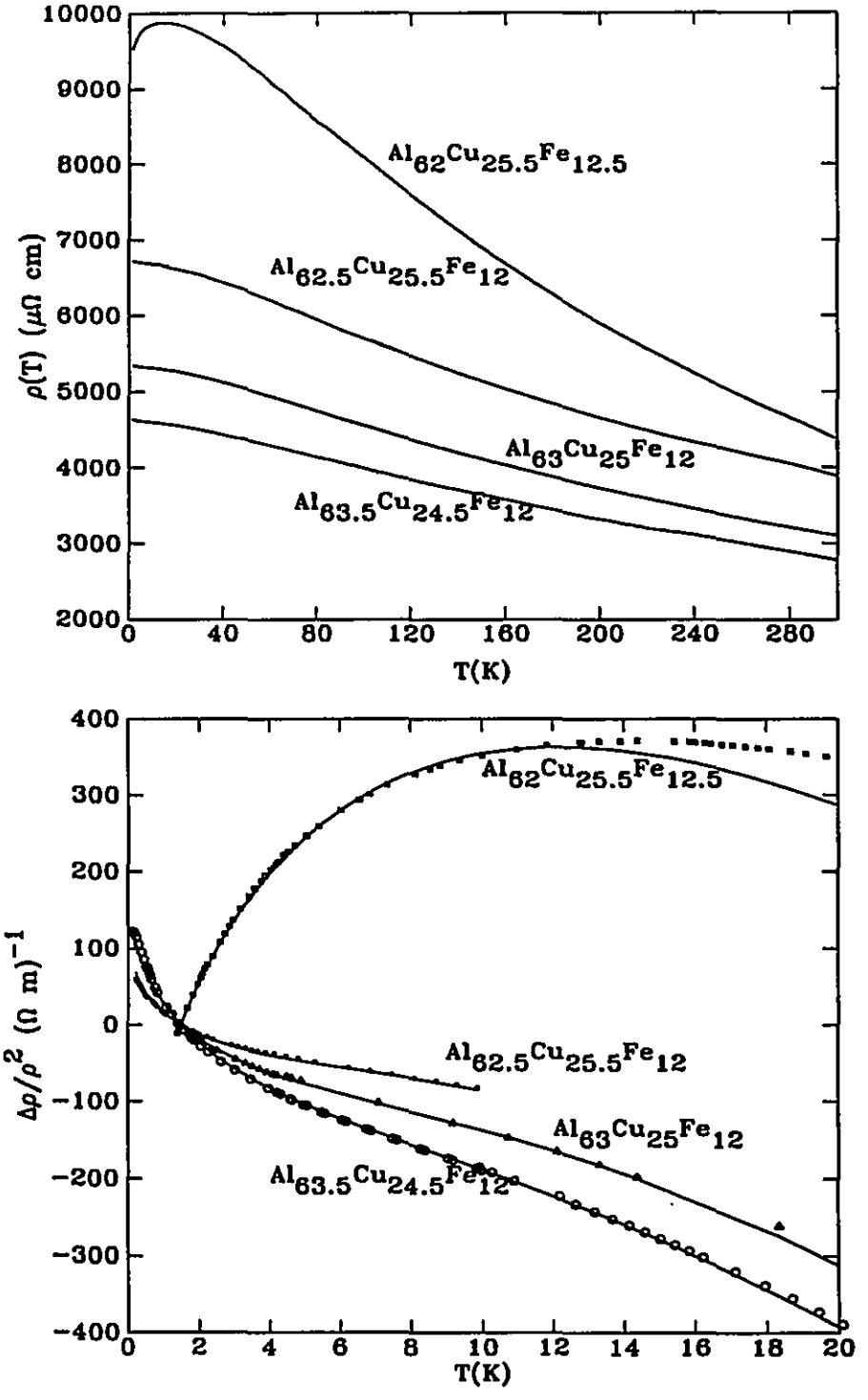

Figure 4.32: Resistivity of icosahedral Al-Cu-Fe alloys as a function of temperature. The solid line in (b) are fits to the data using quantum corrections to the conductivity expressions (Eqs. (2.19) and (2.33).

(2.20)) and to Chakravarty and Schmid [5], a value of $p = 2$ can also be attributed to electron-phonon scattering. If the former alternative is valid it opens the question of whether the magnetoresistance is more sensitive to intense electron scattering (disorder) than the temperature dependence of the resistivity. In fact as mentioned in subsection 2.1.2, the $T^{3/2}$ term in the electron-electron scattering rate is expected to dominate in the strong disorder limit whereas the T^2 should dominate in the weak disorder limit. Our conjecture is supported by the results of the most resistive alloy (with highest disorder), i.e. $Al_{62}Cu_{25.5}Fe_{12.5}$, where both the magnetoresistance and the temperature dependence of the resistivity give, within error, the same $1/\tau_\phi \propto T^{1.5}$. It is still not clear why the temperature dependence of the resistivity seems to be less sensitive to disorder and further investigation is needed to explain the origin of the discrepancy in the value of p for the other samples. But the discrepancy underscores the importance of our approach in analyzing the experimental data. A full picture of the dephasing rate can only be obtained by considering both the magnetic field and temperature dependence of the resistivity.

The low-temperature dependence of the resistivity of $Al_{62}Cu_{25.5}Fe_{12.5}$ deserves special attention and is shown in Figure 4.33 at different constant magnetic fields. The maximum in the resistivity around 14 K was not expected. Such behavior is only seen in highly doped semiconductors (eg. Si:P and Ge:Sb) [111, 112, 113]. Note that our data are in excellent agreement with that reported by Klein *et al.* in their most recent work on this system [53]. They attributed this peculiar behavior of the resistivity to a band structure effect in this very high resistivity alloy. Here we show that it is consistent with weak anti-localization effects caused by spin-orbit scattering discussed in section 2.1 (see also Figure 2.8). A change in the slope of the resistivity occurs for $1/\tau_\phi \geq \frac{1}{6}1/\tau_{so}$ as the dephasing becomes more important at high temperatures. It is worth noting that for the other three Al-Cu-Fe samples considered here, it is not possible to see such an effect because as deduced from the fitting $B_\phi \ll B_{so}$. Another way to destroy anti-localization effect on the resistivity is by applying a magnetic field. One can see from the figure that as the field increases the negative slope of the

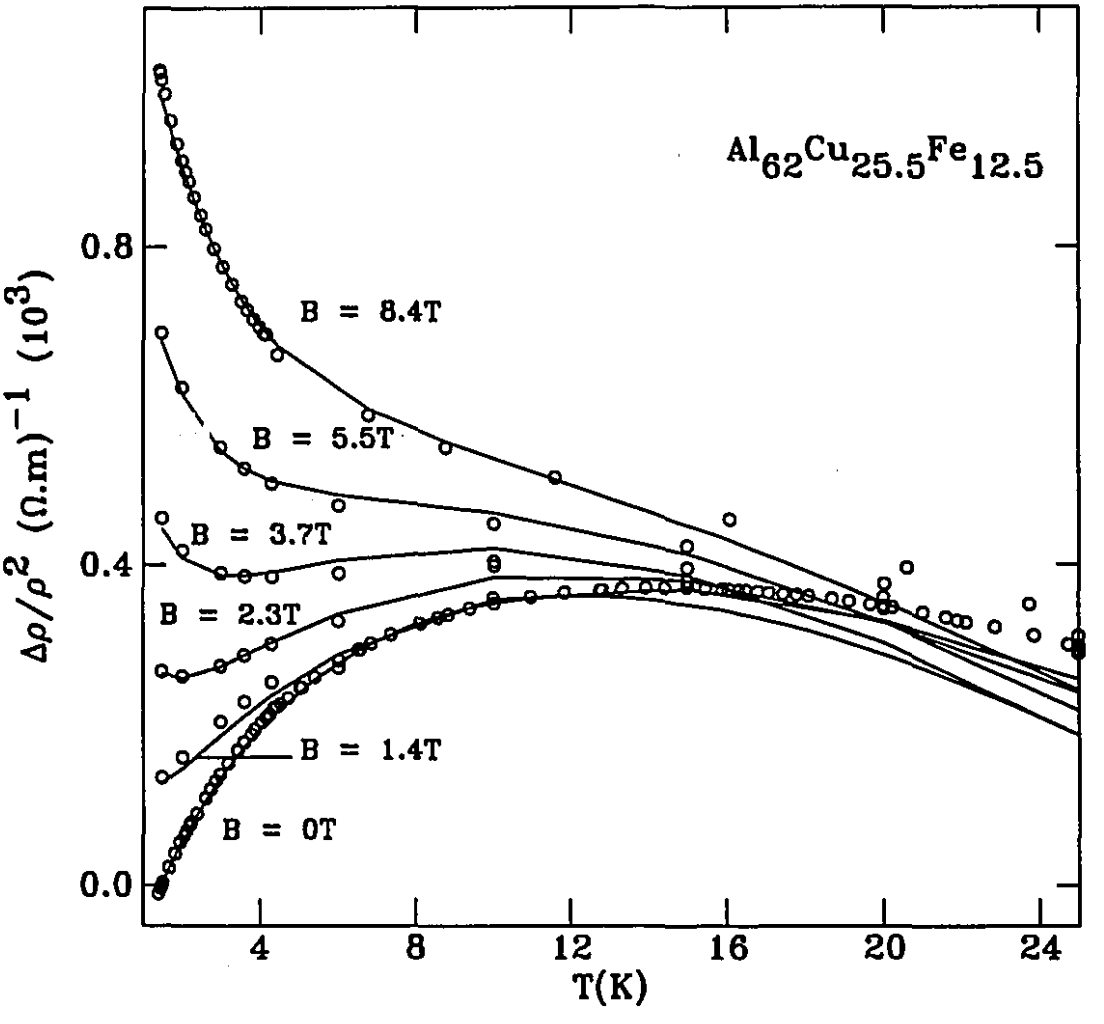

Figure 4.33: Low-temperature resistivity of icosahedral $Al_{62}Cu_{25.5}Fe_{12.5}$ alloy as a function of temperature in different magnetic fields. The solid line is a fit as described in the text.

resistivity with temperature is progressively recovered. We also note that even a field as high as 8.4 T is not sufficient to suppress (saturate) the temperature dependence of the weak localization contribution to the resistivity. The solid lines in Figure 4.33 are therefore the result of a combination of weak localization and enhanced electron-electron interaction (diffusion channel) using the full theoretical expressions with the same parameters as those extracted from the magnetoresistance analysis and are therefore zero parameter fits to the data. Since $\tilde{F}_\sigma = 1.08$, the diffusion channel contribution to the resistivity in the absence of the field is positive in this sample in contrast with the other samples of lower resistivity where it is negative. A similar sign change of the diffusion channel contribution has also been observed by Klein *et al.* [53] in this alloy system and by Thomas *et al.* [111] and Rosenbaum *et al.* [112] in doped Ge:Sb and Si:P, respectively, as a function of dopant concentration just above the metal-insulator transition [109]. This observation with the large effect of electron-electron interaction as found above suggests that $Al_{62}Cu_{25.5}Fe_{12.5}$ is also very close to the transition.

4.2.6 Summary

Throughout this section we have used weak localization and enhanced electron-electron to analyze the low temperature resistivity and magnetoresistance of icosahedral Al-Cu-Fe alloys. The agreement between the data and theory is more than satisfactory. By itself, this is a strong indication for the presence of disorder in this system. Moreover, our estimate of the electron mean free path, based on realistic parameters, places icosahedral Al-Cu-Fe among the most disordered alloys. The temperature exponent of the dephasing rate ($p = 3/2$) is another indication of the high degree of disorder in this alloy system.

However, it is important to underline that disorder alone cannot fully explain the resistivity behavior observed in these alloys. The rapid variation of the resistivity with composition, the reduced density of states are all in favor of the existence of a pseudogap in the density of states at the Fermi level. But here also a pseudogap at

the Fermi level is not sufficient to account for the low temperature dependence of the resistivity on magnetic field and temperature. However the two scenarios, disorder and band structure effects complement each other nicely. Therefore, we are led to the conclusion that the transport properties of icosahedral Al-Cu-Fe are intimately related to both disorder and band structure effects.

Chapter 5

Conclusion

We have presented in this thesis measurements of the magnetoresistance and the temperature dependence of the resistivity in two different systems, namely amorphous Ca-Al-(Ag,Au) alloys and icosahedral Al-Cu-Fe alloys. Our main achievements are, in the former the influence of spin-orbit scattering was, through a systematic study, quantitatively demonstrated for the first time on the electron-electron interaction contributions to the magnetoresistance, a question that has been long overlooked. In icosahedral Al-Cu-Fe we presented the first detailed and complete analysis of the low temperature resistivity and magnetoresistance data in terms of weak localization and enhanced electron-electron interactions theories.

From the results of Ca-Al-(Ag,Au), we have been able to show that weak localization theory is not restricted to weak spin-orbit scattering systems only; it provides an accurate description of the magnetic field and temperature dependences of the resistivity over a wide range of spin-orbit scattering rate; from very small to very large, as well. On the other hand, the diffusion channel contribution to the magnetoresistance was found to be very sensitive to spin-orbit scattering. It decreases rapidly with increasing spin-orbit scattering and is totally removed in the extremely high spin-orbit scattering regime ($1/\tau_{so} \geq 10^{13}\mathrm{s}^{-1}$).

The dephasing and spin-orbit rates were extracted from the low field comparison of the weak localization theory and the experimental data. In this system, the dephasing

rate has a universal behavior in all samples and is controlled by inelastic electron-phonon scattering and varies as T^3 at high temperatures ($T > 5$K). The saturation at lower temperatures ($T \leq 4.2K$) is due to magnetic impurity scattering.

The spin-orbit scattering rate is found to increase linearly with Ag and Au concentrations up to 3% at. of Au. The rate of increase is much larger for Au than for Ag, as expected from the spin-orbit interaction dependence on the atomic number. The hydrogen-like orbital picture, though very simplistic, is found to give a good estimate of the ratio of the two slopes.

Furthermore, we have also shown that in its actual form, the expression for the temperature dependence of the resistivity from the diffusion channel, though it gives the exact dependence on the temperature, cannot account for the observed magnitude of the resistivity change in high spin-orbit scattering alloys unless unphysical values of the screening parameter are assumed.

In icosahedral Al-Cu-Fe we also found good agreement between the experimental data and the theories of quantum corrections to the conductivity. But in contrast to the amorphous system, it was necessary to treat weak localization and enhanced electron-electron interactions contributions on an equal footing in order to account for the magnetoresistance and the resistivity temperature dependence. The analysis allows us to correlate strongly the low temperature behavior to the presence of disorder.

However in spite of the good agreement, discrepancies were found in the magnitude and temperature dependence of the dephasing rate. As deduced from the magnetoresistance $1/\tau_\phi \propto T^p$ with $p = \frac{3}{2}$, a characteristic of electron-electron scattering in the strong disorder limit. The zero-field data on the other hand suggest that dephasing is due to electron-phonon or electron-electron scattering in the weak disorder limit ($p = 2$). This is not due to a weakness in our approach, which separately give results consistent with that of other groups, but rather to a genuine physical phenomenon: the relevance of the degree of disorder to the magnetoresistance and the temperature dependence of the resistivity.

In one of the samples, $Al_{62}Cu_{25.5}Fe_{12.5}$ weak anti localization was directly observed and was nicely accounted for by the theory. Furthermore, a sign change in the diffusion channel contribution to the zero-field resistivity in this sample was found and is attributed to the proximity of the metal-insulator transition in similarity with highly doped semiconductor.

Although substantial progress has been made through this work for a complete understanding of the electronic transport properties in disordered conductors, there are still many open questions that remain to be answered.

On the theoretical side, the effect of spin-orbit scattering on the electron-electron interactions should be investigated in detail. Specifically, the corrections to the resistivity and magnetoresistance from the diffusion channel have to be rederived taking explicitly into account the spin-orbit interaction. The results presented in this thesis may serve as a guide in testing the models proposed. Another important point that also deserves particular attention is the discrepancy observed in the temperature exponent of Al-Cu-Fe; our results need to be put on a solid theoretical ground.

On the experimental side, it will be very useful in the future to complement the magnetoresistance measurements in icosahedral Al-Cu-Fe alloys presented here, by a systematic investigation of the Hall effect in this alloy system. To date all measurements of the Hall coefficient report negative values whereas in a situation where the Fermi surface is believed to interact strongly with the boundaries of the Brillouin zone, one could expect at least some samples with a positive value due to unfilled hole states. The presence of a pseudogap in the density of states at the Fermi level will then be put on a firm ground as the sign change will indicate a sign change in the slope of the density of states with respect to the energy. The crossover is expected to occur in the alloy where the Fermi sphere perfectly matches the first Brillouin zone. Furthermore, these measurements will also allow an independent investigation of the enhanced electron-electron interaction contribution to the magnetoresistance. This is possible because weak localization does not contribute to the Hall effect and the correction to the Hall coefficient comes from enhanced electron-electron interaction

only.

Finally, a full answer to the question of whether Al-Cu-Fe is ordered or disordered remains to be given. The success of quantum corrections to the conductivity in describing the magnetotransport properties at low temperatures implies immediately very intense scattering of the electrons at the Fermi level. Even if band structure effects are important and can explain some of the electronic properties, our estimate of the electron mean free path corresponds to extremely high disorder and compares with that of the most resistive amorphous metals. It will be of great interest in the future to reconcile this with the high degree of atomic order displayed in electron transmission images through models that take into account the specificity of the quasiperiodic structure.

Appendix A

The functions f_3 and g_3

A.1 Weak localization function f_3

The magnetoresistance associated with weak localization as given by Fukuyama and Hoshino [54], Eq. (2.14) and Altshuler *et al.* [4], Eq. (2.18) involves the function f_3 which can be expressed as an infinite series [60]:

$$f_3(x) = \sum_{n=0}^{\infty} a_n(x) \tag{A.1}$$

with

$$a_n(x) = 2(\sqrt{n+1+x} - \sqrt{n+x}) - \frac{1}{\sqrt{n+1/2+x}} \tag{A.2}$$

This series converges very slowly. For large n, the terms fall off only as $n^{-3/2}$. This is so slow that one needs to sum more 10^5 terms to achieve an accuracy better than 1% [23]. To avoid doing so compact formulas from which f_3 can be computed efficiently were given by several authors. Ousset and coworkers [114] were the first to provide an approximation the the function based on an Euler-Maclaurin expansion of the series. However although it represents a great improvement over summing the series directly it is somewhat cumbersome. A more compact and efficient expression, which is used for analysing the data in this thesis, has been recently provided by Baxter *et al.* [88]. This was done by explicitly summing the first two terms of the series. The remaining terms (denoted as $R(x)$) being treated as an integral from 3/2 to infinity with the

intergrand rewritten as a rapidly convergent Taylor series. More explicitly, $f_3(x)$ can be written as:

$$f_3(x) = 2\left(\sqrt{2+\frac{1}{x}}+\sqrt{\frac{1}{x}}\right) - \left(\frac{1}{\sqrt{1/2+1/x}} - \frac{1}{\sqrt{3/2+1/x}}\right) + R(x), \qquad (A.3)$$

with the remainder,

$$R(x) \approx \frac{(2.5+1/x)^{-3/2}}{48} + \frac{(2.5+1/x)^{-7/2}}{1024} + \cdots. \qquad (A.4)$$

The accuracy of the above expression is better than 0.1% by only including the first term of $R(x)$. Moreover if the lower limit in the integral used to compute $R(x)$ is set to 1.53 the correct asymptotic limit, i.e. $f_3(x \rightarrow \infty) = 0.6049$, is retained [88].

Note that this expression can also be extended to the case where $\gamma > 1$ in Eq. 2.14 at large magnetic fields. In fact no discontinuity is observed at $\gamma = 1$ and Eq. (2.14) falls onto Eq. (2.18) for large diffusion constant as was shown in Figure 4.1.

A.2 The diffusion channel function g_3

The diffusion channel contribution to the magnetoresistance, Eq. (2.29), is proportional to function $g_3(x)$. This function has defined by [3]:

$$g_3(x) = \int_0^\infty \frac{d^2}{d\omega^2}(\omega N(\omega)\left\{\sqrt{\omega+x}+\sqrt{|\,\omega-x\,|}-2\sqrt{\omega}\right\} \qquad (A.5)$$

Where $N(\omega) = 1/(exp(\omega)-1)$. $g_3(x)$ has the limiting behaviors:

$$g_3(x) = \begin{cases} 0.056x^2 & x \ll 1 \\ \sqrt{x} - 1.294 & x \gg 1 \end{cases}$$

An approximation to the function $g_3(x)$, for other values of x, has also been given by Ousset *et al.* [114] which was used in this thesis. It is accurate to better than 0.25%. For $x < 3$ Ousset and coworkers have evaluated numerically the integral in Eq. (A.5) and fitted the result to a polynomial expression. They found:

$$\begin{aligned} g_3 x \approx\ & 5.6464 \times 10^{-2}x^2 - 1.4759 \times 10^{-3}x^4 + \\ & 4.2747 \times 10^{-5}x^{-6} - 1.5351 \times 10^{-6}x^8 + 6 \times 10^{-8}x^{10}\ . \end{aligned}$$

For large x, they expanded the square roots in the integrand in terms of ω/x and evaluated the resulting series. This gives for $x \geq 8$:

$$g_3(x) \approx \sqrt{x} - 1.2942 - \frac{\pi^2}{12x^{3/2}} - \frac{\pi^4}{16x^{7/2}} - \frac{5\pi^6}{32x^{11/2}}$$

In the intermediate range, $3 \leq x \leq 8$ with $u = x-4$, the authors fitted the numerically integrated function $g_3(x)$ to a polynomial in u and found:

$$\begin{aligned} g_3(x) \approx \; & 0.64548 + 0.235u - 7.45 \times 10^{-4}u^2 - 2.94 \\ & \times 10^{-3}u^3 + 6.32 \times 10^{-4}u^4 - 5.22 \times 10^{-5}u^5 \end{aligned}$$

The calculations by Ousset *et al.* [114] were later confirmed by Richter [83].

The least squares fitting algorithm used for fitting the theory to the experimental data presented in Chapter 4 is essentially the same the one employed by Richter [83] and is based on the procedures developed by Marquardt [115]. The kernel programs that call the routine contain the different magnetoresistance and temperature dependence of the resistivity expression as given in Chapter 2. Where it applies, the approximate expressions of $f_3(x)$ and $g_3(x)$ given above are used. Listing the programs here will only add 40 or more pages to the thesis and are therefore omitted.

Appendix B

Indexing of icosahedral quasicrystals

As mentioned in the introduction, quasicrystals belong to a new class of structures which is not accounted for by conventional crystallography, yet sharp diffraction peaks are observed in x-ray diffraction experiments. Indexing these peaks is an essential step in the identification of the quasicrystalline structure. Consequently, soon after the discovery of the first quasicrystaline alloy [34], several indexing schemes were developed to accomplish such a task. Here, we describe very briefly a "recipe", based on the method proposed by Cahn *et al.* [80], which was used to index the diffraction peaks in Figure 3.5. For further details, the reader is refered to the original article.

This method consists of assigning a set of integers, (N, M_0), to each diffraction peak such that the whole diffraction pattern can be consistently indexed. To do so, Cahn *et al.* [80] defined a vector $\vec{Q}_0$ in six-dimensional space such that its magnitude is given by:

$$Q_0^2 = N + \tau M_0, \tag{B.1}$$

where τ is the so-called golden mean; $\tau = 2\cos 36^\circ = (1+\sqrt{5})/2$ and $-N/\tau < M_0 < N\tau$.

The quantity Q_0^2 together with $Q_c^2 = \tau(N\tau - M_0)$ define the sequence of intense reflections. Q_c should inversely scale with the intensity.

N	M_0	Q_0^2	Q_c	q (Å^{-1})	2θ
6	9	20.56	1.07	1.68	23.8
7	11	24.80	0.72	1.85	26.2
8	12	27.42	1.24	1.94	27.6
11	16	36.90	1.71	2.25	32.1
14	21	47.98	1.64	2.63	37.6
18	29	64.92	0.45	2.98	43.0
20	32	71.78	0.76	3.14	45.3
27	43	96.57	1.05	3.64	53.1
38	61	136.70	0.89	4.33	64.2
40	64	143.55	1.08	4.43	65.9
52	84	187.91	0.47	5.07	77.0

Table B.1: The indices of the quasicrystalline x-ray diffraction peaks according to Cahn *et al.* scheme [80] ($\lambda = 1.5418$Å and $d_0 = 2.70$Å).

On the other hand, the three dimensional diffraction vector $\vec{q}$, defined as: $q = 4\pi \sin\theta/\lambda$; ($\lambda = 1.5418$Å), is given by:

$$q = \frac{Q}{d_0}, \tag{B.2}$$

d_0 is the quasilattice constant. Knowing, the position of the fundamental peak (most intense with smallest Q_c), Eq. B.2 allows one to determine the quasilattice constant d_0. Then using the relations between N and M_0, one can determine the indices of the remaining peaks. To illustrate this, consider the strong diffraction peak in Figure 3.5, at $2\theta = 45.3°$ which should correspond to the set $(N, M_0) = (20, 32)$. The value of the corresponding diffraction vector is equal to $q = 3.14$Å^{-1}. From this one obtains $d_0 = 2.70$Å for the quasilattice constant. Now, using this value of d_0 and the diffraction vector for each peak in the diffraction pattern, it is possible to determine the indices (N, M_0) through Eqs. B.1 and B.2. These are given above, in Table B.1.

Finally, we add a note on the correlation between the x-ray diffraction pattern and the electronic structure of quasicrystals which allows one to determine the Fermi wavevector k_F. According to Fujiwara the wavevector q of the strongest peaks and k_F always satisfy the condition [116]:

$$2k_F = q. \tag{B.3}$$

In the case of icosahedral Al-Cu-Fe studied here, the strongest peaks are (18,29) and (20,32) which correspond to $q_1 = 2.98\text{Å}^{-1}$ and $q_2 = 3.14\text{Å}^{-1}$, respectively. If we take $2k_F$ to be the mean of these values we obtain $k_F = 1.53\text{Å}^{-1}$. The same method was used by Burkov *et al.* [42] to calculate k_F and their value agrees very well with ours. The value of k_F will be used in our discussion of the disorder parameter in section 4.2.

References

[1] E. Abrahams, P. W. Anderson, D. C. Licciardello, and T. V. Ramakrishnan. *Phys. Rev. Lett.*, 42:673, 1979.

[2] D. J. Thouless. *Phys. Rep.*, 13:93, 1974.

[3] P. A. Lee and T. V. Ramakrishnan. *Rev. Mod. Phys.*, 57(2):287, 1985.

[4] B. L. Altshuler and A. G. Aronov. In A. L. Efros and M. Pollack, editors, *Electron-electron Interactions in Disordered Conductors*, volume 1, page 1, Amsterdam, 1985. North-Holland.

[5] S. Chakravarty and A. Schmid. *Phys. Rep.*, 104(4):193, 1986.

[6] G. Bergmann. *Phys. Rep.*, 107:1, 1984.

[7] G. Bergmann. *Z. Phys. B*, 48:5, 1982.

[8] B. L. Altshuler and A. G. Aronov. *Sov. Phys. JETP*, 50:968, 1979.

[9] J. M. Ziman. *Principles of the Theory of Solids.* Cambridge University Press, Cambridge, 1964.

[10] G. Bergmann. *Phys. Rev. Lett.*, 48:1046, 1982.

[11] G. Bergmann. *Phys. Rev. B*, 28:515, 1983.

[12] J. T. Masden and N. Giordano. *Phys. Rev. Lett.*, 49:819, 1982.

[13] P. Santhanam, S. Wind, and D. E. Prober. *Phys. Rev. Lett.*, 53:1179, 1984.

[14] S. J. Poon, E. J. Cotts, and K. M. Wong. *Solid State Commun.*, 52:519, 1984.

[15] J. Bieri, A. Fert, G. Creuzet, and A. Schuhl. *J. Phys. F*, 16:2099, 1986.

[16] J. C. Ousset, H. Rakoto, J. M. Broto, V. Dupuis, S. Askenazy, J. Durand, and G. Marchal. *Phys. Rev. B*, 36:5432, 1987.

[17] M. Olivier, J. O. Ström-Olsen, Z. Altounian, R. W. Cochrane, and M. Trudeau. *Phys. Rev. B*, 33:2799, 1986.

[18] A. Sahnoune and J. O. Ström-Olsen. *Phys. Rev. B*, 39:7561, 1989.

[19] P. Lindqvist, O. Rapp, A. Sahnoune, and J. O. Ström-Olsen. *Phys. Rev. B*, 41:3841, 1990.

[20] S. Hikami, A. I. Larkin, and Y. Nagaoka. *Prog. Theor. Phys.*, 63:707, 1980.

[21] B. L. Altshuler, A. G. Aronov, A. I. Larkin, and D. E. Khmel'nitskii. *Sov. Phys. JETP*, 54:411, 1981.

[22] H. Fukuyama and K. Hoshino. *J. Phys. Soc. Jpn.*, 50(7):2131, 1981.

[23] R. Richter, D. V. Baxter, and J. O. Ström-Olsen. *Phys. Rev. B*, 38:10421, 1988.

[24] B. J. Hickey, D. Greig, and M. A. Howson. *J. Phys. F: Met. Phys.*, 16:L13, 1986.

[25] B. L. Altshuler, A. G. Aronov, and Y. Zuzin. *Solid State Commun.*, 34:1616, 1982.

[26] A. J. Millis and P. A. Lee. *Phys. Rev. B*, 30:6170, 1984.

[27] S. J. Poon, K. M. Wong, and A. Drehman. *Phys. Rev. B*, 31:1668, 1985.

[28] M. A. Howson, B. J. Hickey, and C. Shearwood. *J. Phys. F: Met. Phys.*, 16:L175, 1986.

[29] M. A. Howson and B. L. Gallagher. *Phys. Rep.*, 170:265, 1988.

[30] A. Sahnoune. Master's thesis, McGill University, Montreal, 1988.

[31] U. Mizutani and T. Matsuda. *J. Phys. F: Met. Phys.*, 13:2115, 1983.

[32] U. Mizutani, M. Sasaura, Y. Yamada, and T. Matsuda. *J. Phys. F: Met. Phys.*, 17:667, 1987.

[33] J. Erwin, R. Delgado, A. Armbuster, D. G. Naugle, D. P. Love, F. C. Wang, C. L. Tsai, and T. O. Callaway. *Phys. Lett.*, 100A:97, 1984.

[34] D. Shechtman, I. Blech, D. Gratias, and J. W. Cahn. *Phys. Rev. Lett.*, 53:1951, 1984.

[35] U. Mizutani. To appear in Materials Science and Technology, 1992.

[36] U. Mizutani, Y. Sakabe, T. Kishi, K. Kimura, and S. Takeuchi. *J. Phys.: Condens. Matter*, 2:6169, 1990.

[37] P. Bancel. Preprint, 1992.

[38] C. Janot, M. Audier, M. De Boissieu, and J. M. Dubois. *Europhys. Lett.*, 14:355, 1991.

[39] S. J. Poon, A. J. Drehman, and K. R. Lawless. *Phys. Rev. Lett.*, 55:2324, 1985.

[40] K. Kimura, T. Hashimoto, and S. Takeuchi. *J. Phys. Soc. Jpn*, 58:2472, 1989.

[41] S. J. Poon. *Advan. Phys.*, 41:303, 1992.

[42] S. E. Burkov, T. Timusk, and N. W. Ashcroft. Preprint, 1992.

[43] B. D. Biggs, Y. Li, and S. J. Poon. *Phys. Rev. B*, 43:8747, 1991.

[44] T. Klein, A. Gozlan, C. Berger, F. Cyrot-Lackmann, Y. Calvayrac, and A. Quivy. *Europhys. Lett.*, 13:129, 1990.

[45] E. Belin, J. Kojnok, A. Sadoc, A. Traverse, M. Harmelin, C. Berger, and J. M. Dubois. *J. Phys.: Condens. Matter*, 4:1057, 1992.

[46] E. Belin, Z. Dankhazi, A. Sadoc, Y. Calvayrac, T. Klein, and J. M. Dubois. *J. Phys.: Condens. Matter*, 4:4459, 1992.

[47] A. Sadoc, E. Belin, Z. Dankhazi, and A. M. Flank. To appear in J. Non-Cryst. Solids, 1992.

[48] T. Fujiwara. *Phys. Rev. B*, 40:942, 1989.

[49] J. Hafner and M. Krajci. *Phys. Rev. Lett.*, 68:2321, 1992.

[50] D. V. Baxter, R. Richter, and J. O. Ström-Olsen. *Phys. Rev. B*, 35:4819, 1987.

[51] B. D. Biggs, S. J. Poon, and N. R. Munirathnam. *Phys. Rev. Lett.*, 65:2700, 1990.

[52] T. Klein, C. Berger, D. Mayou, and F. Cyrot-Lackmann. *Phys. Rev. Lett.*, 66:2907, 1991.

[53] T. Klein, H. Rakoto, C. Berger, G. Forcaudot, and F. Cyrot-Lackmann. *Phys. Rev. B*, 45:2046, 1992.

[54] H. Fukuyama. In A. L. Efros and M. Pollack, editors, *Electron-electron Interactions in Disordered Conductors*, volume 1, page 155, Amsterdam, 1985. North-Holland.

[55] A. B. Pippard. *Magnetoresistance in Metals*, volume 2 of *Cambridge Studies in Low temperature Physics*. Cambridge University Press, Cambridge, 1989.

[56] J. O. Ström-Olsen. *Proc. Roy. Soc.*, A302:83, 1967.

[57] J. S. Langer and T. Neal. *Phys. Rev. Lett.*, 16(22):984, 1966.

[58] A. Aronov, W. Gey, A. Kitschmann, E. Steep, and P. Warnecke. *Europhys. Lett.*, 19:531, 1992.

[59] G. Bergmann. *Solid State Commun.*, 42:815, 1982.

[60] A. Kawabata. *Solid State Commun.*, 34:431, 1980.

[61] H. Takayama. *Z. Phys.*, 263:329, 1973.

[62] A. Schmid. *Z. Phys.*, 271:251, 1974.

[63] B. L. Altshuler and A. G. Aronov. *Sov. Phys. JETP Lett.*, 30:482, 1979.

[64] J. Rammer. *Rev. Mod. Phys.*, 63:781, 1991.

[65] J. Rammer and A. Schmid. *Phys. Rev. B*, 34:1352, 1986.

[66] N. R. Werthamer, E. Helfand, and P. C. Hohenberg. *Phys. Rev.*, 147:295, 1966.

[67] K. M. Wong, E. J. Cotts, and S. J. Poon. *Phys. Rev. B*, 30:1253, 1984.

[68] L. I. Schiff. *Quantum Mehanics.* McGraw Hill, 3 edition, 1968.

[69] K. Yosida. *Phys. Rev.*, 107:396, 1957.

[70] M. T. Béal-Monod and R. A. Weiner. *Phys. Rev.*, 170:552, 1968.

[71] G. Bergmann. *Phys. Rev. B*, 60:4205, 1987.

[72] N. W. Aschcroft and N. D. Mermin. *Solid State Physics.* Saunders College, Philadelphia, 1976.

[73] P. A. Lee and T. V. Ramakrishnan. *Phys. Rev. B*, 26:4009, 1982.

[74] Y. Isawa and H. Fukuyama. *J. Phys. Soc. Jpn.*, 54:1415, 1984.

[75] J. Hafner and S. S. Jaswal. *Phys. Rev. B*, 38:7320, 1988.

[76] M. Bessière, A. Quivy, S. Lefebvre, J. Devaud-Rsepski, and Y. Calvayrac. *J. Phys. I (France)*, 1:1823, 1991.

[77] American Society of Metals. *Binary Alloy Phase Diagrams*, 1986.

[78] R. St. Amand and B. C. Giessen. *Scrip. Metall.*, 12:1021, 1978.

[79] International Center for Diffraction Data. *JCPDS Powder Diffraction Data*, 1989.

[80] J. W. Cahn, D. Shechtman, and D. Gratias. *J. Mat. Sci.*, 1:13, 1986.

[81] H. S. Chen. *Rep. Prog. Phys.*, 43:353, 1980.

[82] R. Haberkern, P. Lindqvist, and G. Fritsch. To appear in J. Non-Cryst. Solids, 1992.

[83] R. Richter. PhD thesis, McGill University, Montreal, 1988.

[84] R. McFee. *Rev. Scient. Inst.*, 30:98, 1959.

[85] D. B. Betts. *An Introduction to Millikelvin Technology*, volume 1 of *Cambridge Studies in Low temperature Physics*. Cambridge University Press, 1989.

[86] C. Tsai and F. C. Lu. *J. Non-Cryst. Solids*, 61 and 62:1403, 1984.

[87] M. A. Howson, A. Paja, G. J. Morgan, and M. J. Walker. *Z. Phys. Chem. NF*, page 683, 1987.

[88] D. V. Baxter, R. Richter, M. L. Trudeau, R. W. Cochrane, and J. O. Ström-Olsen. *J. Phys. France*, 50:1673, 1989.

[89] J. Bieri, A. Fert, G. Creuzet, and J. C. Ousset. *Solid State Commun.*, 49:849, 1984.

[90] Y. Isawa. *J. Phys. Soc. Jpn.*, 53:37, 1984.

[91] W. Gey and S. Weyhe. *Europhys. Lett.*, 18:331, 1992.

[92] F. M. Mayeya and M. A. Howson. submitted to J. Phys: Cond. Matt., 1992.

[93] P. Lindqvist and G. Fritsch. *Phys. Rev. B*, 40:5792, 1989.

[94] M. L. Trudeau and R. W. Cochrane. *Phys. Rev. B*, 38:5353, 1988.

[95] A. Schulte. *Solid State Commun.*, 60:99, 1986.

[96] M. Olivier, J. O. Ström-Olsen, and Z. Altounian. *Phys. Rev. B*, 35:333, 1987.

[97] G. Bergmann, W. Wei, Y. Zou, and R. M. Mueller. *Phys. Rev. B*, 41:7386, 1990.

[98] J. Liu, T. L. Meisenheimer, and N. Giordano. *Phys. Rev. B*, 40:7527, 1989.

[99] N. Kumar, D. V. Baxter, R. Richter, and J. O. Ström-Olsen. *Phys. Rev. Lett.*, 59:1853, 1987.

[100] Y. Imry and A. Stern. Working party on elctron-transport in small systems, International Centre for Theoretical Physics, 1988.

[101] A. Stern, Y. Aharonov, and Y. Imry. *Phys. Rev. A*, 41:3446, 1990.

[102] A. Stern, Y. Aharonov, and Y. Imry. In B. Kramer, editor, *Quantum Coherence in Mesoscopic Systems*, volume 254, New York, 1991. NATO ASI Series: Series B, Plenum Press.

[103] J. Rammer, A. L. Shelankov, and A. Schmid. *Phys. Rev. Lett.*, 60:1985, 1988.

[104] G. Bergmann. *Phys. Rev. Lett.*, 60:1986, 1988.

[105] N. Kumar, D. V. Baxter, R. Richter, and J. O. Ström-Olsen. *Phys. Rev. Lett.*, 60:1987, 1988.

[106] A. J. Millis and P. A. Lee. *Phys. Rev. B*, 31:5523, 1985.

[107] A. Sahnoune, J. O. Ström-Olsen, and H. E. Fischer. to appear in Phys. Rev. B, 15 October, 1992.

[108] T. Chui, P. Lindfeld, W. L. McLean, and K. Mui. *Phys. Rev. Lett.*, 47:1617, 1981.

[109] N. F. Mott and E. A. Davis. *Electronic Processes in Non-Crystalline Materials.* The International Series of Monographs on Physics. Clarendon Press, Oxford, 1979.

[110] T. M. Rice and W. F. Brinkman. In R. E. Mills, E. Asher, and R. I. Jaffe, editors, *Critical Phenomena in Alloys, Magnets, and Superconductors*, page 593, New York, 1971. McGraw-Hill.

[111] G. A. Thomas, A. Kawabata, Y. Ootuka, S. Katsumoto, and W. Sasaki. *Phys. Rev. B*, 26:2113, 1982.

[112] T. F. Rosenbaum, K. Andres, G. A. Thomas, and P. A. Lee. *Phys. Rev. Lett.*, 46:568, 1981.

[113] H. v. Lohneysen and M. Welsch. *Phys. Rev. B*, 44:9045, 1991.

[114] J. C. Ousset, S. Askenazy, H. Rakoto, and J. M. Broto. *J. Phys. France*, 46:22145, 1985.

[115] D. W. Marquardt. *J. Soc. Ind. Appl. Math.*, 11(2):431, 1963.

[116] T. Fujiwara. 8th International conference on liquid and amorphous metals (Wein,Austria), 1992.